Dipl.-Ing. Susanne Maria Bauer, BSc

Models and simulation of EMC problems

DOCTORAL DISSERTATION

for obtaining the academic degree of doctor of technical sciences

submitted to the

Graz University of Technology

Supervisor/First reviewer

Univ.-Prof. Dipl.Ing Dr.techn. Oszkár Bíró

Institute of Fundamentals and Theory in Electrical Engineering

Second reviewer

Univ.-Prof. Dipl.-Ing. Dr.-techn. József Pávó

Budapest University of Technology and Economics

Graz, January 2021

EIDESSTATTLICHE ERKLÄRUNG

Ich erkläre an Eides statt, dass ich die vorliegende Arbeit selbstständig verfasst, andere als die angegebenen Quellen/Hilfsmittel nicht benutzt und die den benutzten Quellen wörtlich und inhaltlich entnommene Stellen als solche kenntlich gemacht habe.

Graz, am ………………………… …………………………………………..

(Unterschrift)

STATUTORY DECLARATION

I declare that I have authored this thesis independently, that I have not used other than the declared sources / resources, and that I have explicitly marked all material which has been quoted either literally or by content from the used sources.

…………………………… …………………………………………..

date (signature)

Abstract

This work deals with different model development approaches in the topic of electro-magnetic compatibility (EMC) and the simulation therein, using numerical techniques like the Finite Element Method (FEM) and the transmission-line modelling for multi-conductor transmission-lines that can be applied in circuit simulators.

One major focus of this work is the transfer impedance of shielded cables with braided shields. With the aid of the FEM, the geometry- and material parameters can be modelled very precisely and also the influence of parameter variations on the transfer impedance can be analysed with this simulation approach. Based on the numerical solution, a simple circuit-simulator model and a new measurement technique are developed. Also existing analytical approaches for the transfer impedance have been studied in more detail with the aid of the numerical results. Usually, the analytical models are compared to measured results but this limits the possible range of geometry- and material parameter variations that are of interest for example in case of stretched or pinched cables. It is shown that, using numerical simulations, these restrictions can be eliminated.

Another very important topic in the field of EMC are fast transients and conducted emission and, therefore, the standardized measurement setup for conducted emission for cable harnesses called the Capacitive Coupling Clamp has been modelled with FEM. The multi-transmission-line parameters for the circuit-simulator model are extracted with the usage of this framework as well and the results are compared to measured data of the same setup. The simulated and measured results stand in excellent agreement.

Also relevant in the context of electrical fast transient disturbances, overvoltage protection devices such as transient voltage suppressor diodes and especially their modelled behaviour in spice-like simulators are investigated as well. This investigation of existing models shows that knowledge of the implemented models is crucial for correct usage and, as a consequence, for reliable simulation results.

Kurzfassung

Diese Arbeit befasst sich mit diversen Anwendungen im Bereich der elektromagnetischen Verträglichkeit (EMV) und deren Simulation mit Hilfe numerischer Methoden wie der Finite-Elemente-Methode (FEM) und mit Simulationsansätzen wie der Leitungstheorie-Modellierung für Mehrleitersysteme, welche in Netzwerksimulatoren angewendet werden können.

Ein wichtiger Punkt ist die Untersuchung der Transferimpedanz von Geflechtschirmen von geschirmten Kabeln. Die notwendigen Geometrie- und Materialparameter können mit Einsatz der FEM sehr präzise modelliert und simuliert werden. Basierend auf den numerischen Simulationen wurde ein Netzwerkmodell für Netzwerksimulatoren und eine neue Messmethode der Transferimpedanz entwickelt. Die existierenden analytischen Modelle konnten mit den Ergebnissen der numerischen Simulation ebenfalls für Parametervariationen untersucht werden. Üblicherweise werden die Modelle mit Messungen von Standard-Koaxialkabeln verifiziert, was in diesem Fall aber die Parametervariationen wie Geometrieabweichungen für z.B. den Fall von gestreckten oder gequetschten Kabeln und auch Materialänderungen nicht so einfach darstellen kann.

Ein weiteres wichtiges Thema in der EMV sind leitungsgebundene Störungen und schnelle transiente Störsignale. In diesem Kontext wird der standardisierte Messaufbau der sogenannten Kapazitiven Koppelzange implementiert, welche zur Untersuchung von leitungsgebundenen Störungen verwendet wird. Für dieses Mehrleitersystem wurden die Leitungsparameter mit Hilfe der FEM für ein Netzwerksimulator-Modell extrahiert und die simulierten Ergebnisse mit Messungen verifiziert und die Ergebnisse stimmen ausgezeichnet überein.

Zusätzlich werden Überspannungsschutzelemente gegen diese schnellen transienten Störungen, wie die Transient-Voltage-Suppressor-Diode und im speziellen deren Modellierung in LTspice, untersucht. Hier werden die Unterschiede der verschiedenen Modelle in Bezug auf deren Anwendungsbereiche für korrekte Simulationsergebnisse diskutiert.

Acknowledgments

First of all, I would like to thank my former head of the institute and PhD supervisor Univ.-Prof. Dipl.-Ing. Dr.techn. Oszkár Bíró for his cooperation and support.

It is an honour for me to be allowed to dissertate at this institute where, among others, renowned scientific paragons such as Oszkár Bíró, Kurt Preis and Werner Renhart are active, all of whom I was also allowed to count among my colleagues.

I also want thank my colleagues, DI. Dr.techn. Christian Türk, ObstltdhmtD and Ass. Prof. Dipl.-Ing. Dr.techn. Gunter Winkler (Institute of Electronics), for the excellent and pleasant collaboration.

I would also like to thank all my colleagues and especially Univ.-Prof. Dipl.-Ing. Dr.techn. Manfred Kaltenbacher.

A big thank you goes of course to my parents, who have always supported me with infinite patience.

And last but not least, I want to say thank you:

to my neighbours Kathi and Tom. Without them I probably would have had almost only conversations with my cats during the COVID lockdown,

to Peter Miesbauer, for years of friendship that has withstood all stressful moments,

to Klaus Roppert, for stimulating discussions of technical and general nature

to Astrid, Manuela, Alexandra, Edith and Robert, for uplifting coffee breaks

and to all those who have accompanied me in one way or another over the past years.

"yesterday's weirdness is tomorrow's reason why"

Hunter S. Thompson

Danksagung

Ich möchte mich zuerst bei meinem ehemaligen Institutsleiter und PhD Betreuer Univ.-Prof. Dipl.-Ing. Dr.techn. Oszkár Bíró für seine Zusammenarbeit und Unterstützung bedanken.

Es ist mir eine Ehre an diesem Institut dissertieren zu dürfen an dem unter anderen namhafte wissenschaftliche Vorbilder wie Oszkár Bíró, Kurt Preis und Werner Renhart tätig sind, welche ich auch zu meinen Kollegen zählen durfte.

Weiters möchte ich mich bei meinen Kollegen, Dipl.-Ing. Dr.techn. Christian Türk, Obstltdhmtd und Ass. Prof. Dipl.-Ing. Dr.techn. Gunter Winkler (Institut für Elektronik), für die ausgezeichnete und angenehme Zusammenarbeit, bedanken.

Ebenso gilt ein Dankeswort all meinen Kollegen und insbesondere an Herrn Univ.-Prof. Dipl.-Ing. Dr.techn. Manfred Kaltenbacher.

Ein großes Dankeschön geht natürlich an meine Eltern, die mich immer mit unendlicher Geduld unterstützt haben.

Und zu guter Letzt möchte ich mich bedanken:

Bei meinen Nachbarn Kathi und Tom, ohne die ich während des COVID Lockdowns wahrscheinlich nur mehr Gespräche mit meinen Katzen geführt hätte,

bei Peter Miesbauer, für eine jahrelange Freundschaft die jeglichem Stress standgehalten hat,

bei Klaus Roppert, für anregende Gespräche fachlicher und allgemeiner Natur

bei Astrid, Manuela, Alexandra, Edith und Robert, für aufmunternde Kaffeepausen

und all jenen, die mich in den letzten Jahren auf die eine oder andere Weise begleitet haben.

"yesterday's weirdness is tomorrow's reason why"

Hunter S. Thompson

Table of Contents

1 Introduction

1.1 Motivation

In terms of electromagnetic compatibility (EMC), an electronic device has to meet given criteria regarding susceptibility, immunity and compatibility. This means that any electronic device, when recipient of disturbances, has to work properly up to a certain level of unwanted emission from other devices and every electronic device, when considered to be the source of disturbances, has to stay within defined limits of emission, in a way that the whole system is able to function reliably in its defined environment.

Supporting the design cycle of any electronic device with simulations targeting the electromagnetic behaviour constitutes a powerful tool to investigate possible problems. Applying suitable simulations at every stage during the development phase of an electronic device can spare a lot of time and costly redesigns when used in a correct and thoughtful manner and, for first appraisals, some time consuming measurements can even be replaced at times. For developing simulation models however, the verification of the same by measurements is an important step, since, especially in the field of EMC, not all relevant factors can be modelled and by the additional use of measurements, hence less relevant parameters can be eliminated from the models. This is not only important for electronic devices by themselves but also for whole setups consisting of cables, protection devices and other systemically relevant parts in the entire equipment used.

Problem settings in the topic of EMC can coarsely be divided into conducted emission and radiated emission and, therefore, the scope of applications regarding measurements and simulations is extensive.

The problem settings covered in this work focus mainly on conducted emission on system-level and simulation approaches of these problems. The aim is to find manageable circuit models that can easily be used in standard circuit simulators as for example LTspice [1] which was used throughout this work. To gather these models, the main procedures here are the Finite Element Method (FEM) for parameter extraction of given setups and problem settings with more complex geometries and transmission-line models for simpler geometries where the parameters can be calculated analytically. EMC is not only an important issue on system-level applications, but also in the field of integrated circuits and their testing techniques [3]-[5].

1.2   Aim and focus of this work

A large part of the material treated in this work concerns the behaviour of braided cable shields and their transfer impedance with respect to geometry- and material variations as well as frequency dependency and to develop a manageable model for circuit simulators of such cable shields. The transfer impedance is an important parameter to characterize the behaviour of a shielded cable and it describes the shielding effectiveness in terms of electromagnetic immunity and emission. The transfer impedance is a length-related parameter and it is measured in Ohms per meter. Usually, graphical data regarding the shielding effectiveness is provided by cable manufacturers but insufficient details regarding the transfer impedance are given even though it is known to be an important cable parameter. In literature mainly analytical approaches for this problem setting can be found, e.g. in [18] and [26]-[30], and these models are mainly verified by measurements limiting their validation for excessive parameter variations concerning geometry and material.

To develop an adaptable circuit model, a parametrized FEM-model was implemented, described in my publications [7] and [10]. This is also used to investigate existing analytical models for a wide variety of geometry- and material variations.

The advantage of the FEM-model is that the influence of excessive parameter variations with respect to the typical shield geometry and also the influence of different materials on the transfer impedance can be evaluated easier without fabricating different cables and extensive measurements of the very same which would be time- and cost- intensive.

The FEM model has been verified with measurements as well, although the setup of such measurement techniques for the transfer impedance are very costly and time consuming. To avoid these complicated setups, based on the simulation approach, an alternative measurement technique for the transfer impedance was additionally developed in my publications [8] and [9], which is not standardized but can be used for cable shield characterization with relatively low effort and excellent accuracy.

Another integral part of EMC related problems are so-called conducted emissions and their testing techniques especially together with electrostatic discharge, ESD, [38] and electrical fast transients, EFT/BURST, [39]. These fast voltage or current peaks with typical rise-times in the range of nanoseconds can be transmitted to sensible circuit inputs via connected signal lines and can cause severe damage. Therefore, it is important to understand the propagated fast transients and, later on, also how to protect circuit inputs or sensible electronic parts against these disturbances.

Given analytical approaches to simulate the standardized EFT/BURST test-setup exist [46], [47] but some parameter calculations are not described in a sufficiently detailed way, which prevents their common understanding. Therefore, the standardized measurement setup for conducted emission, the so called capacitive coupling clamp [39], is simulated with the aid of the FEM-method and, by parameter extraction, a circuit model for testing simplified cable harnesses, was developed [6].

Together with electrical fast transients, the question of signal propagation is important, especially when developing protection structures to ensure the functionality of a given system or device and, therefore, existing Spice-models of overvoltage protection devices such as transient voltage suppressor diodes (TVS-diodes) that are used as protection against electrical fast transients [2] have been investigated as well. This investigation additionally shows how important it is to have knowledge on the way how simulation-models work and under which circumstances they can be used correctly and when one has to adapt them.

1.3   Structure of this work

This work is structured into ten chapters. This current chapter has provided a short introduction of the scope of this work.

Chapter 2 gives an overview of the mathematical fundamentals that are needed for the numerical analysis with the finite element method and a short summary of the concept of the lumped element approach that is commonly used to simulate transmission-lines in circuit simulators. The finite element method in this work is used mainly for developing applicable circuit simulator models especially of problem settings and measurement setups that are geometrically more complex.

In chapters 3 to 7, the focus is on the transfer impedance of shielded cables. Chapter 3 introduces the concept of the transfer impedance and this parameter is investigated by the use of existing analytical methods. Chapter 4 describes how the parametrized FEM-model has been implement with the in-house software Electromagnetic Field Analysis Tool 3D (EleFAnT3D).

In chapter 5, a new and simple method to measure the transfer impedance of shielded cables with the use of a 2-port network analyser without a complex and costly measurement setup is introduced and the measured data is used to verify the results for the FEM- and the analytical models. The models thus developed are used in chapter 6 to analyse parameter influences and their significance on the transfer impedance by applying Global Sensitivity Analysis.

After investigating geometry- and parameter variations and the development of the measurement technique, chapter 7 provides a circuit-simulator model to simulate the transfer impedance including a very simple model to handle the skin effect losses occurring with increasing frequencies.

The problem of electrical fast transients is described in chapter 8 and chapter 9, especially the investigation of protection devices against these unwanted disturbances and a standardized measurement setup for testing conducted emission in cable harnesses.

In chapter 8, model limitations of transient voltage suppressor diodes used in circuit simulators such as LTspice are investigated and, depending on the problem setting, a solution for correct applications is provided. Chapter 9 deals with the standardized measurement setup called the capacitive coupling clamp used for investigating conducted emission on cable harnesses. The final chapter 10 gives a brief outlook for possible future work mainly focusing on transfer impedance investigations.

1.4 Collaborations with third parties

Most parts in this work are a direct result of the project collaboration with the Ministry of Defence of Austria, together with Dipl.-Ing. Dr.techn. Christian TÜRK, Obstlt-dhmtD.

The main focus of this project was the investigation of the transfer impedance of braided cable shields and the influence of parameter variations including simulations and measurements.

Examination of typical spice models of transient voltage suppressor diodes (TVS-diodes) and their correct usage is included in this project as well and my contributions [2], and [7]-[10] are directly linked to this project-collaboration.

Essential measurement support and provision of measurement equipment for my contributions [2]-[10] was provided by Ass. Prof. Dipl.-Ing. Dr.techn. Gunter Winkler, from the Institute of Electronics (IFE) of the Graz University of Technology.

2 Fundamentals

This chapter provides the mathematical fundamentals that are used in this work to simulate EMC related tasks. Especially the finite element method represents an important tool to investigate the geometry dependencies of the transfer impedance of braided cable shields which will be discussed in later chapters, that otherwise could only be done by the use of measurements. The finite element method is not only used to investigate the transfer impedance as in chapter 4, but it is also applied to extract circuit parameters of a standardized test-setup to measure conducted emission, the so called capacitive coupling clamp, in chapter 9.

A short introduction of the transmission-line theory is given, too. This is a manageable technique to simulate wire-like structures in circuit simulators which will be used for conducted emission investigations in later parts of this work as well. In chapter 8 it is used to simulate wires in LTspice to analyse the behaviour of TVS-diode models with respect to electrical fast transients and the transmission-line approach is also applied in chapter 9, covering the above mentioned capacitive coupling clamp to simulate the whole measurement setup in LTspice as well.

2.1 Maxwell's equations

Maxwell's equations are a set of partial differential equations that describe the behaviour of electric and magnetic fields and their relations to each other.

The first Maxwell equation, Ampere's law, states that an electric current and a time varying electric field can generate magnetic fields. In the time domain it is written as

$$\nabla \times \mathbf{H} = \mathbf{J} + \frac{\partial \mathbf{D}}{\partial t} \tag{2.1}$$

where $\mathbf{H}$ is the magnetic field density, $\mathbf{J}$ is the current density and $\mathbf{D}$ is the electric flux density.

Faraday's law of induction, the second of Maxwell's equations, states that a time varying magnetic field induces an electric field and it is given as

$$\nabla \times \mathbf{E} = -\frac{\partial \mathbf{B}}{\partial t} \tag{2.2}$$

where $\mathbf{E}$ is the electric field density and $\mathbf{B}$ is the magnetic flux density.

Gauss's law for magnetism states that there are no magnetic monopoles, i.e. no magnetic charges exist and it is written as

$$\nabla \cdot \mathbf{B} = 0. \tag{2.3}$$

Gauss's law states that a positive electric charge acts like a source for electric fields and a negative charge acts as a sink for electric fields and is written as

$$\nabla \cdot \mathbf{D} = \rho \tag{2.4}$$

where ρ is the volume charge density.

The constitutive relations are given as:

$$\mathbf{B} = \mu \mathbf{H}, \tag{2.5}$$

$$\mathbf{J} = \sigma \mathbf{E}, \tag{2.6}$$

$$\mathbf{D} = \varepsilon \mathbf{E} \tag{2.7}$$

where $\mu = \mu_0 \cdot \mu_r$ denotes the permeability with μ_0 defining the vacuum permeability and μ_r the relative permeability, σ is the conductivity and $\varepsilon = \varepsilon_0 \cdot \varepsilon_r$ is the permittivity, again ε_0 defining the vacuum permittivity and ε_r the relative permittivity.

Ampere's law (2.1) and Faraday's law of induction (2.2) in the frequency domain are described as:

$$\nabla \times \mathbf{H} = \mathbf{J} + j\omega \mathbf{D} \tag{2.8}$$

$$\nabla \times \mathbf{E} = -j\omega \mathbf{B} \tag{2.9}$$

by substituting the time derivate $\dfrac{\partial}{\partial t}$ with $j\omega$ where ω is the angular frequency.

2.2 Quasi-static fields

In case of the quasi static eddy current problems, the relationship

$$\left| \frac{\partial \mathbf{D}}{\partial t} \right| << |\mathbf{J}| \tag{2.10}$$

applies and the subset of applicable Maxwell equations for this quasi-static field problem in the time harmonic case can be summarized as follows:

$$\nabla \times \mathbf{H} = \mathbf{J} \tag{2.11}$$

$$\nabla \cdot \mathbf{B} = 0 \tag{2.12}$$

$$\nabla \times \mathbf{E} = -j\omega \mathbf{B} \tag{2.13}$$

and the constitutive relations are

$$\mathbf{B} = \mu \mathbf{H} \ \text{ and } \ \mathbf{J} = \sigma \mathbf{E} \tag{2.14}$$

2.2.1 Skin effect problem

Fig. 2.1 shows the field model of a skin effect problem with current excitation.
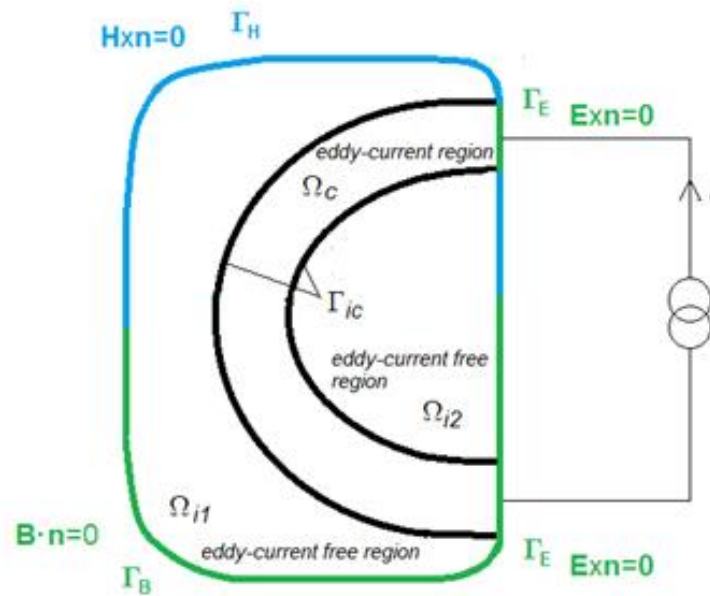
Fig. 2.1: Field model of a skin-effect problem

Maxwell's equations for the eddy current region constituting the conducting region Ω_c are:

$$\left. \begin{aligned} \nabla \times \mathbf{H} &= \mathbf{J} \\ \nabla \times \mathbf{E} &= -j\omega \mathbf{B} \\ \nabla \cdot \mathbf{B} &= 0 \end{aligned} \right\} \ \text{ in } \ \Omega_c \tag{2.15}$$

and in the eddy-current free region Ω_i including non-conducting domains and conductors with given current density, the set of equations are

$$\left.\begin{array}{l} \nabla \times \mathbf{H} = \mathbf{J} \\ \nabla \cdot \mathbf{B} = 0 \end{array}\right\} \quad \text{in} \quad \Omega_i \qquad (2.16)$$

with the constitutive relations

$$\mathbf{B} = \mu\mathbf{H} \quad \text{in} \quad \Omega_c \quad \text{and} \quad \Omega_i \qquad (2.17)$$

and

$$\mathbf{J} = \sigma\mathbf{E} \quad \text{in} \quad \Omega_c. \qquad (2.18)$$

The boundary conditions are:

$$\mathbf{H} \times \mathbf{n} = \mathbf{0} \quad \text{on} \quad \Gamma_{Hc} \qquad (2.19)$$

$$\mathbf{E} \times \mathbf{n} = \mathbf{0} \quad \text{on} \quad \Gamma_E \qquad (2.20)$$

$$\mathbf{H} \times \mathbf{n} = \mathbf{K} \quad \text{on} \quad \Gamma_{Hi} \qquad (2.21)$$

$$\mathbf{B} \cdot \mathbf{n} = -b \quad \text{on} \quad \Gamma_B. \qquad (2.22)$$

On the interface Γ_{ci} between the conducting region Ω_c and the non-conducting domain Ω_i, the normal component of the flux density and the tangential component of the magnetic field intensity are continuous providing coupling between the two formulations:

$$\mathbf{H} \times \mathbf{n} = \mathbf{0} \quad \text{and} \quad \mathbf{B} \cdot \mathbf{n} = 0 \text{ continuous on} \quad \Gamma_{ic} \qquad (2.23)$$

where $\mathbf{n}$ in (2.19) – (2.23) denotes the outer normal vector.

2.2.2 A,V-A-formulation

For the numerical analysis, the **A**,V-**A**-formulation is used as proposed in [11] and [12]. A magnetic vector potential **A** and an electric scalar potential V replaced by a modified scalar potential v with

$$V = j\omega v \qquad (2.24)$$

are introduced.

The magnetic vector potential **A** is used in the non-conducting region Ω_i and in the conducting region Ω_c.

The modified scalar potential v is used in the conducting region Ω_c :

$$\mathbf{B} = \nabla \times \mathbf{A} \text{ in } \Omega_c \text{ and } \Omega_i \tag{2.25}$$

$$\mathbf{E} = -j\omega\mathbf{A} - \nabla V = -j\omega\mathbf{A} - j\omega\nabla v \text{ in } \Omega_c \tag{2.26}$$

satisfying Faraday's law of induction (2.12) and Gauss' law for magnetism (2.13).

Ampere's law (2.11) using the constitutive relations (2.14) results in

$$\nabla \times (\frac{1}{\mu}\nabla \times \mathbf{A}) + \sigma j\omega\mathbf{A} + \sigma j\omega\nabla v = \mathbf{0} \quad \text{in} \quad \Omega_c \tag{2.27}$$

$$\nabla \times (\frac{1}{\mu}\nabla \times \mathbf{A}) = \mathbf{J}_0 \quad \text{in} \quad \Omega_i \tag{2.28}$$

In the eddy current region, Ampere's law results in one vectorial differential equation for both potentials $\mathbf{A}$ and v. An additional scalar differential equation, the law of continuity

$$\nabla \cdot \mathbf{J} = 0 \tag{2.29}$$

is added which results in

$$\nabla \cdot \left(-\sigma j\omega\mathbf{A} - \sigma j\omega\nabla v\right) = 0 \quad \text{in} \quad \Omega_c \tag{2.30}$$

and this leads to a vectorial- and a scalar differential equation for the vector-potential and the scalar potential.

The boundary conditions (2.19) – (2.22) then result in

$$\frac{1}{\mu}\nabla \times \mathbf{A} \times \mathbf{n} = \mathbf{0} \quad \text{and} \quad \mathbf{n} \cdot (-\sigma j\omega\mathbf{A} - \sigma j\omega\nabla v) = 0 \quad \text{on} \quad \Gamma_{Hc} \tag{2.31}$$

$$\mathbf{n} \times \mathbf{A} = \mathbf{0} \quad \text{and} \quad v = \text{konst} = v_0 \quad \text{on} \quad \Gamma_E \tag{2.32}$$

$$\frac{1}{\mu} \times \mathbf{A} \times \mathbf{n} = \mathbf{K} \quad \text{on} \quad \Gamma_{Hi} \tag{2.33}$$

$$\mathbf{n} \cdot \nabla \times \mathbf{A} = -b \quad \text{on} \quad \Gamma_B \tag{2.34}$$

and the interface conditions (2.23) are

$$\nabla \times \mathbf{A}_c \times \mathbf{n}_c + \nabla \times \mathbf{A}_i \times \mathbf{n}_i = \mathbf{0} \quad \text{and}$$
$$\frac{1}{\mu_c}\nabla \times \mathbf{A}_c \cdot \mathbf{n}_c + \frac{1}{\mu_i}\nabla \times \mathbf{A}_i \cdot \mathbf{n}_i = 0 \quad \text{on} \quad \Gamma_{ic}. \tag{2.35}$$

The subscripts i and c stand for the quantities in the non-conducting and the conducting regions, respectively, and for the outer normal vectors the relation $\mathbf{n}_c = -\mathbf{n}_i$ is valid.

For skin effect problems, the impressed current density function $\mathbf{J}_0$, the surface current density $\mathbf{K}$ and the magnetic charge density b equal zero.

The boundary conditions for a skin effect problem with current excitation are given as

$$v_0 = 0 \quad \text{on} \quad \Gamma_{E1} \quad \text{and} \quad v_0 = v_x \quad \text{on} \quad \Gamma_{E2} \tag{2.36}$$

where Γ_{E1} and Γ_{E2} in this case denote the surfaces of the electrodes of the inner conductor and respectively of the shield and v_x denotes the voltage between these two electrodes and is an unknown constant.

Additionally, with the current I_0 given, the following relationship has to be satisfied too:

$$\int_{\Gamma_{E2}} \sigma \left(j\omega \mathbf{A} + j\omega \nabla v \right) \cdot \mathbf{n} d\Gamma = I_0 \tag{2.37}$$

2.2.3 Finite element solution

For the finite element method [13], [14] the complex problem domain is discretized in a finite number of smaller sub-regions of simpler geometry. The resulting finite element mesh consists of a certain number of edges and nodes.

The vector potential is approximated by the edge-shape functions $\mathbf{N}_j$ ($j = 1, 2 ... n_1$) of the edges that are not located on Γ_E or on Γ_B

$$\mathbf{A} \approx \mathbf{A}_n = \mathbf{A}_D + \sum_{j=1}^{n_1} A_j \mathbf{N}_j \tag{2.38}$$

and the scalar potential is approximated by the nodal-shape functions N_j ($j = 1, 2 ... n_2$) of nodes that are not located on Γ_E

$$v \approx v_n = v_D + \sum_{j=1}^{n_2} v_j N_j \tag{2.39}$$

and therefore the functions $\mathbf{N_j}$ and N_j satisfy the homogeneous Dirichlet boundary conditions on Γ_E and Γ_B.

The functions $\mathbf{A}_D$ and v_D

$$\mathbf{A}_D = \sum_{edges_j \in \Gamma_E, \Gamma_B} A_j \mathbf{N}_j$$

$$v_D = \sum_{nodes_j \in \Gamma_E} v_j N_j$$

(2.40)

fulfill the inhomogeneous Dirichlet boundary conditions.

The finite element Galerkin equation system then is given as

$$\int_{\Omega_c + \Omega_i} \nabla \times \mathbf{N}_i \cdot \frac{1}{\mu} \nabla \times \mathbf{A}_n d\Omega +$$

$$\int_{\Omega_c} \mathbf{N}_i \cdot \sigma j\omega(\mathbf{A}_n + \nabla v_n) d\Omega = 0 \quad \text{for} \quad i = 1, 2, \dots n_1,$$

(2.41)

$$\int_{\Omega_c} \nabla N_i \cdot \sigma j\omega(\mathbf{A}_n + \nabla v_n) d\Omega = 0 \quad \text{for} \quad i = 1, 2, \dots n_2 \ . \tag{2.42}$$

In case of the skin effect problem with current excitation at hand, the value v_x of the scalar potential on the electrode surface Γ_{E2} is not known. Therefore, v_D is not totally specified:

$$v_D = \sum_{node_j \in \Gamma_E} v_j N_j = v_x \sum_{node_j \in \Gamma_{E2}} N_j. \tag{2.43}$$

the following notation is introduced:

$$N_{\Gamma_{E2}} = \sum_{nodes_j \in \Gamma_{E2}} N_j \quad . \tag{2.44}$$

The value of this scalar function is 1 on Γ_{E2} and 0 on Γ_{E1} and this leads to $n_2 + 1$ unknowns for of v_n:

$$v \approx v_n = v_x N_{\Gamma_{E2}} + \sum_{j=1}^{n_2} v_j N_j \quad . \tag{2.45}$$

Since $N_{\Gamma_{E2}}$ is a weighting function as well this leads to an additional equation:

$$\int_{\Omega_c} \nabla N_{\Gamma_{E2}} \cdot \sigma j\omega(\mathbf{A}_n + \nabla v_n) d\Omega = I_0 \ . \tag{2.46}$$

2.3 Quasi-static electric field

Additionally, quasi-static electric field computations [15] have been carried out later on to calculate the distributed capacitances of a given measurement setup in order to obtain a circuit model for simulation in LTspice.

Faraday's law in the time harmonic case describing the quasi-static electric field is

$$\nabla \times \mathbf{E} = \mathbf{0} \ . \tag{2.47}$$

The law of continuity has to be fulfilled too:

$$\nabla \cdot (\mathbf{J} + j\omega \mathbf{D}) = 0 \ . \tag{2.48}$$

The boundary conditions are

$$\mathbf{E} \times \mathbf{n} = 0 \quad \text{on} \quad \Gamma_E \tag{2.49}$$

and

$$\mathbf{J} \cdot \mathbf{n} = 0 \quad \text{on} \quad \Gamma_J \tag{2.50}$$

2.3.1 V-formulation of the quasi- static electric field

The electric field intensity $\mathbf{E}$ can be described with the scalar potential V as

$$\mathbf{E} = -\nabla V \tag{2.51}$$

satisfying (2.47).

Together with the material relations

$$\mathbf{J} = \sigma \mathbf{E} \quad \text{and} \quad \mathbf{D} = \varepsilon \mathbf{E} \ , \tag{2.52}$$

this leads to the scalar differential equation

$$\nabla \cdot (-\sigma \nabla V - j\omega \varepsilon \nabla V) = 0. \tag{2.53}$$

For the scalar potential, the boundary conditions (2.49) and (2.50) are

$$V = V_0 \quad \text{on} \quad \Gamma_E \tag{2.54}$$

and

$$(-\sigma \nabla V - j\omega \varepsilon \nabla V) \cdot \mathbf{n} = 0 \quad \text{on} \quad \Gamma_J. \tag{2.55}$$

2.3.2 Finite element solution

For the approximation of the scalar potential, nodal-shape functions N_j ($j = 1, 2...n$) are used, which are again the functions belonging to the nodes that are not located on Γ_E, as already mentioned in section 2.2.3. This again leads to

$$V \approx V_n = V_D + \sum_{j=1}^{n} V_j N_j \tag{2.56}$$

where

$$V_D = \sum_{nodes_j \in \Gamma_E} V_j N_j. \tag{2.57}$$

The Galerkin equation system then can be written as

$$\int_{\Omega} \nabla N_i \cdot \sigma \nabla V_n d\Omega + \int_{\Omega} \nabla N_i \cdot j\omega\varepsilon \nabla V_n d\Omega = 0 \quad (i = 1, 2, ..., n) \tag{2.58}$$

2.4 Transmission-line model

The transmission-line model [16] and [17] is a representation of two- or multi-conductor transmission-lines by a per-unit-length equivalent circuit as it is depicted in Fig. 2.4 and Fig. 2.5.

The advantage of these equivalent circuits is, that they can be easily used in any circuit simulator as for example LTspice especially for simulating wire type structures. This method is especially used in chapter 8 and chapter 9 to simulate a simple test setup respectively a more complex measurement setup for conducted emission.

2.4.1 Transmission-line equations

This formulation is valid if the dimensions of the setup, especially the dimension of the cross-section of the setup are electrically short and the transverse electromagnetic mode (TEM-mode) is the mode of operation. If the dimensions are not electrically short additional higher order transverse electric (TE) and transverse magnetic (TM) field structures and modes of propagation will occur.

The derivation of the transmission-line equations is demonstrated briefly on the basis of a two-conductor system as depicted in Fig 2.2.
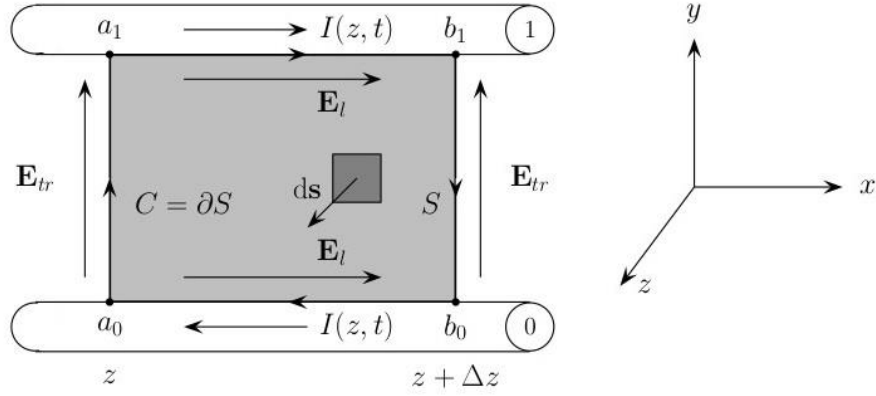
Fig. 2.2: Two-conductor system for first transmission-line equation

The first transmission-line equation can be derived from Faraday's law:

$$\oint_{C=\partial S} \mathbf{E} \cdot d\mathbf{l} = -\mu \frac{d}{dt} \int_S \mathbf{H}_{tr} \cdot d\mathbf{S} \tag{2.59}$$

where S is a surface between the two conductors in the longitudinal (z) direction and the contour C is its boundary, as it is depicted in Fig 2.2. Along the given contour C (2.59) can be re-written as:

$$\int_{a_0}^{a_1} \mathbf{E}_{tr} \cdot d\mathbf{l} + \int_{a_1}^{b_1} \mathbf{E}_\ell \cdot d\mathbf{l} + \int_{b_1}^{b_0} \mathbf{E}_{tr} \cdot d\mathbf{l} + \int_{b_0}^{a_0} \mathbf{E}_\ell \cdot d\mathbf{l} = -\mu \frac{d}{dt} \int_S \mathbf{H}_{tr} \cdot d\mathbf{S} \tag{2.60}$$

where $\mathbf{E}_{tr}$ denotes the electric field intensity in the transversal ($x-y$) plane and $\mathbf{E}_\ell$ is the electric field intensity along the longitudinal direction. Since the setup is considered to be electrically short, a voltage between the two conductors can be defined uniquely:

$$-\int_{a_0}^{a_1} \mathbf{E}_{tr}(x, y, z, t) \cdot d\mathbf{l} = U(z,t)$$

$$-\int_{b_0}^{b_1} \mathbf{E}_{tr}(x, y, z + \Delta z, t) \cdot d\mathbf{l} = U(z + \Delta z, t). \tag{2.61}$$

The integrals of the electric field strength in the longitudinal-direction considering imperfect conductors can be rewritten as:

$$-\int_{a_1}^{b_1} \mathbf{E}_\ell \cdot d\mathbf{l} = -R_1 \Delta z I(z,t)$$

$$-\int_{b_0}^{a_0} \mathbf{E}_\ell \cdot d\mathbf{l} = -R_0 \Delta z I(z,t) \tag{2.62}$$

where R_1 and R_0 are the per-unit-length resistances of the conductors.

Substituting (2.61) and (2.62) in (2.60) and dividing by Δz leads to:

$$\frac{U(z+\Delta z,t)-U(z,t)}{\Delta z} = -(R_1 + R_0)I(z,t) - \mu \frac{1}{\Delta z}\frac{d}{dt}\int_S \mathbf{H}_{tr} \cdot d\mathbf{S}. \qquad (2.63)$$

The magnetic flux per-unit-length can be written as:

$$\psi = \mu \lim_{\Delta z \to 0}\frac{1}{\Delta z}\frac{d}{dt}\int_S \mathbf{H}_{tr} \cdot d\mathbf{S} = LI(z,t) \qquad (2.64)$$

with L denoting the per-unit-length inductance.

Using (2.64) in (2.63) and applying $\Delta z \to 0$ leads to the first transmission line equation:

$$\frac{\partial U(z,t)}{\partial z} = -RI(z,t) - L\frac{\partial I(z,t)}{\partial t} \qquad (2.65)$$

where R equals $R_1 + R_0$.

For the second transmission-line equation, a closed surface S' is placed around the second conductor where S'_ℓ denotes the part of the surface with is normal component pointing in the longitudinal direction and S'_{tr} denotes the part of the surface with its normal component pointing to the sides of the conductor, as depicted in Fig. 2.3.
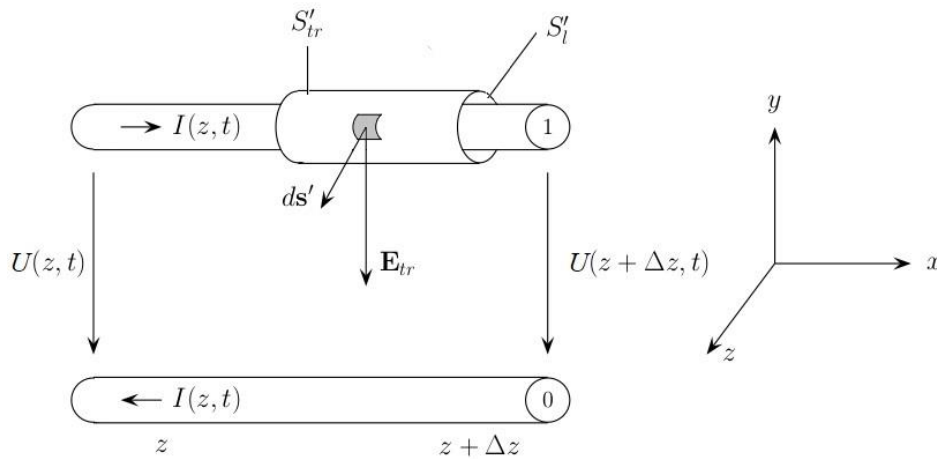
Fig. 2.3: Two-conductor system for second transmission-line equation

The second transmission-line equation can then be derived from the equation of conservation of charge:

$$\oiint_{S'} \mathbf{J} \cdot d\mathbf{S}' = -\frac{d}{dt}q_{enc}. \qquad (2.66)$$

In the longitudinal-direction, through the surface S_ℓ, this results into

$$\iint_{S'_\ell} \mathbf{J} \cdot d\mathbf{S}' = I(z+\Delta z,t) - I(z,t). \tag{2.67}$$

Between the two conductors a transverse conduction current is flowing and this leads to

$$\iint_{S'_{tr}} \mathbf{J}_c \cdot d\mathbf{S}' = \sigma \iint_{S'_{tr}} \mathbf{E}_{tr} \cdot d\mathbf{S}'. \tag{2.68}$$

The enclosed charge per unit length by the surface can be determined by Gauss's law

$$q_{enc} = \varepsilon \iint_{S'_{tr}} \mathbf{E}_{tr} \cdot d\mathbf{S}'. \tag{2.69}$$

Substituting (2.67)-(2.69) in (2.66) and dividing by Δz leads to:

$$\frac{I(z+\Delta z,t) - I(z,t)}{\Delta z} = -\sigma \frac{1}{\Delta z} \iint_{S'_{tr}} \mathbf{E}_{tr} \cdot d\mathbf{S}' - \varepsilon \frac{1}{\Delta z} \iint_{S'_{tr}} \mathbf{E}_{tr} \cdot d\mathbf{S}'. \tag{2.70}$$

G is defined as the per-unit-length conductance between the two conductors

$$\sigma \lim_{\Delta z \to 0} \frac{1}{\Delta z} \iint_{S'_{tr}} \mathbf{E}_{tr} \cdot d\mathbf{S}' = GU(z,t) \tag{2.71}$$

and the per-unit-length capacitance C defines the charge per unit line length between the two conductors.

$$\varepsilon \lim_{\Delta z \to 0} \frac{1}{\Delta z} \iint_{S'_{tr}} \mathbf{E}_{tr} \cdot d\mathbf{S}' = CU(z,t) \tag{2.72}$$

Substituting (2.71) and (2.72) in (2.70) and applying $\Delta z \to 0$ leads to the second transmission line equation:

$$\frac{\partial I(z,t)}{\partial z} = -GU(z,t) - C\frac{\partial U(z,t)}{\partial t}. \tag{2.73}$$

Now the per-unit-length equivalent circuit of the two-conductor transmission-line can be assembled and it is depicted in Fig 2.4.
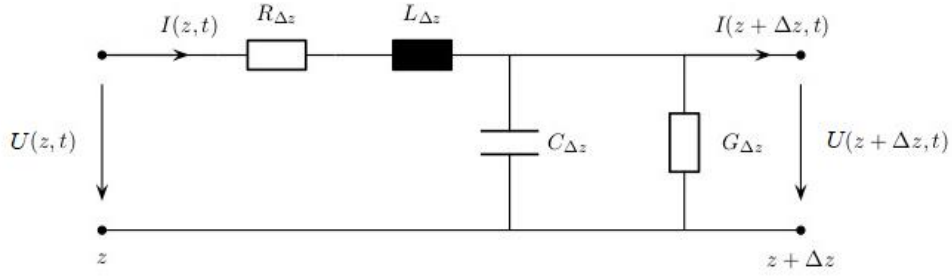
Fig. 2.4: Equivalent circuit for two-conductor transmission-line problem

In case of multi-conductor transmission-lines, the equations are quite similar to (2.65) and (2.73):

$$\frac{\partial}{\partial z}\mathbf{U}(z,t) = -\mathbf{R}\mathbf{I}(z,t) - \mathbf{L}\frac{\partial}{\partial t}\mathbf{I}(z,t)$$

$$\frac{\partial}{\partial z}\mathbf{I}(z,t) = -\mathbf{G}\mathbf{U}(z,t) - \mathbf{C}\frac{\partial}{\partial t}\mathbf{U}(z,t).$$

(2.74)

The difference in this case is that the per-unit-length parameters are matrices instead of scalars and also include couplings between single conductors.

The equivalent circuit of the multi-conductor transmission-line is shown in Fig 2.5.
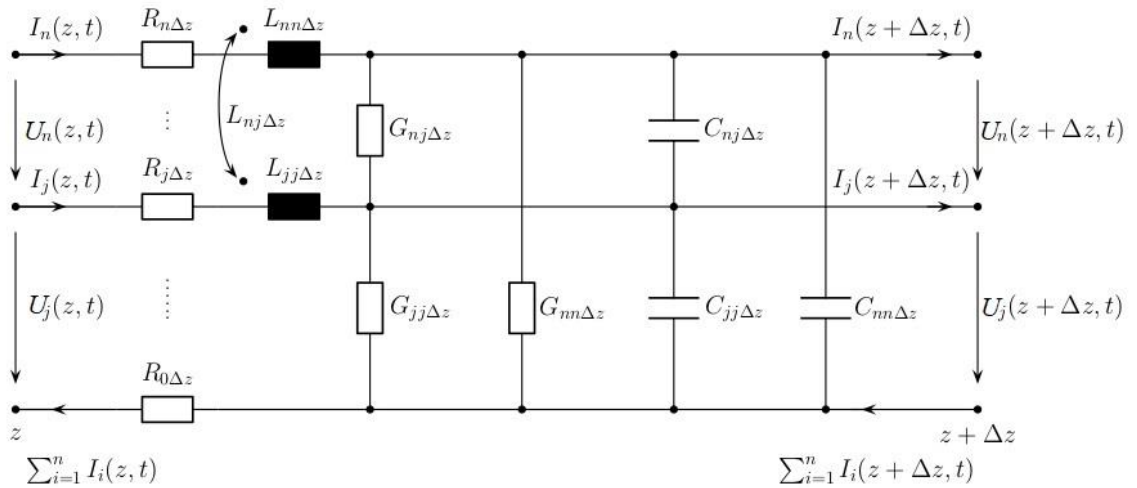
Fig. 2.5: Equivalent circuit for multi-conductor transmission-line problem

2.4.2 Lumped circuit approach

As already mentioned at the beginning of this section, the dimensions of the cross section of the setup have to be electrically short with respect to the wavelength corresponding to the highest frequency of the excitation.

The lengths of the simulated segments have to meet this criterion as well. The segment is considered to be electrically short if the following condition is met for the maximum line length $\mathcal{L}$:

$$\mathcal{L} < \frac{\lambda}{10} \tag{2.75}$$

where $\lambda = \dfrac{c}{f_{max}}$ is the minimum wavelength present, c here it the speed of light and f_{max} is the maximum operating frequency of a given problem setting.

In case the length of the simulated segment is longer than the maximum line length $\mathcal{L}$, the line can be divided into smaller segments, where every single segment then is electrically short.

The per-unit-length parameters for a given setup can be derived from the geometry information of the cross-section. For simpler structures the parameters can be calculated analytically and especially for wire-type structures the formulas are very precise.

In case of more complex geometries, analytical approaches are often not possible anymore and parameter extraction can be done with numerical methods as for example the finite element method as it is used in this work.

3   Transfer Impedance: Basics and analytical approach

The transfer impedance Z_t is a shield effectiveness parameter to characterize the performance of a cable shield and was first introduced by Schelkunoff [18] for solid coaxial transmission lines. It describes the shielding effectiveness in terms of electromagnetic immunity and emission. A lower transfer impedance translates into a better shielding effectiveness, this means lower emission from the cable itself, less interference with its surroundings and less induced noise inside the cable with respect to an external electromagnetic interference (EMI) source in terms of immunity.

3.1   Braided cable shields

This section provides a short overview regarding the most important parameters characterizing a braided shield which will also be important in chapter 4 for modelling the geometry with the finite element method.

The basic geometry of a coaxial cable is defined by the diameter of the inner conductor, the distance from the inner conductor to the shield and the shield thickness. The permittivity of the dielectric of a cable is a highly relevant material property for the cable characteristics. These parameters are also relevant for the fundamental electrical parameters and the characteristic impedance of a coaxial cable which stand in direct correlation. Usually the standard coaxial cables have a characteristic impedance of 50Ω or 75Ω.

Besides this basic geometry, the composition of the shield has to be evaluated in a more detailed manner. The main parameters defining a braided cable shield can be divided into geometry dependencies and material dependencies.

The important geometry parameters are shield thickness and the rhomboid shaped apertures of the shield, which are mainly determined by the weave angle in shape and size.

Another important characteristic is the so called optical coverage factor, which describes the amount of coverage of the shield. A solid shield, for example, has an optical coverage factor of 100%. The rhombic shaped apertures of a braided shield result into a coverage factor of less than 100% and therefore the size and the number of apertures is a defining factor for the shield quality, since a higher coverage factor translates into a

better shielding effectiveness. A sample picture of the defining geometry is given in Fig. 3.1 for standard coaxial cables with typical coverage factors of 85% to 98%.

In Fig. 3.1 on the right, more parameters like the number of carriers, the number of filaments per carrier and the filament diameter are visible, but these parameters have not been taken into consideration, neither for the analytical investigation nor the finite element model and the carriers are assumed to be made of solid conducting material.

Despite this simplification the simulated results, compared to measurements that are done in chapter 5, will be seen to stand in good agreement.

The reference model in this case is a standard RG58/CU coaxial cable with a nominal characteristic impedance of 50Ω which is used to verify the simulated results with measurements. For this cable the material of the shield and the inner conductor is copper.
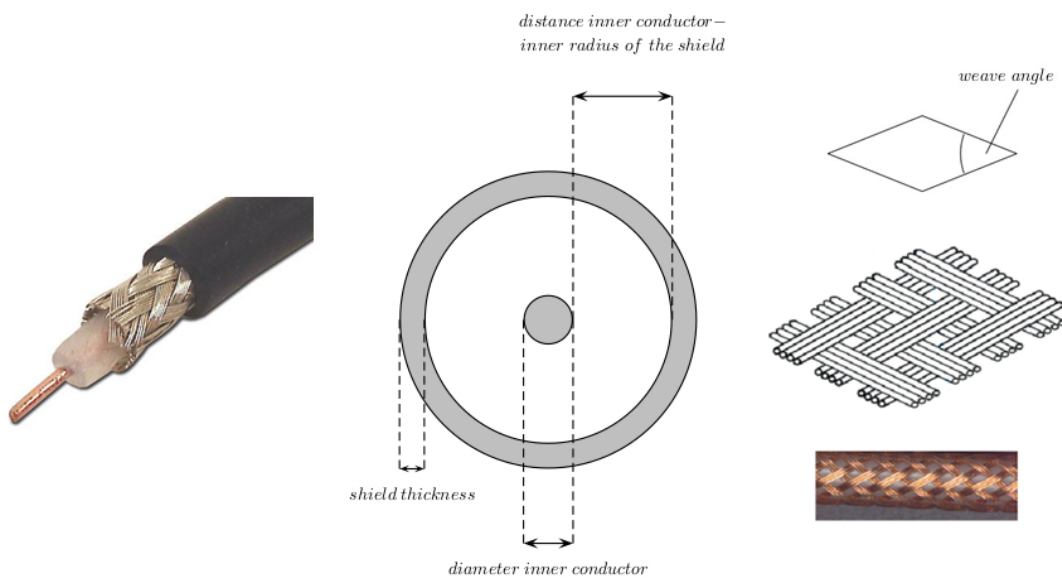
Fig. 3.1: Sample of geometry parameters of braided cable shields

The geometry- and material parameters of this coaxial cable are given as:

Geometry parameters:

- Diameter of inner conductor: 0.90mm

- Inner diameter of shield: 2.95mm

- Outer diameter of shield: 3.55mm

- Shield thickness: 0.3mm

- Coverage factor: 95%

- Weave angle: 20° to 30°

Material parameters:

- Conductors: copper with a conductivity of 58MS/m

- Dielectric: Polyethylene

3.2 Characteristic impedance

It has to be mentioned that the transfer impedance is not to be confused with the characteristic impedance of a coaxial cable. The transfer impedance describes the energy propagation through the shield along the cable and the characteristic impedance defines the properties along the cable with respect to signal propagation [19].

The characteristic impedance Z_0 is only dependent on the basic geometry of the cable and for non-braided coaxial cables, it is derived as

$$Z_0 = \sqrt{\frac{L'}{C'}} \tag{3.1}$$

where L' is the per-unit-length inductance and C' the per-unit-length capacitance of the cable and these parameters are derived as

$$L' = \frac{\mu_0 \mu_r}{2\pi} ln \frac{D}{d} \quad \text{H/m}$$

$$C' = \frac{2\pi \varepsilon_0 \varepsilon_r}{ln \frac{D}{d}} \quad \text{F/m}$$

(3.2)

where μ_0 and μ_r denote the vacuum- and relative permeability, ε_0 and ε_r denote the vacuum- and relative permittivity and d gives the diameter of the inner conductor and D is the outer diameter of the shield. From (3.1) and (3.2) it is visible that the characteristic impedance is mainly dependent on the basic geometry, namely on the size ratio of the diameters of the inner- and outer conductors.

3.3 Definition of transfer impedance

The transfer impedance of any shielded cable can be defined as in (3.3) as the ratio between the transferred voltage per unit length on the external surface of the shield U'_{ext}, which is measured in Volt per meter and the longitudinal current I_0 on the internal side of the shield, as in [19] and [20], and therefore, the transfer impedance is measured in Ohms per meter.

Fig. 3.2 depicts the general evaluation setup as is used throughout this work. A known electromagnetic interference current (EMI-current) I_0 is applied to the inner circuit formed by the inner conductor of the cable and the shield and this current generates the differential transfer voltage U'_{ext} on the outer side of the shield which leads to the definition of the transfer impedance as

$$Z_t = \frac{1}{I_0} U'_{ext}.$$ (3.3)

The external transfer voltage U'_{ext} represents the energy transfer from the inside to the outside of the shield and therefore the transfer impedance is a per unit length parameter that describes the energy losses propagating along the cable through the shield.
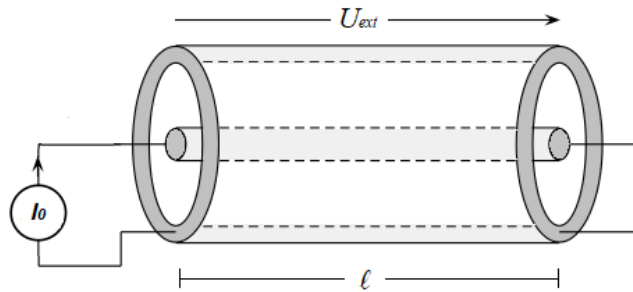
Fig. 3.2: General evaluation setup for transfer impedance

The transfer impedance, being the ratio of the voltage U'_{ext} and the current I_0, with both parameters not dependent on the surroundings but only on the shield composition, can be considered to be a pure characteristic of the cable itself, only depending on the material properties and the geometry.

It is also correlated to the inductive coupling since the interference current I_0 is related to the magnetic field. In case of perforated shields, there is a capacitive coupling, too

because the normal component of the electric field acts directly through the apertures which is described via the transfer admittance parameter.

Fig. 3.3 shows the result of the numerical simulation and depicts the principal behaviour of the transfer impedance of a braided cable shield with respect to the frequency. The curve shape can be coarsely divided into three particular regions, depending on the frequency:

The DC-region describes the behaviour for low frequencies and equals the DC-resistance of the shield. With increasing frequency, it passes over to the region where the skin effect losses predominate. At higher frequencies, the inductive region prevails due to the aperture leakage of the shield.
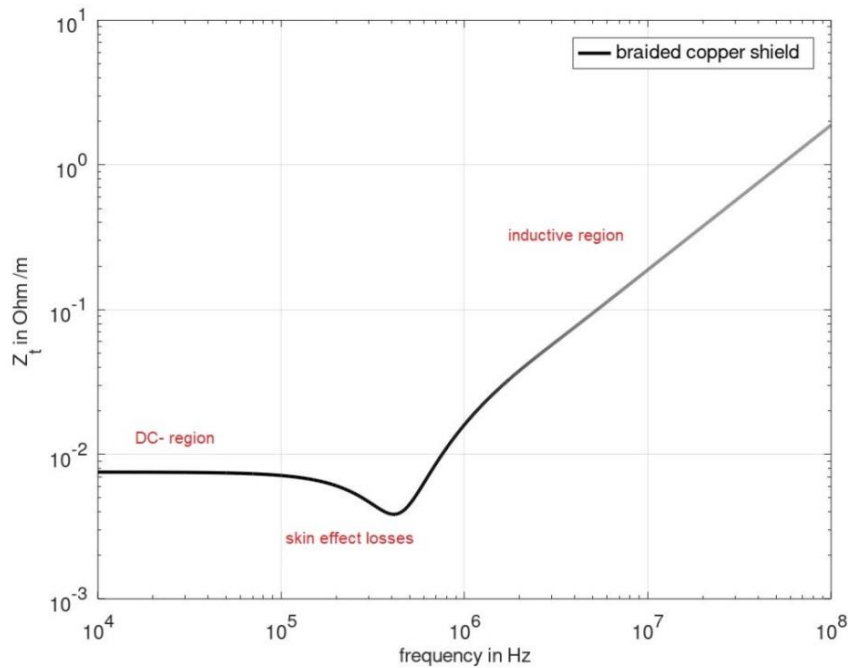
Fig. 3.3: Classification of predominant regions of the transfer impedance with respect to the frequency

3.4 DC-region and skin effect losses

The transfer impedance is highly frequency dependent due to the phenomenon called skin effect. Since for this problem, the skin depth is not considered to be small with respect to the thickness of the shield, the current density can be modelled with Bessel functions.

Different skin depths for a solid copper shield with a shield thickness of 0.3mm are shown in Fig. 3.4 for frequencies of 50kHz on the left side and for 5MHz on the right.
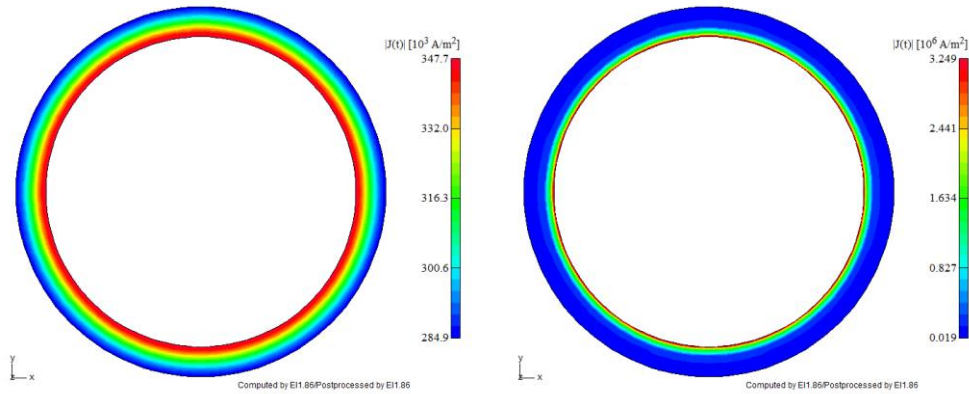
Fig. 3.4: Frequency dependence of skin depth in solid copper shield of 0.3mm shield thickness at 50kHz and 5MHz.

With increasing frequency, the current density is seen to concentrate more and more on the inner side of the shield and this leads to a decreasing voltage on the outside of the solid shield, resulting in the decrease of the transfer impedance.

For lower frequencies the transfer impedance equals the DC-resistance of the shield and, at a specific frequency, the transfer impedance starts to decrease due to the afore-mentioned skin effect. This cut-off frequency is material- and geometry dependent and this will be discussed in chapter 6 in more detail.

The curve shape of the transfer impedance of a solid copper shield over the operating frequency is depicted in Fig. 3.5.
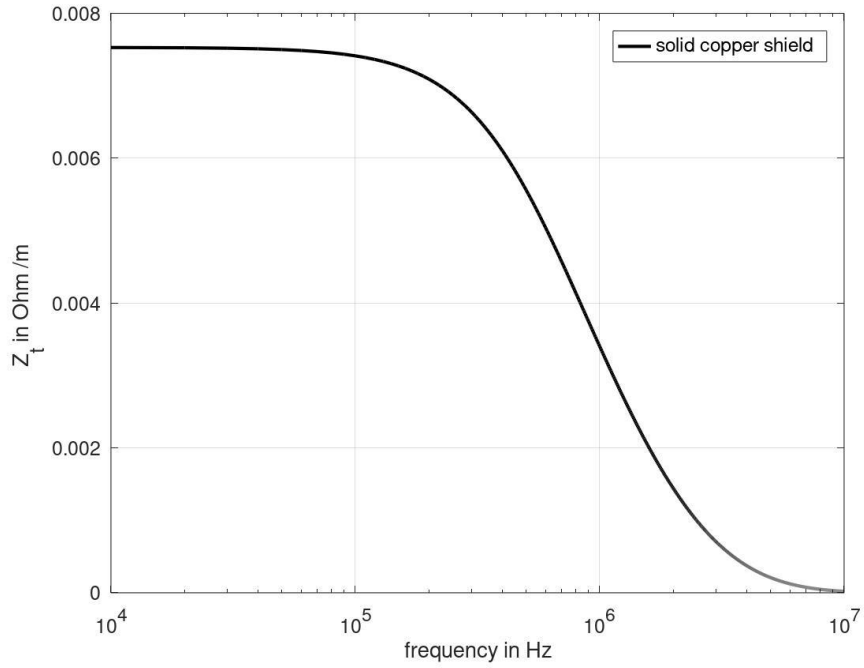
Fig. 3.5: Transfer impedance of a solid copper shield

3.4.1 Analytical model for the solid shield

The current distribution of the magnetic field inside a conductor is derived from Ampere's law (2.11), and the constitutive relations (2.14) as

$$\nabla \times (\nabla \times \mathbf{H}) = \sigma(\nabla \times \mathbf{E}). \tag{3.4}$$

Together with Faraday's law of induction (2.13) and (2.14) this leads to the equation

$$\nabla^2 \mathbf{H} = j\omega\sigma\mu\mathbf{H}. \tag{3.5}$$

For a straight cylindrical conductor with a given radius r this problem is solved with the magnetic field, leading to Bessel's equation

$$\frac{\partial}{\partial r}\left[\frac{1}{r}\frac{\partial}{\partial r}(rH_\phi)\right] = \gamma^2 H_\phi \tag{3.6}$$

with its solution

$$H_\phi = AI_1(\gamma r) + BK_1(\gamma r). \tag{3.7}$$

The relation between the current and the magnetic field for this problem in cylindrical coordinates is derived from (2.11) and is given as

$$J_z = \frac{1}{r} \frac{\partial}{\partial r} (r H_\phi) \tag{3.8}$$

again applying the constitutive relations from (2.14) and substituting the derivative of (3.7) leads to

$$E_z = \frac{\gamma}{\sigma} [A I_0 (r\gamma) - B K_0 (r\gamma)] \tag{3.9}$$

with $\gamma = \sqrt{j\omega\mu\sigma}$, $I_1(x)$ and $K_1(x)$ denote the first-order modified Bessel-functions of the first and second kind and $I_0(x)$ and $K_0(x)$ denote the zero-order modified Bessel-functions of the first and second kind.

A and B are constants, that are evaluated now for the solid shield with an inner radius $r = a$ and an outer radius $r = b$.

The current return path can be provided either inside or outside the shield which leads to the surface impedances Z_{aa} respectively Z_{bb} (3.13) for the internal and the external return. The impedance $Z_t = Z_{ab} = Z_{ba}$ (3.14) denotes the transfer impedance from one surface of the shield to the other [18], [19].

To derive the unknown constants A and B from (3.9), a known total current $I_a + I_b$ is assumed, flowing in the solid cylindrical shield, where I_a denotes the current of the internal return and I_b is the part of the current returning on the outside, as depicted in Fig. 3.6.
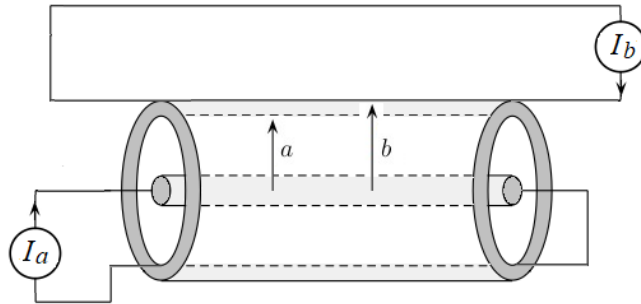
Fig. 3.6: Definition of currents I_a and I_b for evaluation of the transfer impedance of a solid shield

The current enclosed by the inner surface is $-I_a$ and applying Ampere's law (2.11), this results in $H_{\phi a} = -\dfrac{I_a}{2\pi a}$. I_b is the current enclosed by the outer surface, which analogously leads to $H_{\phi b} = \dfrac{I_b}{2\pi b}$.

Substituting $H_{\phi a}$ and $H_{\phi b}$ in (3.7), for the inner- and outer radius of the shield, gives the following equations

$$AI_1(\gamma a) + BK_1(\gamma a) = -\frac{I_a}{2\pi a}$$
$$AI_1(\gamma b) + BK_1(\gamma b) = \frac{I_b}{2\pi b}$$

(3.10)

and the constants A and B can be derived as:

$$A = I_a \frac{K_1(\gamma b)}{2\pi aD} + I_b \frac{I_1(\gamma a)}{2\pi bD}$$

(3.11)

$$B = -I_a \frac{I_1(\gamma b)}{2\pi aD} - I_b \frac{I_1(\gamma a)}{2\pi bD}$$

where $D = [I_1(\gamma b)K_1(\gamma a) - I_1(\gamma a)K_1(\gamma b)]$.

Substituting (3.11) in (3.9) leads to

$$E_z(a) = Z_{aa}I_a + Z_{ab}I_b$$

(3.12)

$$E_z(b) = Z_{bb}I_b + Z_{ba}I_a$$

where Z_{aa} is the surface impedance with the internal return and Z_{bb} is the surface impedance with external return and they are evaluated as:

$$Z_{aa} = \frac{j\omega\mu}{\gamma} \frac{1}{2\pi aD}[I_0(\gamma a)K_1(\gamma b) + K_0(\gamma a)I_1(\gamma b)]$$

(3.13)

$$Z_{bb} = \frac{j\omega\mu}{\gamma} \frac{1}{2\pi bD}[I_0(\gamma b)K_1(\gamma a) + K_0(\gamma b)I_1(\gamma a)]$$

and the transfer impedance Z_t from one surface of the shield to the other is given as

$$Z_t = Z_{ab} = Z_{ba} = \frac{1}{2\sigma abD} = \frac{1}{2\pi\sigma ab[I_1(\gamma b)K_1(\gamma a) - I_1(\gamma a)K_1(\gamma b)]}. \quad (3.14)$$

Using the following approximation of the modified Bessel functions for the asymptotic behaviour for small arguments $0 < x \leq \sqrt{n+1}$:

$$I_n(x) \approx \frac{1}{\Gamma(n+1)}\left(\frac{x}{2}\right)^n$$

$$(3.15)$$

$$K_n(x) \approx \begin{cases} -\left(\ln\left(\frac{x}{2}\right) + \gamma\right) ... n = 0 \\ \dfrac{\Gamma(n)}{2}\left(\dfrac{2}{x}\right)^2 ... n > 0 \end{cases}$$

(3.14) leads to the DC-resistance of the solid cable shield

$$R_{dc} = \frac{1}{\pi\sigma(b+a)(b-a)} \quad (3.16)$$

and using the approximation of the modified Bessel functions for the asymptotic behaviour for large arguments $x >> |n^2 - 0.25|$

$$I_n(x) \approx \frac{1}{2\pi x}e^x$$

$$(3.17)$$

$$K_n(x) \approx \sqrt{\frac{\pi}{2x}}e^{-x}$$

(3.14) leads to the transfer impedance Z_t of the solid shield

$$Z_t = \frac{\gamma}{2\pi\sigma\sqrt{ab}\,sinh(\gamma d)} \quad (3.18)$$

with d being $(b-a)$, i.e. the shield thickness.

3.5 Inductive region

In the case of braided shields, we can identify the DC-region and the skin effect losses but at higher frequencies the inductive behaviour of the apertures of the shield is predominant and lead to a rise of the transfer impedance as depicted in Fig. 3.3.

The reason for this inductive behaviour is the so called aperture leakage that arises from the geometry of the shield. The cable shield protects against external EMI fields and it also protects against the leakage effects from the inner part of the cable. This shielding effectiveness is reduced by the apertures in the shield. The resulting inductive behaviour is strongly geometry dependent.

For this investigation, the problem setting is considered to be in the low-frequency domain, which means that the apertures are relatively small with respect to the wavelength and therefore the geometry is electrically short [21].

3.5.1   Analytical model for inductance calculation

To calculate the aperture leakage, an electric dipole source with its dipole moment $\mathbf{p}_a$ perpendicular to the aperture and a magnetic dipole source with its dipole moment $\mathbf{m}_a$ in the aperture plane, located at the centre of the aperture, are assumed.

These dipole sources generate an electric-dipole field as well as a magnetic-dipole field. According to [22], the first-order diffracted field by small apertures can be described as the superposition of the two fields.

To obtain the dipole moments, the rhombic apertures of the shield are approximated via elliptic apertures that are assumed to be in a conducting plane.

The magnetic dipole moment is then derived from the static magnetic dipole moment of an ellipsoidal magnetic body that is placed in a uniform static magnetic field as depicted in Fig. 3.7 on the right. The static magnetic dipole moment components can be calculated as

$$m_x = \frac{V}{L_x + \frac{\mu_0}{(\mu - u_0)}} H_x \tag{3.19}$$

due to the field H_x along the ℓ_x - axis and

$$m_y = \frac{V}{L_y + \frac{\mu_0}{(\mu - u_0)}} H_y \tag{3.20}$$

due to the field H_y along the ℓ_y - axis, as described in [24].

The electric dipole moment is derived from the static dipole moment of a dielectric body that is placed in a uniform static electric field E_0 along the ℓ_z-axis, as depicted in Fig. 3.7 on the left and the dipole moment p_z is calculated as [24]:

$$p_z = \frac{\varepsilon_0 V}{L_z + \dfrac{\varepsilon_0}{(\varepsilon - \varepsilon_0)}} E_0 \tag{3.21}$$

where V is the volume of the ellipsoid.
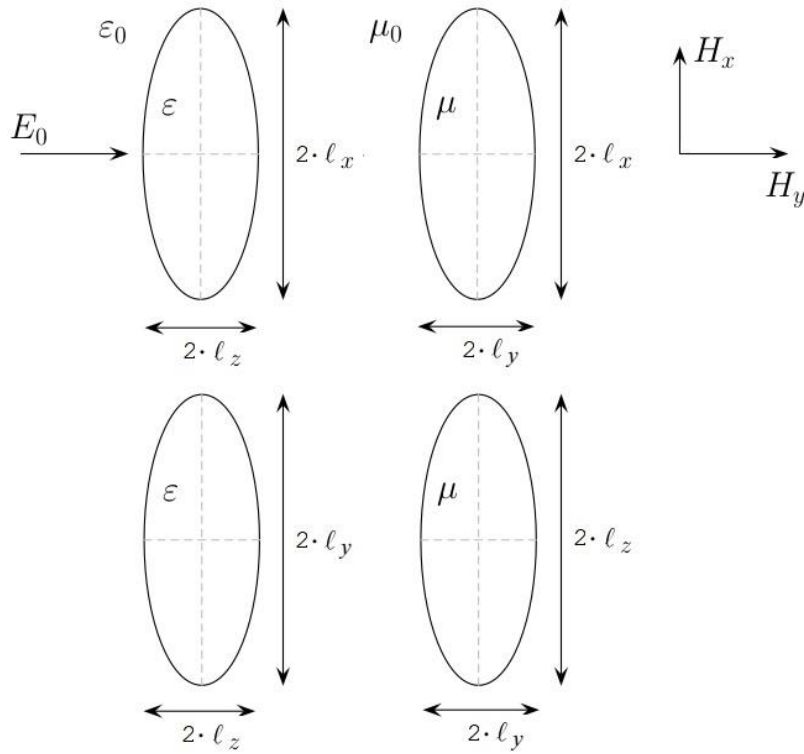
Fig. 3.7: Dielectric ellipsoid on the left and permeable magnetic ellipsoid on the right

The integrals for the constants L_n are calculated by the aid of appropriate limiting processes as in [23] and [24]:

$$L_n = \frac{\ell_x \ell_y \ell_z}{2} \int_{\ell_n}^{\infty} \frac{ds}{(s + \ell_n^2)\sqrt{(s + \ell_x^2)(s + \ell_y^2)(s + \ell_z^2)}} \tag{3.22}$$

for $n = x, y$ and z and ℓ_x, ℓ_y, ℓ_z are the ellipsoid semi-axes.

Using (3.22), the static dipole moment then can be evaluated from (3.19) – (3.21) as

$$m_x = \frac{4}{3}\pi\ell_x^{\ 3}\frac{e^2}{[K(e)-E(e)]}H_x \tag{3.23}$$

$$m_y = \frac{4}{3}\pi\ell_x^{\ 3}\frac{e^2(1-e^2)}{E(e)-(1-e^2)K(e)}H_y \tag{3.24}$$

$$p_z = -\frac{4\pi\ell_x^{\ 3}}{3}\frac{(1-e^2)}{E(e)\varepsilon_0}E_z \tag{3.25}$$

where $K(e)$ and $E(e)$ are the complete elliptic integrals of the first and of the second kind, respectively and

$$e = \sqrt{1-\frac{\ell_y^{\ 2}}{\ell_x^{\ 2}}}, \ell_x > \ell_y \tag{3.26}$$

defines the eccentricity of the elliptic aperture.

The effective dipole moments

$$\mathbf{m}_e = \frac{1}{4}\mathbf{m} = \bar{\bar{\alpha}}_m \cdot \mathbf{H} \tag{3.27}$$

$$\mathbf{p}_e = \frac{1}{4}\mathbf{p} = \varepsilon_0\alpha_e\mathbf{nnE} \tag{3.28}$$

result in the dyadic magnetic polarizabilities:

$$\alpha_{mx} = \frac{\pi\ell_x^{\ 3}}{3}\frac{e^2}{[K(e)-E(e)]} \tag{3.29}$$

$$\alpha_{my} = \frac{\pi\ell_x^{\ 3}}{3}\frac{e^2(1-e^2)}{E(e)-(1-e^2)K(e)} \tag{3.30}$$

$$\alpha_{mxy} = \alpha_{myx} = 0 \tag{3.31}$$

and the electric polarizability

$$\alpha_e = -\frac{\pi\ell_x^{\ 3}}{3}\frac{(1-e^2)}{E(e)\varepsilon_0}. \tag{3.32}$$

The effective aperture inductance of a single aperture can then be evaluated as:

$$L_x = \alpha_{mx} \frac{\mu_0}{(2\pi r)^2},$$

$$L_y = \alpha_{my} \frac{\mu_0}{(2\pi r)^2}$$

(3.33)

where r is the radius of the conducting tubular screen.

3.6 Applicable analytical model

The analytical approximation methods in general to describe the different regions of the transfer impedance and their practical use have been studied in [26]-[30]. An overview of those methods is also presented in [25]. The drawback of those models lies in the fact that the results are mainly compared to measurements and therefore more excessive geometry variations have not been studied in detail.

In the following sections the adjustment procedures for the applicable analytical model are described. These adaptions are needed, since on the one hand, the coverage factor has a direct influence on the DC-region respective the DC-resistance, which is not taken into consideration for the solid shield in section 3.4.

On the other hand, the inductance calculation of the apertures by approximating the rhombic shapes with ellipses, as it is done in section 3.5.1, leads to an overestimated inductance value, which will be explained in section 3.6.2.

3.6.1 DC-region and skin effect losses

For calculating the DC-resistance including the skin-effect losses, the analytical approach of Schelkunoff [18] for solid cable shields, as mentioned before, provides very accurate and stable results. Comparing the analytically derived values and the numerical results shows that, to gather the correct DC-resistance, mainly the optical coverage factor of the given shield has to be taken into consideration additionally which leads to an increase of the resistance value since the effective area for the current flow decreases.

In this case (3.14) leads to:

$$Z_t = \frac{1}{CF_{opt}} \cdot \frac{1}{2\pi\sigma ab[I_1(\gamma b)K_1(\gamma a) - I_1(\gamma a)K_1(\gamma b)]}$$

(3.34)

where the factor CF_{opt} describes the optical coverage of the cable shield.

3.6.2 Inductive region

As mentioned before, to calculate the aperture leakage the rhombic openings of the braided cable shield are approximated via ellipsoids. Using the same length of the main- and semi axis for this approximation leads to an overestimation of the calculated value. To obtain better results, the magnetic polarizability can be written as in [31]-[34]

$$\alpha_m = \mu_m S^{\frac{3}{2}} \tag{3.35}$$

where S is the surface of the rhombic aperture, α_m is the magnetic polarizability from (3.29) and (3.30) and μ_m represents the dimensionless magnetic polarizability.

Using this representation, the dimensionless magnetic polarizabilities can be re-written as

$$\mu_{mx} = \frac{2}{3 \cdot \sqrt{\pi}} \left(\frac{\ell_x}{\ell_y} \right)^{\frac{3}{2}} \frac{e^2}{[K(e) - E(e)]} \tag{3.36}$$

for angles $\beta = arctan\left(\dfrac{\ell_x}{\ell_y} \right) > 45°$ and $e = \sqrt{1 - \dfrac{\ell_y^{\,2}}{\ell_x^{\,2}}}, \ell_x > \ell_y$ which translates into weave angles of $\alpha < 90°$ and

$$\mu_{my} = \frac{2}{3 \cdot \sqrt{\pi}} \left(\frac{\ell_y}{\ell_x} \right)^{\frac{3}{2}} \frac{e^2}{E(e) - (1 - e^2)K(e)} \tag{3.37}$$

for $\beta = arctan\left(\dfrac{\ell_x}{\ell_y} \right) < 45°$ and $e = \sqrt{1 - \dfrac{\ell_x^{\,2}}{\ell_y^{\,2}}}, \ell_y > \ell_x$, which translates to weave angles $\alpha > 90°$.

The two different cases for the weave angle α are shown in Fig. 3.8.
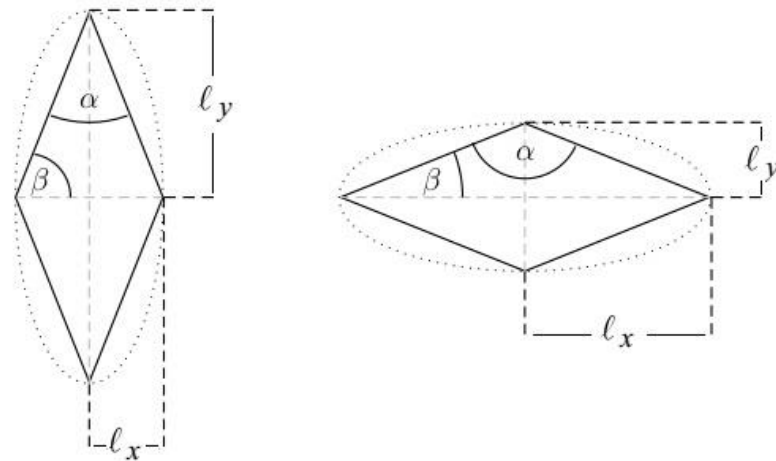
Fig. 3.8: Approximation of rhombic apertures with ellipses

The effective aperture inductance of a single aperture is then evaluated similarly as in (3.33):

$$L_x = \mu_{mx} \frac{\mu_0}{(2\pi b)^2}$$

$$L_y = \mu_{my} \frac{\mu_0}{(2\pi b)^2}$$

(3.38)

where b is the outer radius of the shield taking the shield thickness respectively the basic geometry into consideration.

The analytical results for these hole-inductance values are compared to results of the FEM-model which will be explained in more detail in chapter 5.

The comparisons are depicted in Fig. 3.9 for weave angles $\alpha < 90°$ and in Fig. 3.10 for angles $\alpha > 90°$ and the results stand in very good agreement.
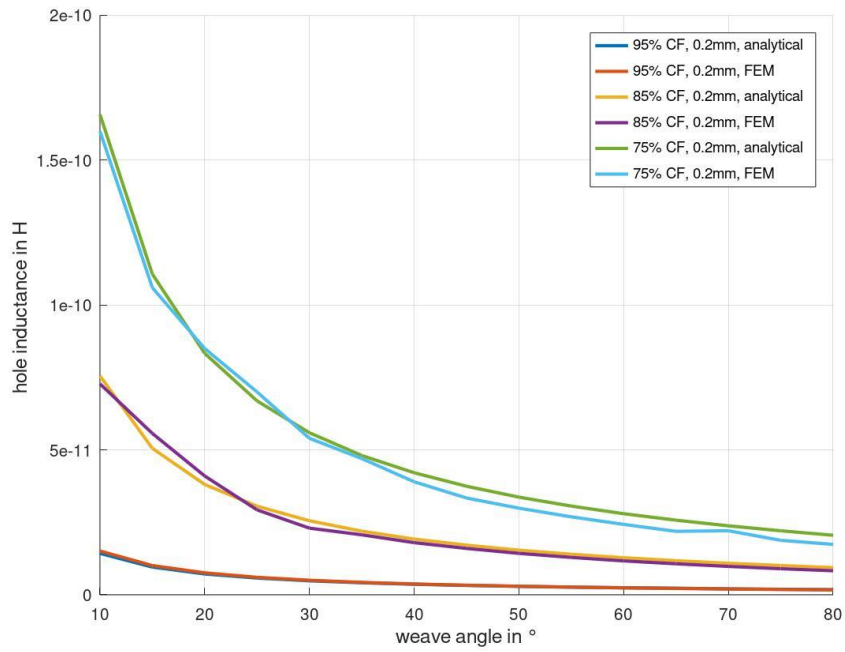
Fig. 3.9: Comparison of hole inductance for weave angles $\alpha < 90°$, FEM vs analytical
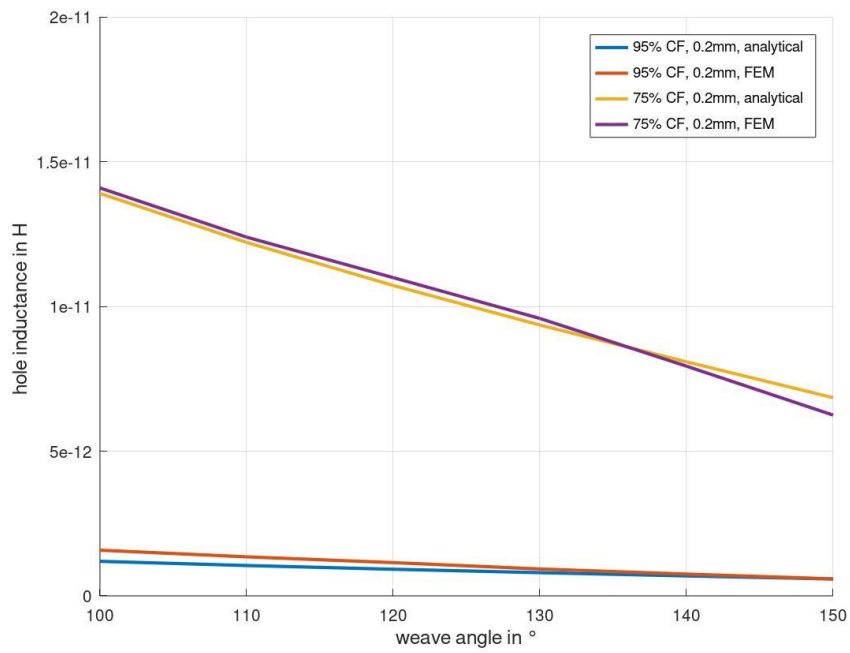
Fig. 3.10: Comparison of hole inductance for weave angles $\alpha > 90°$, FEM vs analytical

3.6.3   Cable shield with multiple apertures

To gather the hole-inductance per unit length, the value in (3.38) has to be multiplied with the number of apertures per meter of the cable shield [16].
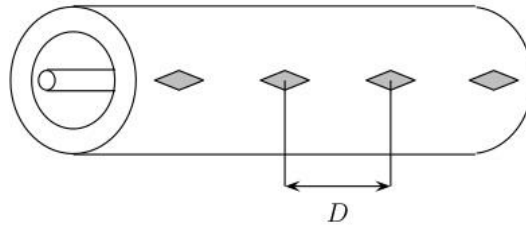
Fig. 3.11: Definition of hole-distance for multiple apertures

For a cable shield with n apertures at an average distance D between the neighbouring apertures as depicted in Fig. 3.11, the hole-inductance per unit length can be derived as:

$$
\begin{aligned}
L_{xn} &= \frac{1}{D} L_x = nL_x \; H/m \\
L_{yn} &= \frac{1}{D} L_y = nL_y \; H/m
\end{aligned}
\tag{3.39}
$$

A more detailed analysis on the influence of different parameters on the overall transfer impedance is carried out in chapter 6 by the use of sensitivity analysis.

4 FEM model for transfer impedance of braided cable shields

This chapter gives a short introduction of the software tool used and describes how the FEM-model of the parametrized cable model has been implemented.

As mentioned before, the transfer impedance is not only frequency dependent, but geometry- and material parameters have strong influence on the shielding behaviour of a given cable shield.

This chapter will take a closer look at the geometry dependencies with the help of the finite element method. The advantages of numerical simulations are that these parameter variations can be modelled exactly and they give a more precise evaluation model for the analytical calculations. Even though the analytical model is verified by measurements in section 5.3, based on the implemented FEM-model, more influences can be investigated without the need to fabricate special cables and run extensive measurements.

Using numerical simulations also gives the ability to investigate cable deformations such as bending and stretching of the cable shield and the influence of the resulting geometry deviations on the shielding effectiveness.

For the FEM-model, the basic geometry parameters like diameter of the inner conductor, the distance from the inner conductor to the inner radius of the shield and the shield thickness can be varied. For the cable shield, the weave angle and the coverage factor are parametrized as well. This model works in the range of a coverage factor from 60% to a full coverage of 100% which translates into a solid shield. These parameters should suffice since coverage factors of 90% and higher are very common values for typical coaxial cables.

As also mentioned before, the conductors of this cable are made of copper but this material parameter can be varied for this model as well.

It has to be noted, that changing the basic geometry parameters like the distance from the inner conductor to the outer radius of the shield are used to evaluate the influences of these parameter variations on the shielding effectiveness. Changing these parameters will lead to a change in the characteristic impedance of a coaxial cable as is mentioned

in section 3.2. The possible changes on the signal propagation properties, arising with these parameter variations, are not under investigation in this work.

The reference model in this case is a standard RG58/CU coaxial cable, as mentioned in chapter 3, which is used to verify the simulated results with measurements. A more detailed description of the measurement setup and novelties of the same are discussed in chapter 5.

For the numerical simulation, the **A**,V-**A**-formulation with current excitation is used, as it is described in chapter 2, since for the evaluation of the transfer impedance, i.e. the voltage on the outer side of the shield, a known EMI-current is needed, as seen in (3.1).

4.1 Space discretization using finite elements: EleFAnT3D

The software package **Ele**ctromagnetic **F**ield **An**alysis **T**ool (EleFAnT3D) [26] is used to solve this three-dimensional electromagnetic problem.

The whole domain is divided into smaller subdomains, the so called finite elements, over which simple basis functions are defined to approximate the solution. The software package uses 2nd order hexahedral elements that are defined via 20 nodes and 36 edges and the unknown functions are represented on a nodal basis or on an edge basis.

In the case of node based elements the unknown scalar- and vector functions are approximated in the nodes that are associated with the element. Using continuous and piecewise polynomial basis functions that satisfy

$$N_j = \begin{cases} 1 & \text{at node } j \\ 0 & \text{at all other nodes} \end{cases} \tag{4.1}$$

lead to the interpolated solution.

The basis functions can be expressed in terms of local coordinates (ξ, η, ζ), that represent the position within the element. The global coordinates of the nodes (x_j, y_j, z_j) give the position within the global geometry and if the transformation between the global coordinates and the local coordinates is done with the same basis functions, the elements are so called isoparametric elements [35]. With this kind of representation, any element in the global coordinate system can be transformed into a regularly shaped element in the local coordinate system:

$$x = \sum_{j=1}^{n_n} x_j N_j(\xi, \eta, \zeta) \qquad y = \sum_{j=1}^{n_n} y_j N_j(\xi, \eta, \zeta) \qquad z = \sum_{j=1}^{n_n} z_j N_j(\xi, \eta, \zeta) \tag{4.2}$$

where n_n represents the number of nodes in the element and N_j are the used shape functions that depend on the number of nodes.

If vector quantities like vector potentials are considered, it is an advantage to approximate them with the aid of edge base functions since the nodal representation imposes full continuity of the vector field in tangential and normal direction which can lead to non-physical solutions [11]. Using edge based elements ensures the continuity of the tangential component and allows the normal component to be discontinuous. The edge basis functions are vectorial and satisfy

$$\int_{edge_i} \mathbf{N_j} \cdot d\mathbf{r} = \begin{cases} 1 & \text{if } i = j \\ 0 & \text{otherwise.} \end{cases} \tag{4.3}$$

Applying (4.1) and (4.3) leads to sparse system matrices and the resulting linear equation system can be solved with direct or iterative procedures.

4.2 Cable shield model with EleFAnT3D

After this short introduction of the used software package, the following sections give a description of how the fundamental geometry settings and the shield geometry was implemented.

4.2.1 Basic geometry

The initial rectangular grid and the basic geometry is shown in Fig. 4.2, whereas the rectangular grid elements are the macro elements which are divided into finite elements as mentioned in section 4.1.

front view: x-z plane   top view: x-y plane
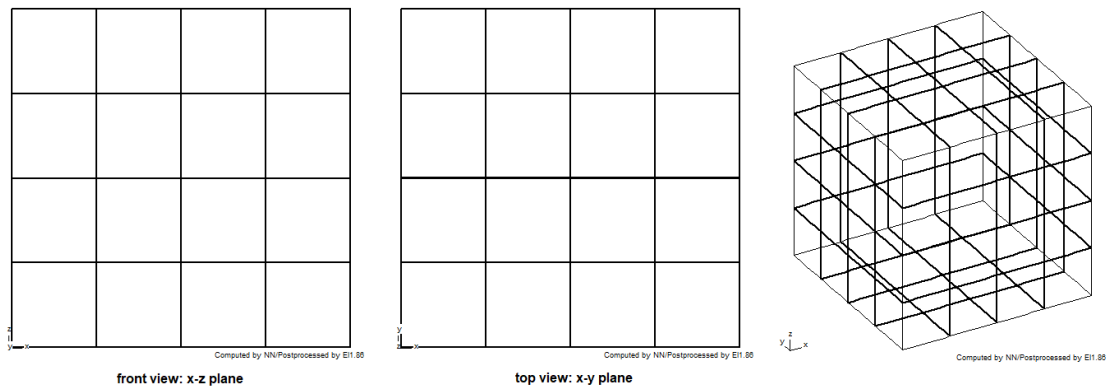
Fig. 4.2: Initial grid for 4x4 macro elements

The possibility to use so called "ellipses with stripes" is already implemented and this special ellipsoid geometry is needed since the basic ellipsoid would eliminate macro elements that are later needed to model the complex shield geometry. A comparison of these two variants is shown in Fig. 4.3.
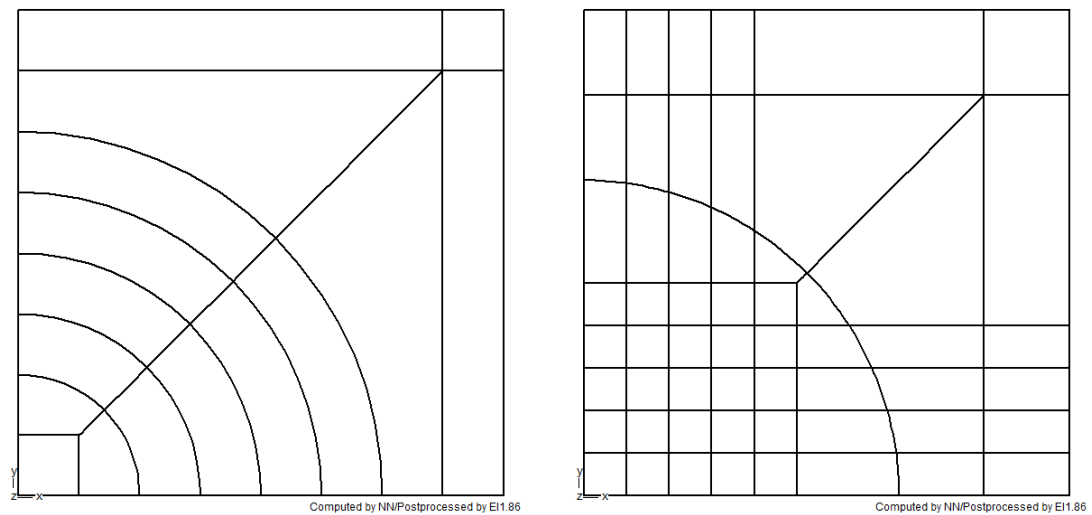
Fig. 4.3: Predefined variants for ellipses, on the right is the used geometry implementation providing macro elements for the shield geometry

The basic cable geometry consisting of the inner conductor and the cable shield is shown in in Fig. 4.4.

- 48 -
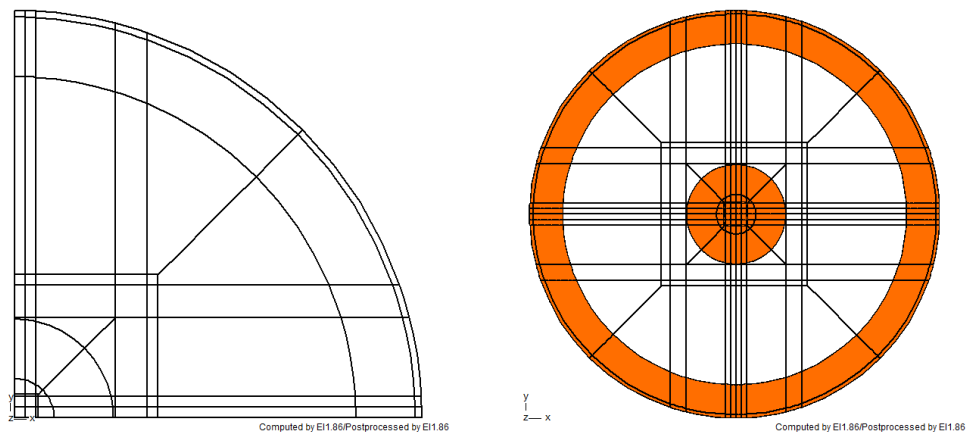
Fig. 4.4: Top view of quarter model and full cable model for solid shield

The implemented shield consists of two macro-elements in the x-y plane where the middle radius varies with the frequency due to skin effect. This frequency dependent behaviour is also applied to the model of the inner conductor, in case a termination resistance is needed for application purposes.

4.2.2 Shield geometry

As mentioned before, for the cable model, the implemented ellipsoids with stripes as depicted in Fig. 4.3 are used to achieve a sufficient number of macro-elements to model the rhomboid shaped apertures for the cable shield.

There are two main models, one for a coverage factor of 75% and higher and one for a coverage factor below 75%. The modelling of the apertures especially modifying the z - layers for these two cases is explained later on.

First, the joint base-manipulations are explained.

Due to the use of the ellipsoids, some macro-elements are eliminated and cannot be manipulated, as shown in Fig. 4.5, and this needs to be considered for later geometry calculations since these eliminated elements determine the minimal possible coverage factor and the limitation of the basic geometry.
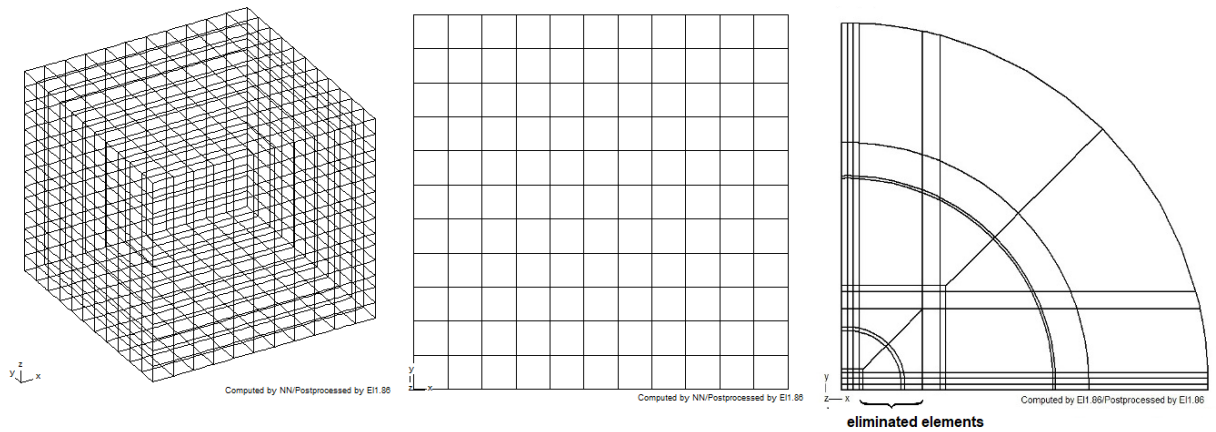
Fig. 4.5: Basic geometry indicating eliminated macro elements

Nevertheless, the implemented model can vary the coverage factor from 60% to 100% and also the weave angle can be arbitrarily set up to 179 degrees. These very extreme variations are more for evaluation purposes or for the investigation of pinched, stretched or bent cables since a common coaxial cable usually has a coverage factor between 95% and 98% and a weave angle of around 30 degrees.

To achieve the desired geometry, the elements considered for the conductive material and the elements for the apertures are chosen from the beginning and remain the same for any parameter-variation of the implemented shield geometry.

Material parameters can be set directly and the parameterization of the main geometry can be done by modifying the x- and y-distances of the main grid.

For the apertures, geometry parameters like the radius of the shield and shield thickness together with the coverage factor or optical coverage factor (cf) and the weave angle α are needed. This data usually can be taken from datasheets and the weave angle can be measured. A model with a coverage factor of 98% is shown in Fig. 4.6.
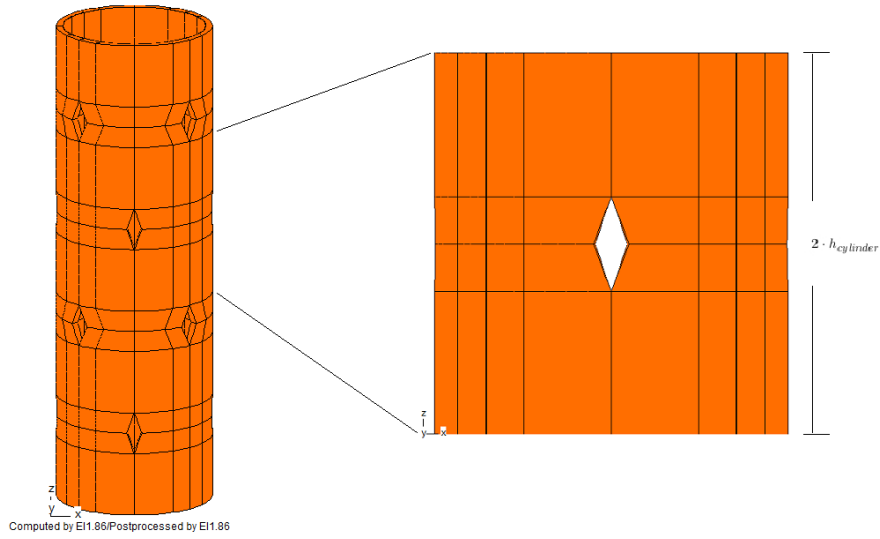
Fig. 4.6: Sample cable model for coverage factor of 98%

For the aperture size, a so called shielding-factor (sf) is introduced. This factor describes the ratio of the shield-material versus the aperture opening in the $x - y$ plane.

The used procedure herein is:

The area of a certain cylinder based on the outer shield circumference (u_{outer}) and the angle β as depicted in Fig. 4.7, where β is the complementary angle of half of the weave angle α, is derived as

$$\beta = 90^{\circ} - \frac{\alpha}{2}. \tag{4.4}$$

To calculate the aperture area, the area of the solid cylinder jacket is multiplied with the coverage factor and subtracted from the full area

$$A_{apertures} = 2 \cdot u_{outer} h_{cylinder} \left(1 - cf\right) \tag{4.5}$$

giving the area of all apertures on the cylinder jacket. To derive the area of one single aperture, the area has to be divided by four as in Fig. 4.7.
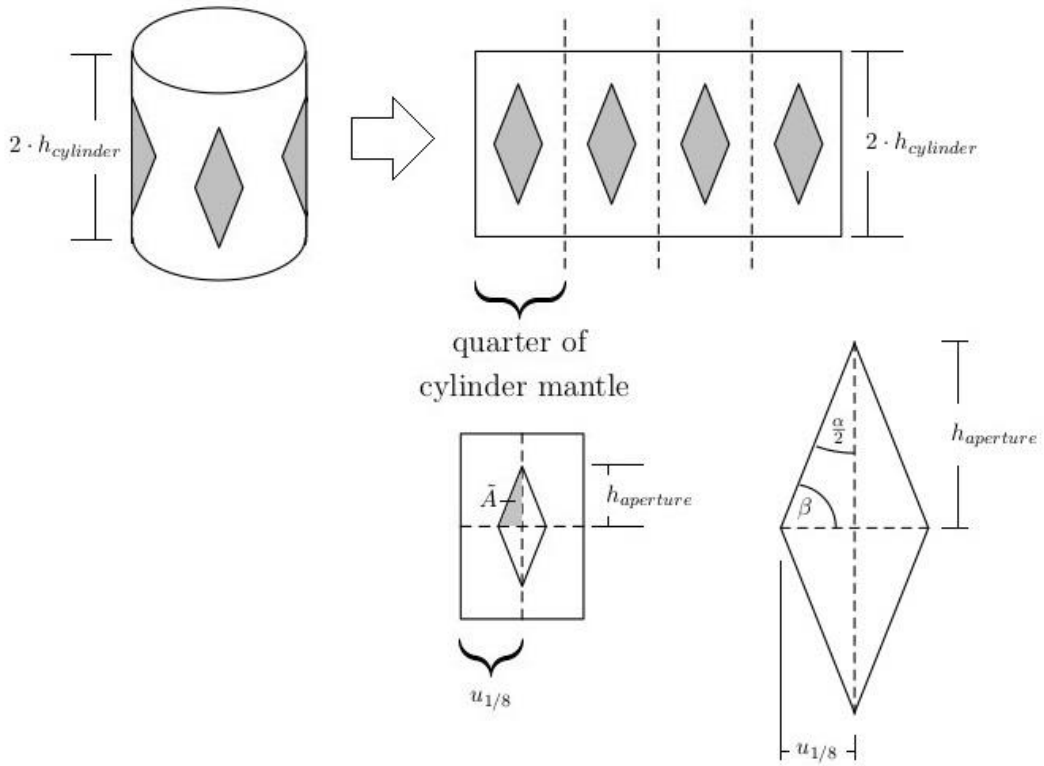
Fig. 4.7: Derivation of the shielding-factor for a given optical coverage

Since for the FEM-model the coordinates are calculated for an eighth of the cable circumference, this leads to the working area $\tilde{A}$ as in Fig. 4.7

$$\tilde{A} = \frac{A_{apertures}}{16} = \frac{u_{1/8} \cdot (1-sf) \cdot h_{aperture}}{2} = \frac{u_{1/8}^2 \cdot (1-sf)^2 \cdot \tan \beta}{2} \tag{4.6}$$

where $u_{1/8}$ is one eight of the outer shield circumference.

The shielding-factor then can be derived as

$$sf = 1 - \sqrt{\frac{2 \cdot \tilde{A}}{u_{1/8}^2 \cdot \tan \beta}}. \tag{4.7}$$

This shielding-factor is a constant parameter for one given geometry-model and the shielding material component is calculated as:

$$s_{mat_n} = r_n \cdot sin\left(\frac{u_{n/8} \cdot sf}{2 \cdot r_n}\right) \tag{4.8}$$

and the non-material regions are calculated as

$$s_{void_n} = r_n \cdot sin\left(\frac{u_{n/8} \cdot (1-cf)}{2 \cdot r_n}\right) \qquad (4.9)$$

where r_n and $u_{n/8}$ denote the n radii and circumferences of the macro-elements the shield is modelled as depicted in Fig. 4.8.
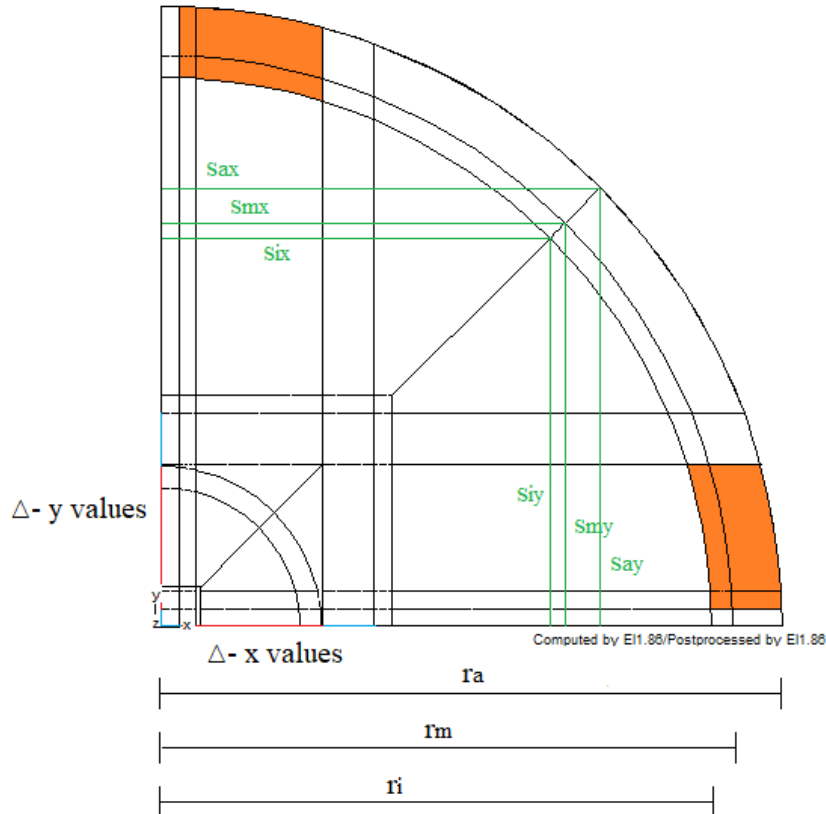
Fig. 4.8: Quarter model of cable shield indicating the material- and non-material regions of the shield

In Fig. 4.8, the total range of the material- and non-material parts from (4.8) and (4.9) are indicated as s_{nx} and s_{ny} in green and the Δx -and Δy - values of the macro elements for modifying the regions with shielding material along the y - and the x - axis, respectively, are depicted in red and for modifying the regions without shielding material are depicted in blue. The macro- elements of the shield for modelling the braid are coloured in orange and the elements for modelling the holes are white.

Fig. 4.9 shows the order of how to modify the x - intervals on the y - axis and vice versa, depending on which octant is modified.
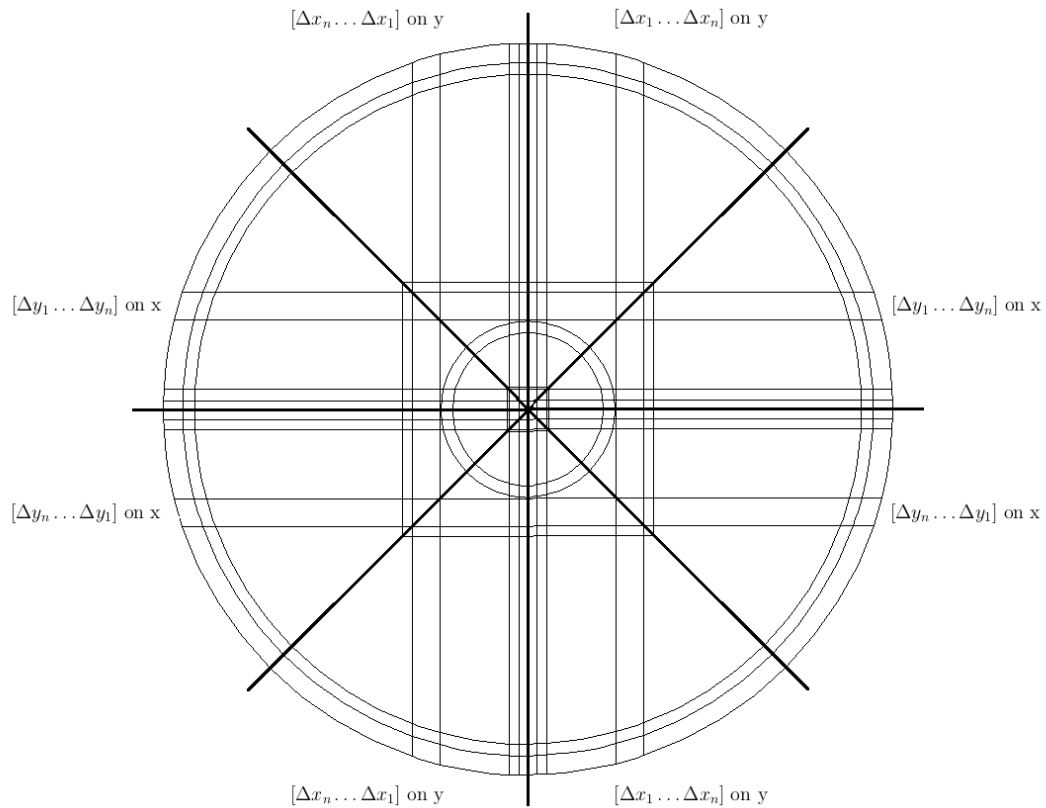
Fig. 4.9: Manipulation in the x-y plane

Now the elements on consecutive z - planes can be modified with respect to these values and the aforementioned eliminated macro-elements have to be considered carefully to avoid any intersections between single elements or too heavy geometry distortions. This z - layer manipulation is now divided into the two main geometry models.

4.2.3 Modelling the coverage factor of the shield

In the previous section, the manipulations in the x - y plane have been explained. To implement a desired coverage factor, these manipulations have been done on consecutive z -layers to obtain the final geometry. The implementation is divided into two different models, one to implement coverage factors of 75% and higher and one to implement coverage factors below 75% . The difference between these two models is explained in the following subsections.

4.2.3.1 Coverage factor of 75% and higher

In this case, three different z-layers have to be modified and consecutively repeated to model the braided pattern as shown in Fig. 4.10.
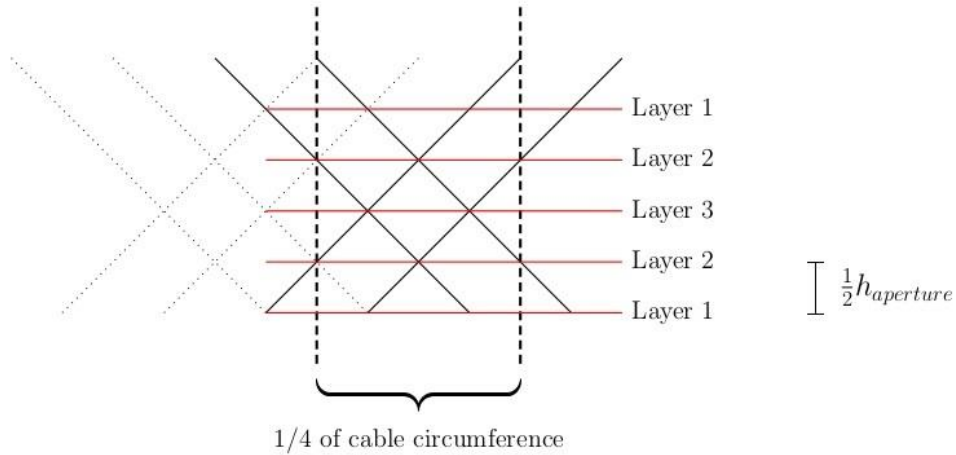
Fig. 4.10: Different layers for cable model with coverage factor of 75% and higher

For the geometry variations with a given coverage factor of 75% and higher, the first and the third z-layer have half of the material thickness, as it is depicted in Fig. 4.10 as well.

Layer 1 and Layer 3 always have half of the material thickness ($sf / 2$) so a constant shield-material coverage can be achieved which is due to the assembly of the braid pattern. The height of the z-layers as depicted in Fig. 4.10 are calculated as

$$\frac{1}{2}h_{aperture} = z = \frac{u_{outer}}{8} \cdot (1 - cf) \cdot tan(\beta) \tag{4.10}$$

In this case, the absolute height of one element ($h_{cylinder}$) with respect to the shield radius and weave angle, as shown in Fig. 4.6, is not kept constant. With this approach, it is possible to model cable deformations such as compressed or stretched cables as depicted in Fig. 4.11.
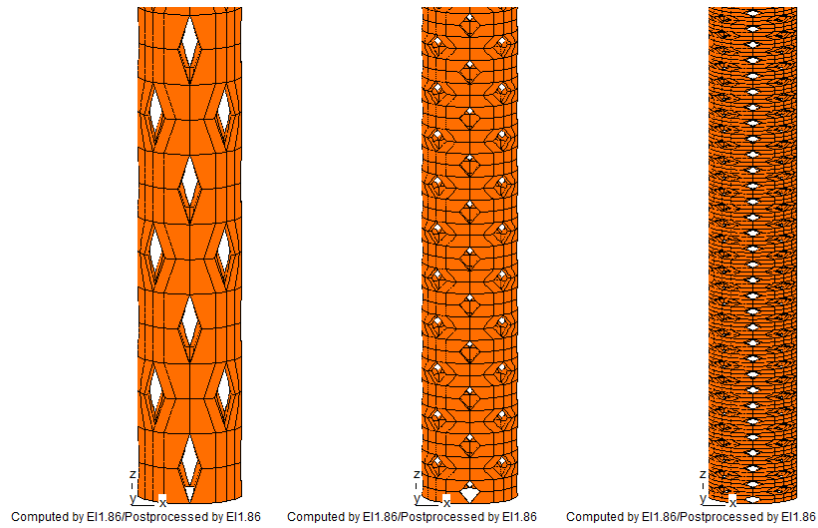
Fig. 4.11: Example for possible cable variations by changing the coverage factor by altering the size of the apertures

Adding an additional z-layer after the second allows to change the coverage factor not only by the size of the apertures by changing the shield factor but by varying the number of apertures per length, as it is depicted in Fig. 4.6 and Fig. 4.12.
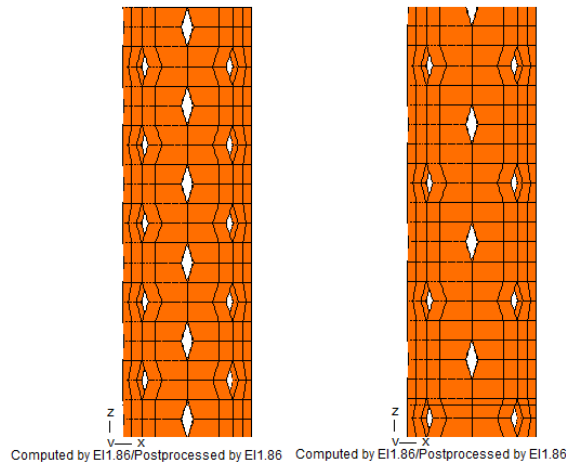
Fig. 4.12: Example for possible cable variations by changing the coverage factor by the number of apertures per length

4.2.3.2 Coverage factor less than 75%

An example for coverage factors of less than 75% is shown in Fig. 4.13. In this case four different z-layers have to be taken into account
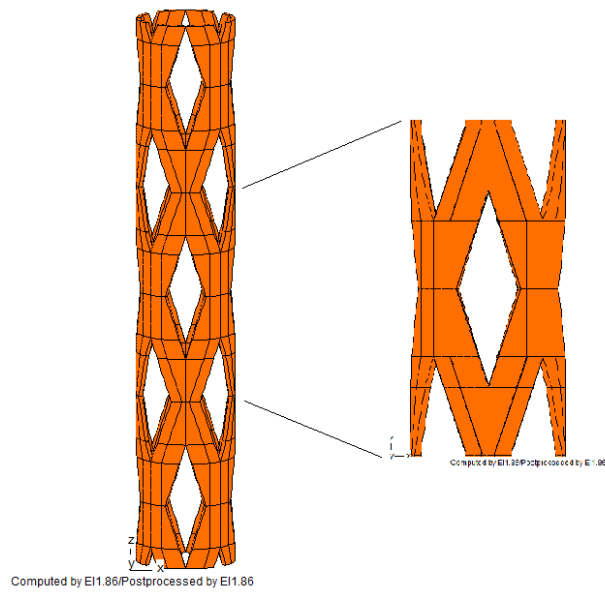
Fig. 4.13: Shield model with coverage factor of 60%

Again, Layer 1 and Layer 4 have half of the material thickness which is again due to the assembly of the braid pattern to achieve a constant shielding material thickness as depicted in Fig. 4.14.

Layer 1
Layer 2

Layer 3
Layer 4
Layer 3

Layer 2
Layer 1

1/4 of cable circumference
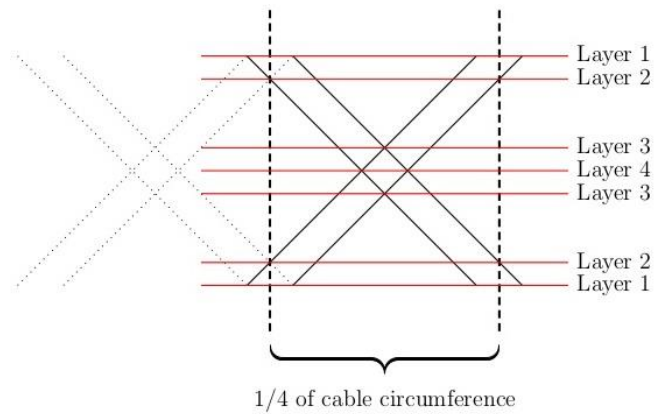
Fig. 4.14: Different layers for cable model with coverage factor less than 75%

The height of the z-layers to get the correct rhomboid shape is depicted in Fig. 4.15 and the calculation of the heights is done as:

$$\frac{1}{2}h_{aperture} = z_1 + z_2 = \frac{u_{outer}}{8} \cdot (1 - cf \cdot 0.5) \cdot tan(\beta)$$

$$z_1 = \frac{u_{outer}}{8} \cdot (cf \cdot 0.5) \cdot tan(\beta) \tag{4.11}$$

$$z_2 = \frac{1}{2}h_{aperture} - z_1$$
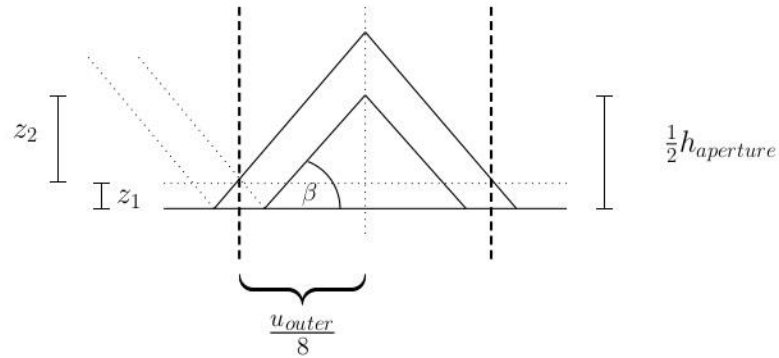
Fig. 4.15: Calculation of height of z-layers

Again, varying coverage factors and cable deformations can be modelled with this version as well and some examples for this shield geometry model are depicted in Fig. 4.16.
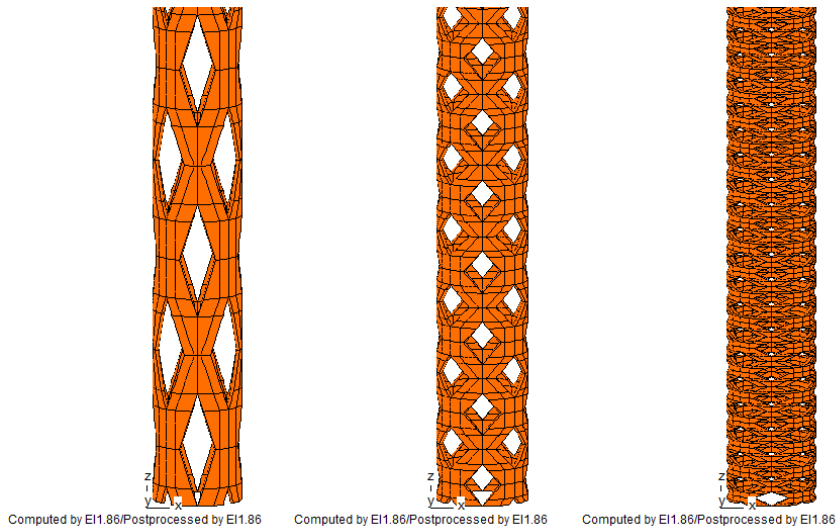
Fig. 4.16: Examples for possible cable variations

5   Measurement technique

This chapter describes a new and reliable measurement method for the transfer imped-
ance with the help of a 2-port network analyser that is fast and very simple to imple-
ment. This method was first presented in [8] and [9].

Known techniques to measure the transfer impedance are usually very costly and time
consuming because of the complex measurement setup [35].

Nevertheless, it is noteworthy that this method developed by us is not a standardized
one but it can be easily applied for quality control of given coaxial cables or for investi-
gation of cable behaviour after exposing the cable under test to mechanical or thermal
stress since frequent measurements can be done rather quickly.

5.1   Measurement setup

The needed parameters to derive the transfer impedance are the scattering-parameters
(s-parameters) S_{11} and S_{21} as they are depicted in Fig. 5.1 and, therefore, the measure-
ment is done with a 2-port network analyser and the transfer impedance Z_t is then eval-
uated as

$$Z_t = \frac{1}{I_{shield}} U' \quad \Omega / m \qquad (5.1)$$

where I_{shield} denotes the current through the shield and U' describes the voltage drop
along the outer side of the shield as described in section 3.3.

The two ports Port 1 and Port 2 of the network analyser are denoted as $P1$ and $P2$,
respectively in Fig. 5.1 and Z_0 represent the input and output impedance. With the aid
of a so called adapter, as shown in Fig. 5.2 on the right, where the inner conductor is
basically soldered to the shield, the shield of the cable under test is connected to the
inner conductor without being connected to the ground terminal of Port 1 of the network
analyser.
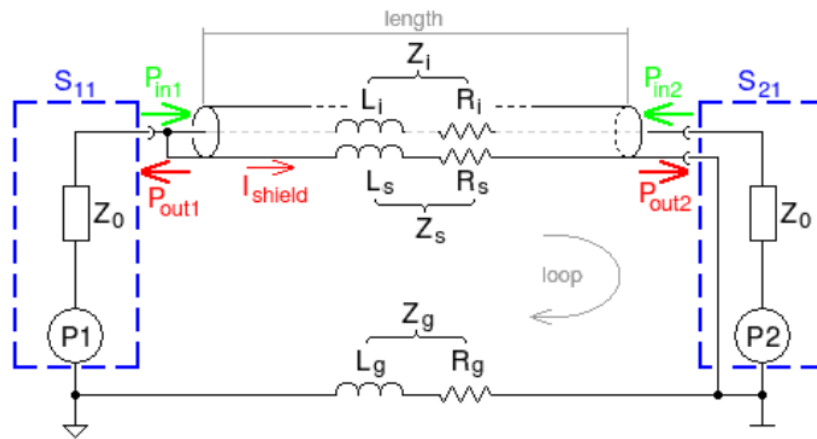
Fig. 5.1: Model circuit [8], © 2017 IEEE

The parameters R_i and L_i model the inner conductor and the parameters R_s and L_s are used to model the shield of the cable. The ground terminals of the two ports of the network analyser cannot be referenced to the same ground potential and therefore R_g and L_g stand here for the internal ground link. Additionally, different ground symbols were used to distinguish the two different ground potentials of the ports, which can be reasoned by the physical design of the network analyser.
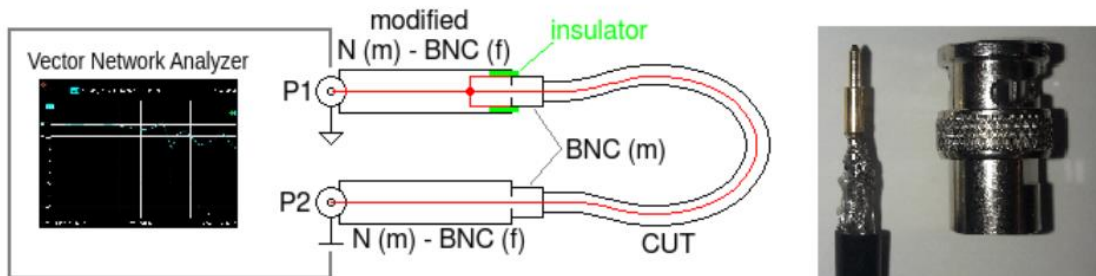
Fig. 5.2: Test setup [8], © 2017 IEEE

The representation of the setup as lumped elements is again valid as long as the length is considered to be electrically short and the rule of the maximum length $\mathcal{L} < \dfrac{\lambda}{10}$ is fulfilled as discussed in Section 2.4.

Since exported measured values are given in logarithmic format, the s-parameters have to be converted to linear scale

$$S_{xlin} = 10^{\frac{S_x(dB)}{20}} \tag{5.2}$$

where S_x denotes the magnitudes of the parameters S_{11} and S_{21}.

5.2 Parameter evaluation

The aforementioned setup describes a passive two-port network with a system imped-ance Z_0 of 50Ω on both Port 1 and Port 2. Port 1 leads into a low impedance path of the shield consisting of R_s and L_s and the ground impedance R_g and L_g to get a closed loop. The inner conductor with the impedance R_i and L_i of the unmodified end of the cable under test is terminated at Port 2 of the network analyser by the impedance Z_0. Since it is assumed that the characteristic impedance of 50Ω is several orders of magnitude greater than the shield impedance and the ground impedance $(Z_0 \gg Z_s + Z_g)$, the output current of Port 1 will take the current path denoted as "loop" in Fig. 5.1. The needed reflection coefficient S_{11} is defined as the ratio between the voltage out of Port 1 and the reflected voltage at Port 1 and is given as

$$S_{11} = \frac{u_{out1}}{u_{in1}}. \tag{5.3}$$

The power ratio P_{in1} at Port 1 can be expressed in terms of the S_{11} parameter as

$$P_{in1} = P_{gen} \cdot (1 - |S_{11}|^2) \tag{5.4}$$

where P_{gen} denotes the output power at Port 1 of the network analyser.

The input impedance of Port 1 can be calculated via the S_{11} parameter as well, and it is given as

$$Z_{11} = Z_0 \cdot \frac{1 + S_{11}}{1 - S_{11}} \tag{5.5}$$

and together with (5.3) the shield current I_{shield} can be derived as

$$I_{shield} = \sqrt{\frac{P_{in1}}{Z_{11}}}. \tag{5.6}$$

Having now computed the shield the current I_{shield} for (5.1), the voltage drop along the cable under test has to be evaluated by the use of the reflection coefficient S_{21}.

The power experienced at Port 2 is only a fraction of the transferred power P_{in1} due to the fact that, in this setup, the ground connectors of the ports are separated by the ground impedance R_g and L_g. The voltage at Port 2 can now be evaluated as

$$U_2 = S_{21} \cdot \sqrt{P_{in1} \cdot Z_0} \tag{5.7}$$

and (5.1) leads to

$$Z_t = \frac{1}{I_{shield}} U'_2 \tag{5.8}$$

where U'_2 is the referenced voltage to a unit-length of 1m.

With the measured parameter S_{21} the transfer impedance can now be written as

$$Z_t = Z_0 \cdot S_{21} \cdot \sqrt{\frac{1+S_{11}}{1-S_{11}}} \frac{1}{l} \Omega / m. \tag{5.9}$$

Considering (5.9), it is evident that different kinds of cables under test can be evaluated with this method, since the intrinsic and unknown impedances have no direct influence in the evaluation of the transfer impedance and the only parameters needed are the reflection coefficient S_{11}, the forward gain coefficient S_{21} and the system impedance of the given setup.

An equivalent circuit of the transfer impedance with respect to this given setup is shown in Fig. 5.3.
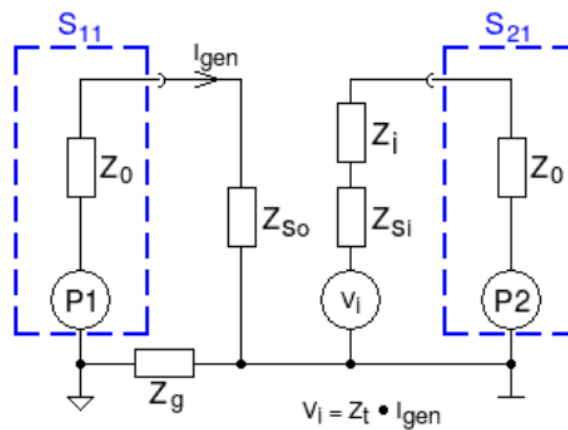
Fig.: 5.3: Equivalent circuit for braided cable shields [8], © 2017 IEEE

The transfer impedance Z_t in this equivalent circuit consists of the impedance Z_i and Z_s, where the shield impedance is split into an inner system (Z_{si}) and an outer system (Z_{So}). It is noteworthy that the system impedance Z_0 is purely resistive, whereas Z_{So}, Z_{Si} and Z_i are complex values.

5.3 Results and comparison with analytical and numerical models

The measurements have been carried out for cables under test of different lengths but of the same cable model. It has also been proven that the cable layout for this measurement setup is not of importance and even having a loop for longer cable length does not influence the measured results. This is shown in Fig. 5.4 for a measured cable under test for 1m of length. The reason for this behaviour is that even if there is a small rise in the impedance Z_s, the current will drop accordingly and this will lead to a relative voltage drop for U_2 at Port 2 and therefore this influence is cancelled out.

The same stability was seen when a metallic plate was put under the cable under test. However, this condition does not hold in case of propagation effects as for example when resonances occur.
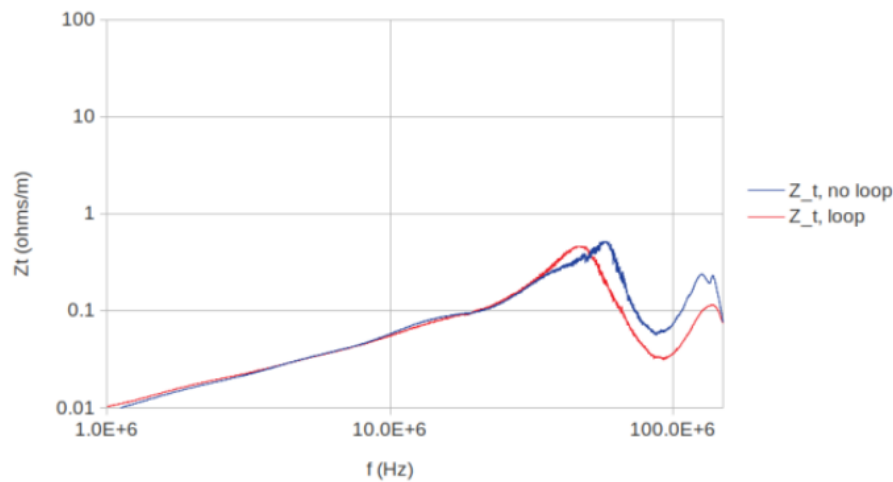
Fig. 5.4: Influence on loops in the setup on transfer impedance [8], © 2017 IEEE

Fig. 5.5 depicts the comparison between the measured results and the numerical and analytical model for the transfer impedance. The cable under test in this case was the standard RG-58 coaxial cable with a characteristic impedance of 50Ω.
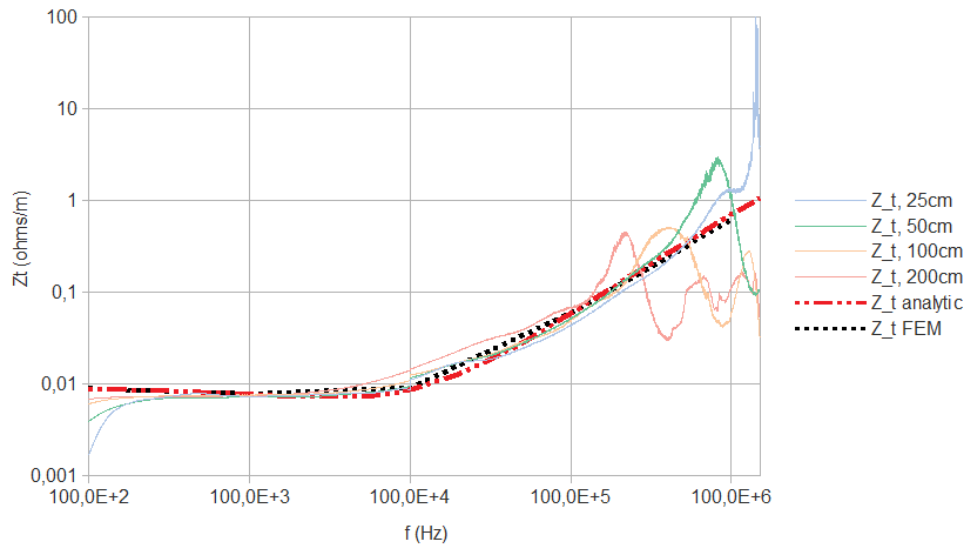
Fig. 5.5: Comparison of measured and simulated data [8], © 2017 IEEE

The results stand in very good agreement and this comparison was also used to validate the numerical and analytical models discussed in the previous sections.

6   Parameter dependencies for transfer impedance

The aim of this chapter is to give a short overview of the influence of parameter variations on the transfer impedance, geometry- as well as material-related. At first the investigation includes the influence of the shield thickness and the used material to cover the basic shield variations. The second part covers the geometry variants of the braided shield affecting the aperture geometry including influential parameters as coverage factor and weave angle, altering the size of the area of a given aperture and the last part is a combination of these variations to demonstrate the overall influence.

The basic analysis in sections 6.1-6.3 has been done with the FEM-model described in chapter 4. Since the numerical and analytical results always stood in very good agreement, a more detailed parameter analysis using sensitivity analysis with the aid of the analytical model has been carried out in section 6.4 to save computational time.

6.1   Basic shield parameters

Fig. 6.1 demonstrates the influence of the shield thickness on the low frequency range determining the DC- resistance value and the skin effect losses for increasing frequencies in case of a solid shield.

The most dominant effect at first sight is the influence of the shield thickness on the DC-resistance, since the DC-resistance is directly influenced by the current carrying cross-section of the conductor which is determined for low frequencies by the shield thickness:

$$R_{dc} = \frac{1}{\pi\sigma(b+a)(b-a)} \tag{6.1}$$

where a denotes the inner radius of the shield, b the outer radius and σ is the conductivity of the shielding material as it is mentioned in section 3.4.

Not only the value of the DC-resistance is affected by the shield thickness, but also the beginning of the region defining the skin effect losses, as seen in Fig. 6.2. To make this effect clearer, the curves are normalized with respect to the DC-resistance value.

The corner frequency at which the decrease of the transfer impedance of the solid shield starts can be coarsely approximated as the frequency when the skin depth δ equals the shield thickness d, i.e.

$$f_c = \frac{1}{d^2 \cdot \mu_0 \cdot \sigma \cdot \pi} \tag{6.2}$$

where σ again is the conductivity of the shield and μ_0 denotes the permeability of free space.
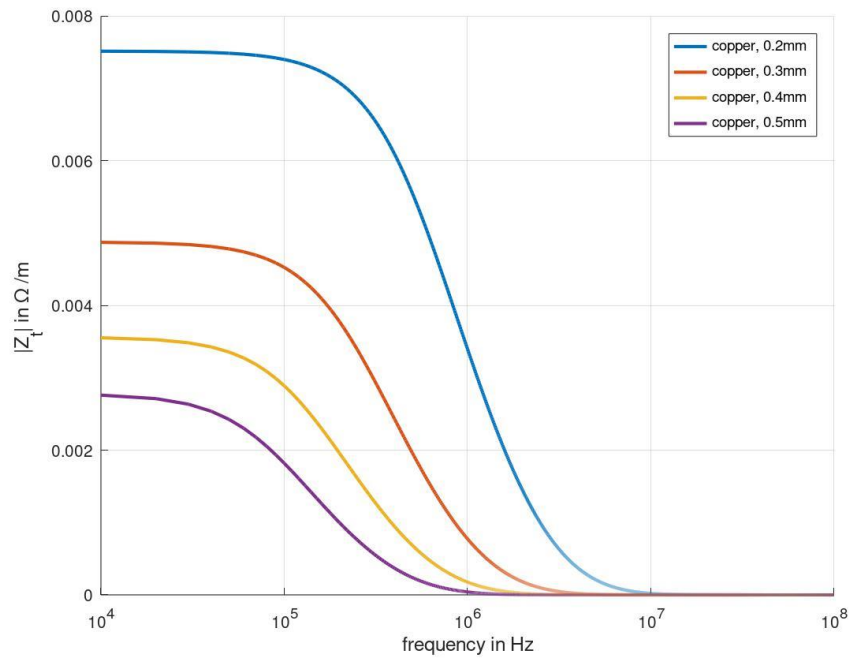
Fig. 6.1: Influence of shield thickness and frequency behaviour
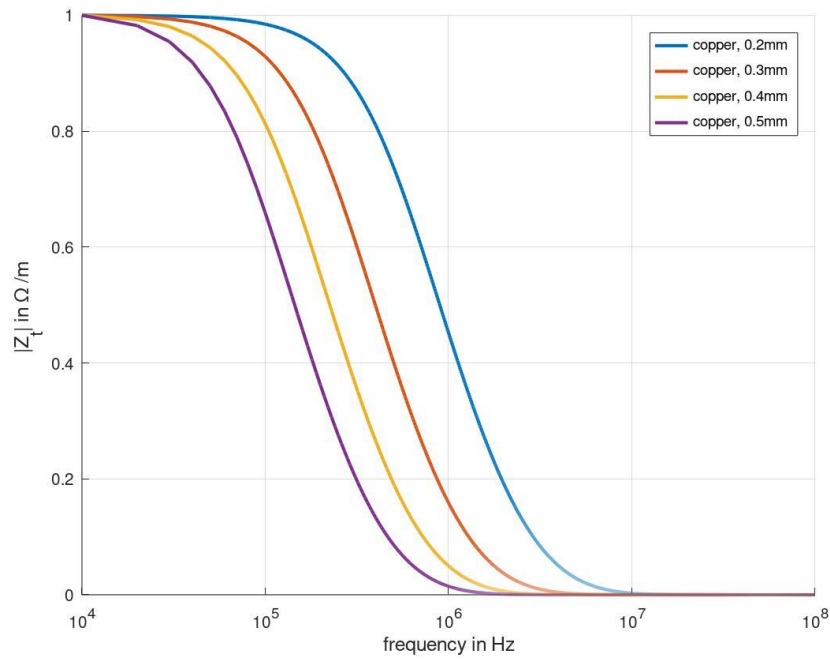
Fig. 6.2: Influence of shield thickness and frequency behaviour normalized by R_{dc}

Therefore, a thicker shield in general translates into a better shielding effectiveness at lower frequencies.

Looking at (6.1) and (6.2), it also clear that the conductivity σ of the shield material has an impact on the DC-resistance and the frequency dependent skin effect losses as well. For this evaluation, the used conductivities are copper ($\sigma = 5,8 \cdot 10^7$ (Ωm)$^{-1}$), gold ($\sigma = 4,5 \cdot 10^7$ (Ωm)$^{-1}$) and aluminium ($\sigma = 3,7 \cdot 10^7$ (Ωm)$^{-1}$).

Fig. 6.3 compares the transfer impedance of a solid shield with a given shield thickness of 0.2mm with respect to different materials. Here the DC- resistance alterations are clearly visible. Fig. 6.4 again depicts the normalized curves to represent the frequency dependence of the skin effect losses and the aforementioned frequency f_c more clearly.
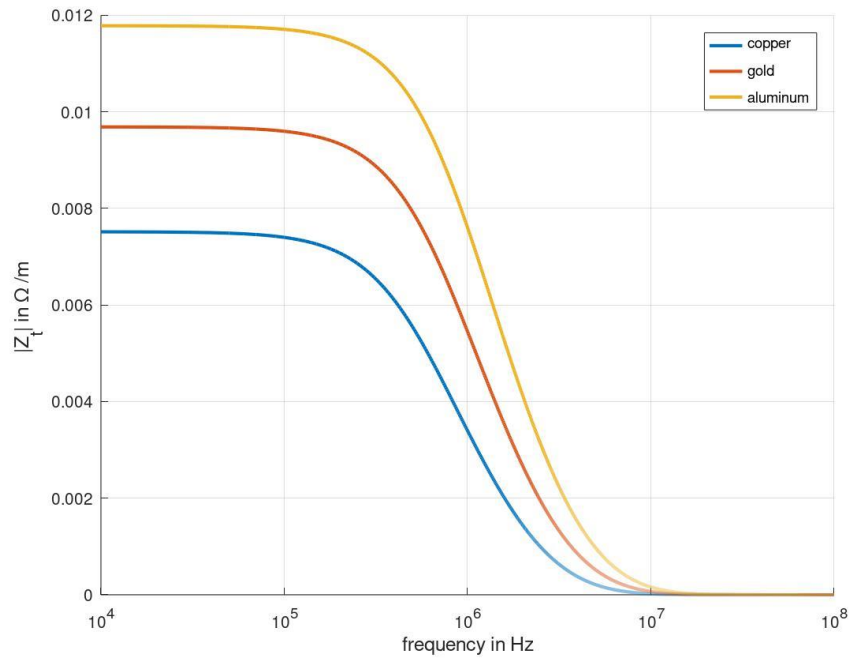
Fig. 6.3: Transfer impedance for different shield conductivities
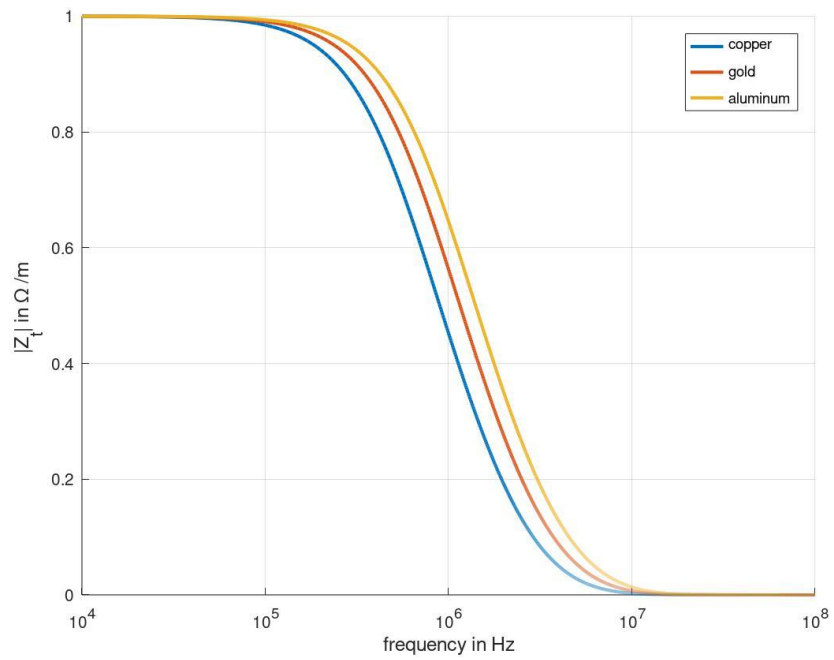
Fig. 6.4: Transfer impedance for different shield conductivities normalized to R_{dc}

6.2 Coverage factor and weave angle

This section gives a short overview on the influence of the geometry variations regarding the optical coverage factor of a cable shield and different shapes of the rhombic apertures.

Fig. 6.5 depicts the graph of the transfer impedance of a cable shield with a constant thickness of 0.2mm and a given weave angle of 30 degrees but with varying coverage factors, changing the size of the apertures without altering the shape. A higher coverage factor translates into less or smaller apertures and this leads to a smaller hole-inductance resulting in a better shielding effectiveness. It is also noteworthy that the coverage factor has an influence on the DC-resistance value too, since a decreasing coverage factor leads to a decreasing effective conductor area which translates into a higher resistance value as seen in (3.34).
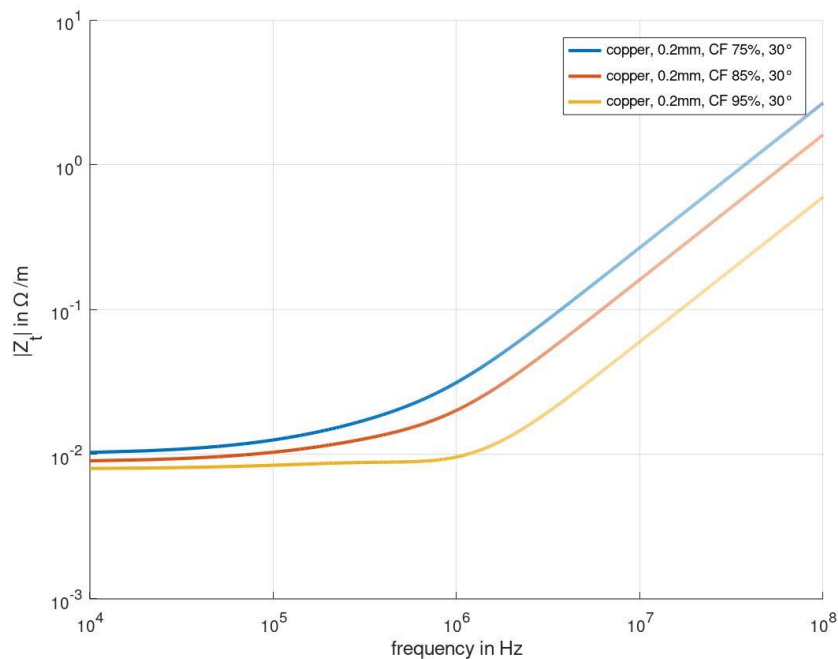
Fig. 6.5: Influence of coverage factor on transfer impedance

Fig. 6.6 shows the transfer impedance for a constant coverage factor of 95% but for varying weave angles comparable to stretching or compressing a cable with a length of one meter. In this scenario, the transfer impedance remains more or less the same. The explanation for this behaviour is that the height of one single aperture varies with respect to the changing angle. In case of a smaller weave angle, the height of every single aperture is elongated which leads to a higher inductance value but is also leads to fewer

apertures per meter of a given cable and the two effects seem to keep balance. The same is valid for increasing weave angles, since the height of one aperture is compressed, decreasing the inductance of one single aperture but increasing the number of apertures per meter. It has to be mentioned that, in this case, the reference length of the cable is of importance, since it is crucial whether the inductance changes based on the deformities are eliminated or not.
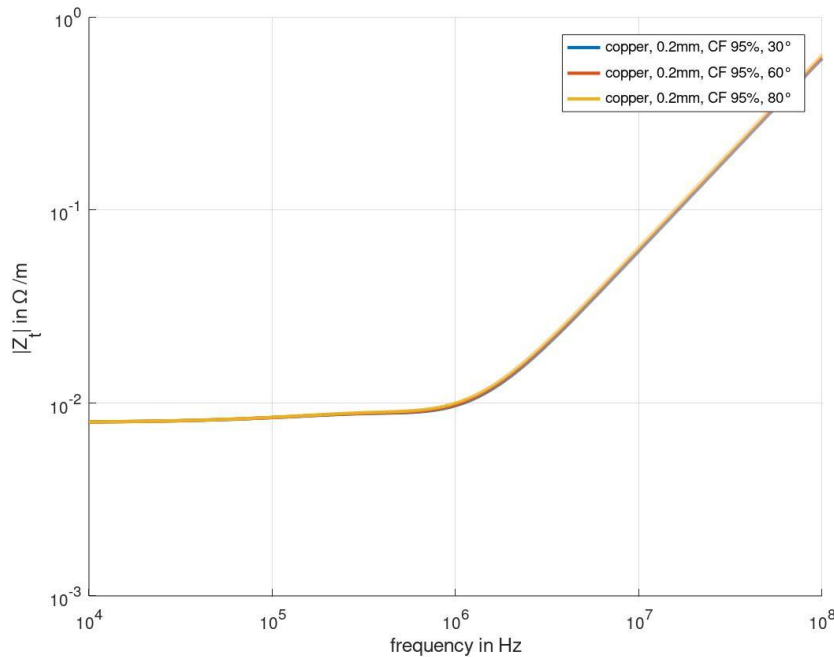
Fig. 6.6: Influence of different aperture shapes with constant reference cable-length

6.3 Overall influence

After the basic alterations have been discussed, a variation of all parameters is briefly demonstrated here. Fig. 6.7 shows the transfer impedance for constant coverage factor and weave angle but with different shield thicknesses. As already mentioned, the influence on the DC-resistance and the frequency curve in the lower frequency spectrum is visible but, also in the higher frequency range, a difference is noticeable. Indeed, a shift of the curve with respect to the frequency can be seen here. It is clearly visible that, for evaluation and modelling of the transfer impedance, the shield thickness is a highly important parameter and deviations in its dimensions lead to a substantial change.

Another factor is the influence of the number of apertures due to a given layout, as depicted in Fig. 6.8.

Fig. 6.9 contrasts the impedance curves of these two model variants and shows the influence of a given cable layout with apertures of the same size and shape but different numbers per meter. Reducing the number of holes in the shield is another way to increase the coverage factor.
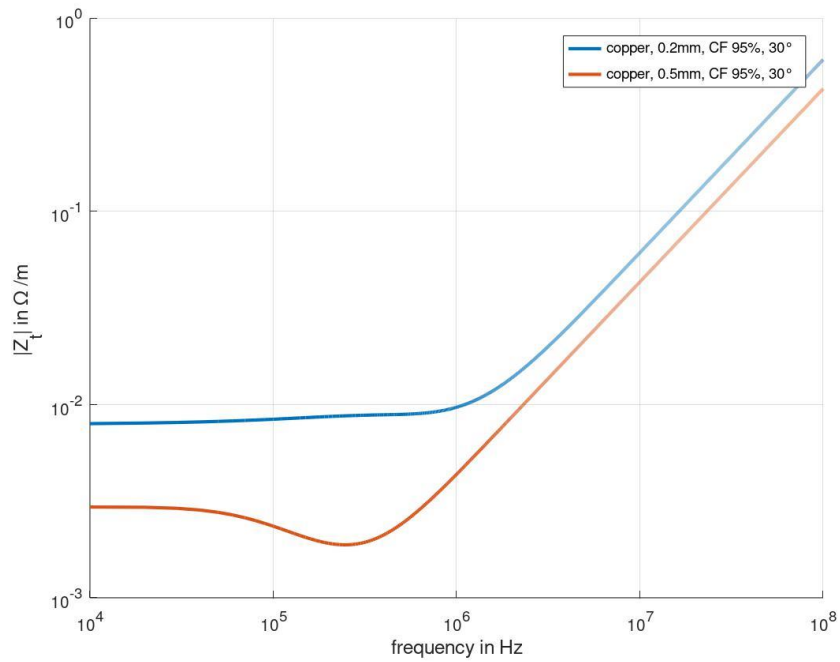
Fig. 6.7: Comparison of different shield thicknesses on overall behaviour
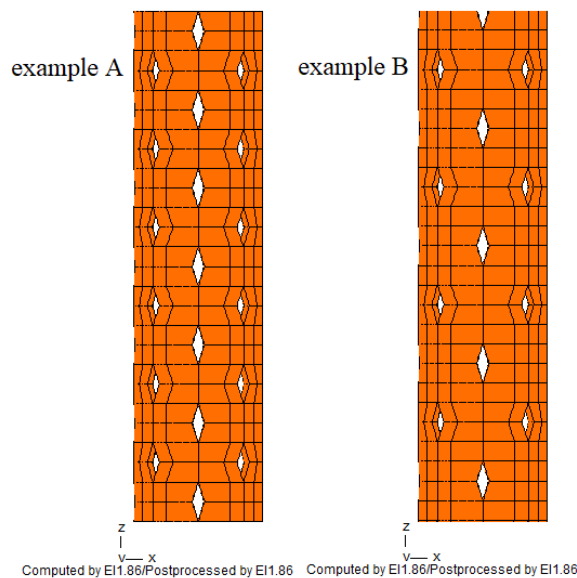
Fig. 6.8: Different layout versions determining the number of apertures per length
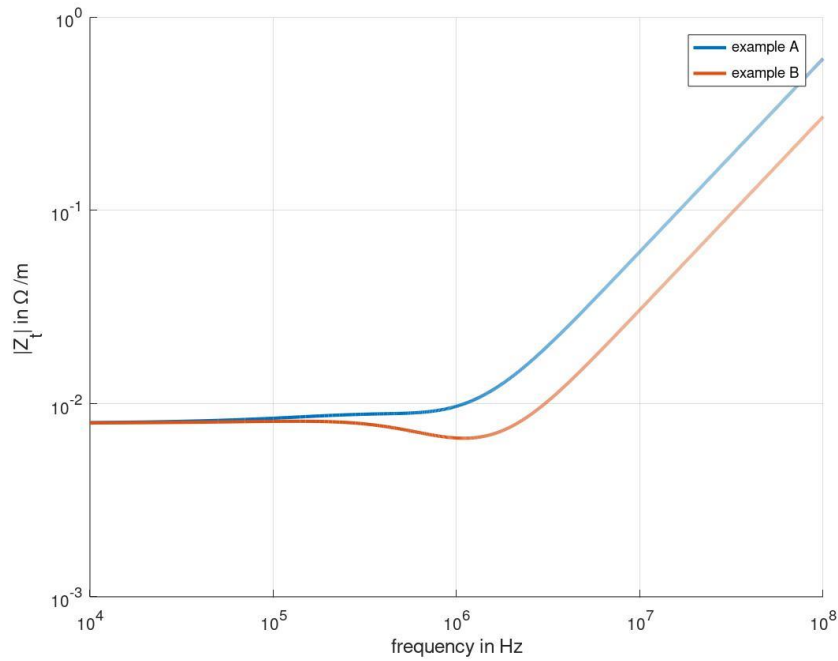
Fig. 6.9: Influence on number of apertures per constant cable length for varying the coverage factor based on the number of apertures per meter

6.4 Sensitivity analysis

In the previous sections, different parameter influences have been studied briefly. To get a structured overview of those influences, input parameter variations have been investigated by the aid of sensitivity analysis.

The aim of sensitivity analysis in general is to evaluate the influence of variable input parameters on the variance of a given model output. The relevant investigation is considered to be a Global Sensitivity Analysis (GSA) if all input parameters are varied at the same time and the sensitivity is assessed over the total range of each input parameter. Also, the interaction of the given input parameters is evaluated.

The goal of the Global Sensitivity Analysis, also called Sobol method based on Sobol indices [37], here in this work, is to determine the significance of the influence of different material and geometry parameter variations on the transfer impedance and therefore on the quality of a braided cable shield.

The model considered for this analysis is given as

$$y = f(\mathbf{x}_1 \ldots x_n) \tag{6.3}$$

where y denotes the output (in our case the transfer impedance) and the variables $x_1 \ldots x_n$ are the independent input parameters.

The information whether a random input variable x_i is influential on the investigated output or not is given by the first Sobol index. It gives the contribution of the random variable x_i to the change of the model output without taking interactions with other input variables into consideration.

The input variable is considered to be influential if the conditional variance $V(E[y/x_i])$ is large compared to the variance of the quantity of interest $V(y)$ and therefore the first Sobol index is defined as:

$$S_i = \frac{V_i}{V(y)} = \frac{V(E[y \mid x_i])}{V(y)} \tag{6.4}$$

where $E[y/x_i]$ is the expected value of the model output y with a fixed parameter x_i.

To gather information regarding the sensitivity of first order effects and regarding the interaction between one input parameter and all the other parameters, the total Sobol index or total-order sensitivity index is evaluated as

$$S_{Ti} = 1 - \frac{V(E[y \mid \mathbf{x}_{\sim i}])}{V(y)}. \tag{6.5}$$

where $\mathbf{x}_{\sim i}$ denotes all variable input parameters except x_i.

The second Sobol index gives the influence on the output by the interaction of input parameters x_i and x_j and it is defined as:

$$S_{ij} = \frac{V_{ij}}{V(Y)} = \frac{V(E(Y \mid x_i, x_j)) - V(E(Y \mid x_i)) - V(E(Y \mid x_j))}{V(Y)}. \tag{6.6}$$

For the investigation of the transfer impedance only first-order, total-order and second-order indices defined in (6.4)-(6.6) have been evaluated.

6.4.1 Sensitivity analysis for transfer impedance

The investigated parameters for this analysis are:

Variable		**Input Parameter**
x_1	…	shield thickness
x_2	…	coverage factor
x_3	…	conductivity of the shield
x_4	…	inner radius of the shield
x_5	…	weave angle
x_6	…	number of apertures per meter

The sensitivity analysis has been carried out for different frequency points at 10kHz, 100kHz, 1MHz, 10MHz and 100MHz. The results are depicted in Fig. 6.10.
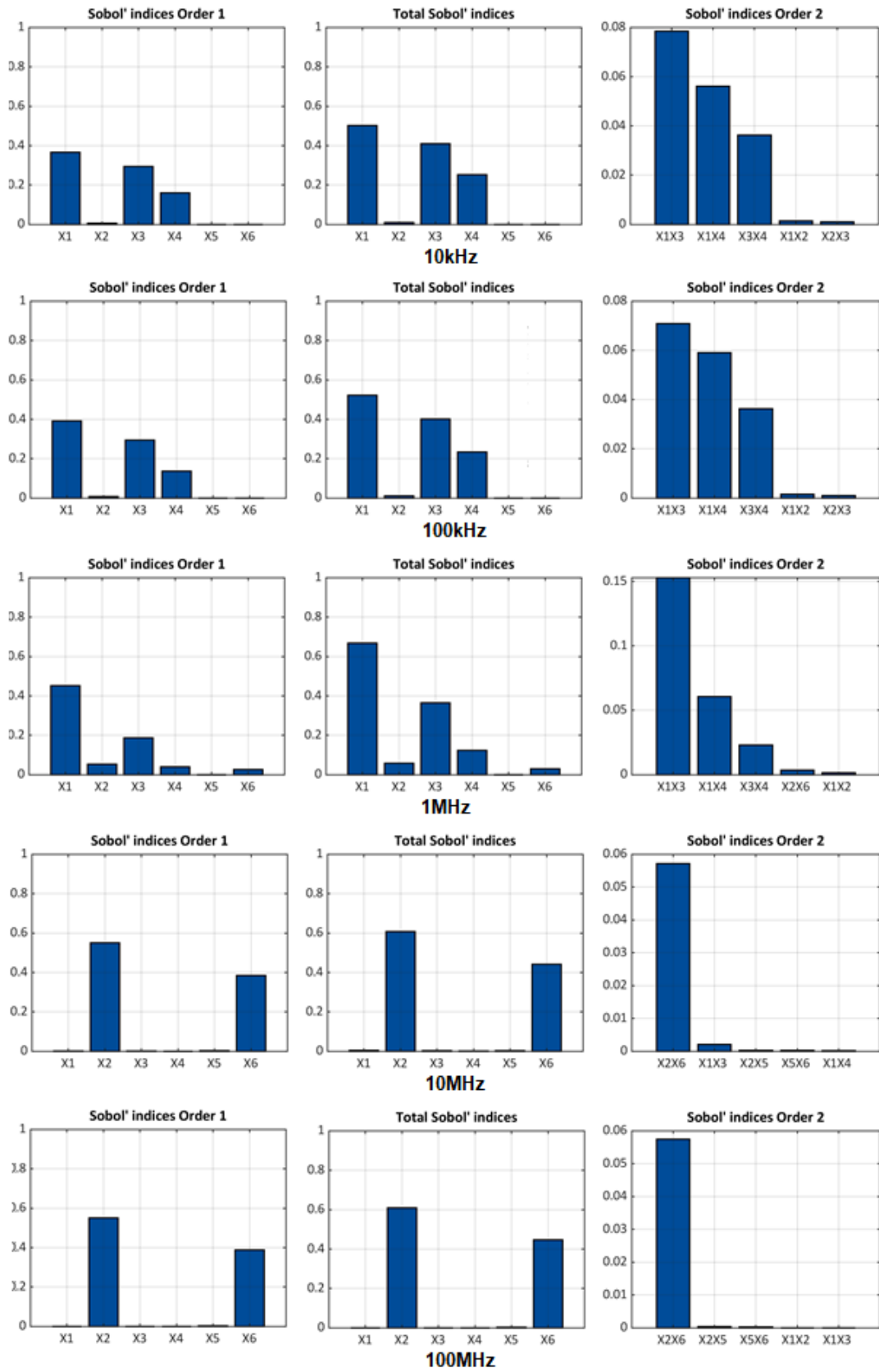
Fig. 6.10: Results for GSA: first-order, total-order and second-order indices

6.5 Results

It is evident from the results that the parameter influences vary considerably for different frequency ranges.

For lower frequencies, the most influential parameters are the basic geometrical dimensions and material properties like shield thickness, conductivity and the inner radius of the shield, which have a direct influence on the DC-resistance and the skin effect losses. The influence of the coverage factor can be considered to be minor. The frequency where the skin effect losses start to dominate can be roughly estimated as the frequency for which the skin depth equals the shield thickness, hence this is highly dependent on the conductivity value and the basic geometry of the cable.

The influence changes for higher frequencies in the inductive region, where the most influential parameters are the coverage factor and the number of apertures (changing the latter is also a way to alter the coverage factor).

6.6 Conclusion

Even though just the most common parameter variations have been demonstrated here, it is clear that small changes in the model can significantly alter the transfer impedance. For evaluating the outcome of altered weave angles, it is of great importance whether the evaluation is executed for a constant cable length or the alterations are assumed to change the length of the cable as well varying the number of the apertures of the cable under test.

Since the possible parameter variations are very extensive, it is of great importance to design the simulation model as exactly as possible to get reliable results and to be able to match the simulated outcome with real world behaviour.

In the author's opinion, the transfer impedance can be simulated fairly accurately for a very precise and specified setup and it is a suitable quantity for cable characterizations.

However, it has been demonstrated that parameter variations are highly influential and it should be kept in mind that, in real-world applications, all possible parameter influences demand a very accurate knowledge of the given test-setup.

7 Circuit Model

This chapter describes the implementation of a circuit model to simulate the transfer impedance in any circuit simulator as, for example, LTspice used in this work.

At first, a model to simulate the skin effect losses of a cable shield is proposed which ultimately is the more challenging part since the aperture leakage then can be implemented by a series inductance (7.1) and the desired transfer impedance is represented by a series connection of the impedances representing skin effect losses and the hole inductance of all apertures:

$$Z_t = Z_s + j\omega L_a \tag{7.1}$$

where the term Z_s represents the DC-resistance and for increasing frequencies the occurring skin effect losses and L_a characterises the inductive behaviour of the shield apertures.

7.1 Modeling skin effect losses

To model the skin effect losses, voltage dependent voltage sources provided by LTspice are used. A voltage dependent source, it can be either a voltage or current source, decouples the single stages of the ladder-network from one another so each single stage remain uninfluenced by the stages before or after.

An exemplary circuit model of four stages is depicted in Fig. 7.1.
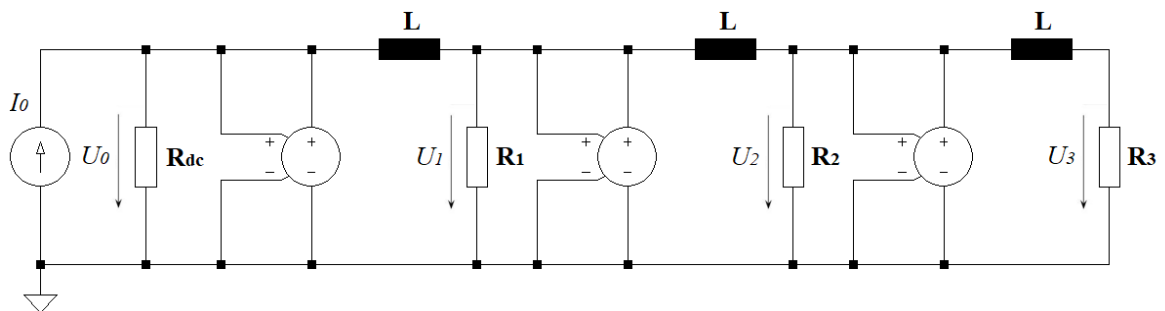
Fig. 7.1: Circuit model for skin effect losses in LTspice

The first stage is used to fix the DC-resistance R_{dc}. The current of the current source is set to 1 Ampere as it is also done with the FEM-model and the measurement setup. Note that, for this variant, the inductance values are kept at a constant value of 1nH and the gain of the dependent voltage sources is kept at constant factor of 1 since it is visible in (7.5) that there is no gain-factor due to the single stages in the magnitude.

The resistance R_1 for the second stage is determined as

$$R_1 = f_{work} \cdot 2 \cdot \pi \cdot L \tag{7.2}$$

where f_{work} is the frequency when the phase of the transfer impedance of the solid shield is at -90 degrees and this frequency point can be obtained as

$$f_{work} = \frac{10}{\sqrt{e}} \cdot f_c \tag{7.3}$$

Furthermore, f_c is again the corner frequency at which the skin depth equals the shield thickness as mentioned in as mentioned in section 6.1 and it is derived as

$$f_c = \frac{1}{d^2 \cdot \mu \cdot \pi \cdot \sigma} \tag{7.4}$$

where d denotes the shield thickness.

If only the magnitude of the transfer impedance is available, f_c is also the frequency point at which the magnitude of the transfer impedance is decreased by the factor $\frac{1}{\sqrt{e}}$.

The other resistance values $R_2 \ldots R_n$ can be approximated with $R_1 \cdot n$ where n is the number of stages of the ladder network.

The voltages of the single stages of the network can then be calculated as:

$$U_0 = I \cdot R_0$$

$$U_1 = U_0 \cdot \cfrac{1}{1 + j\omega \cfrac{L}{R_1}}$$

$$U_2 = U_1 \cdot \cfrac{1}{1 + j\omega \cfrac{L}{R_2}} \tag{7.5}$$

$$\vdots$$

$$U_n = U_{n-1} \cdot \cfrac{1}{1 + j\omega \cfrac{L}{R_n}}$$

Fig. 7.2 shows the magnitude and phase of the simulated results for a shield thickness of 0.5mm for a solid copper shield for a four-ladder network compared to the analytical solution.
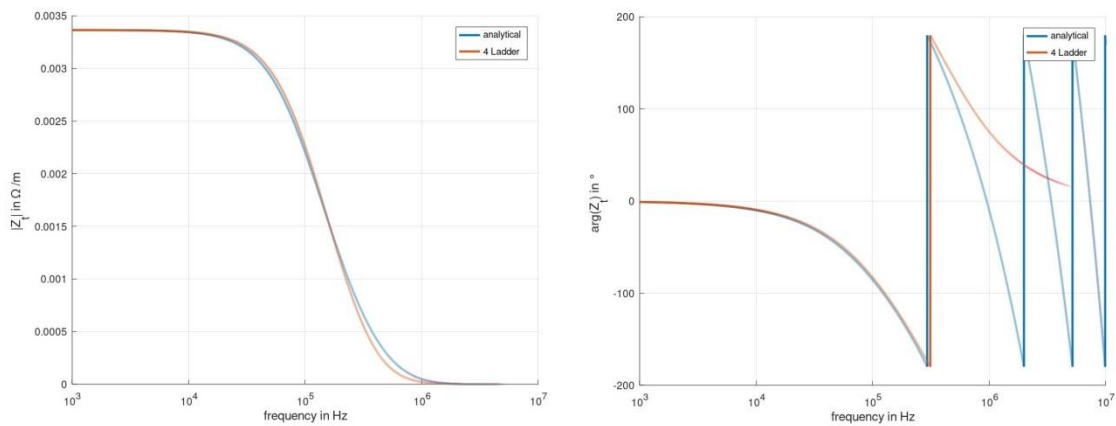
Fig. 7.2: four-ladder network vs analytical model for solid copper shield of 0.5mm thickness

It is noteworthy that the curve shape of the magnitude can be derived even with a two-ladder network, the phase can be approximated for the desired frequency range by increasing the stages if needed. Fig. 7.3 depicts again magnitude and phase of the same solid shield approximated via an eight-ladder network.
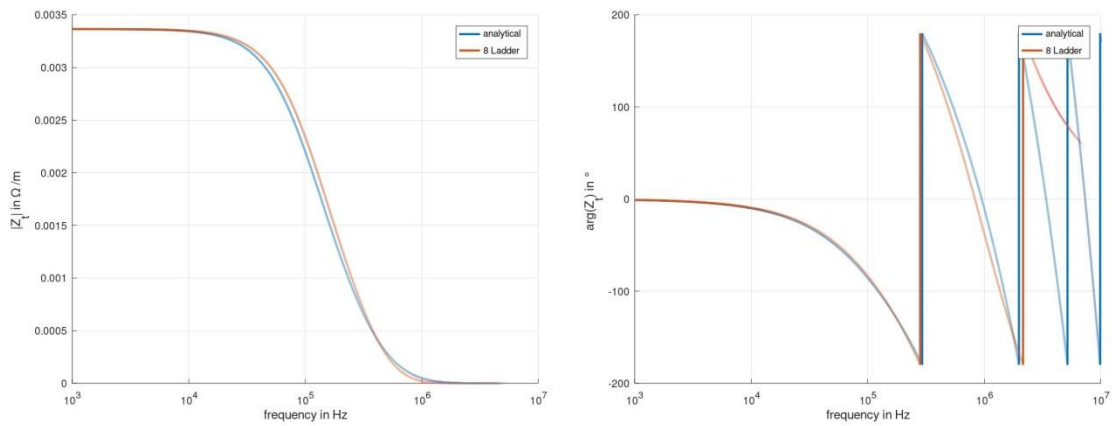
Fig. 7.3: eight-ladder network vs analytical model for solid copper shield of 0.5mm thickness

Fig. 7.4 shows again a four-ladder network simulation compared to the analytical curve for a shield thickness of 0.1mm to demonstrate that this very simple design process is valid for different shield geometries as well.
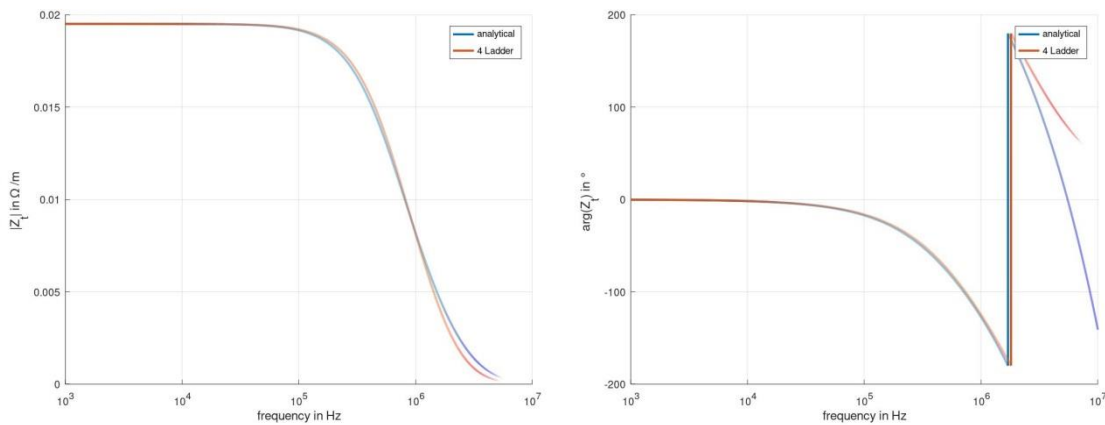
Fig. 7.4: four-ladder network vs analytical model for solid copper shield of 0.1mm thickness

The resistance values of this model are in the mΩ range and therefore it is important to understand the circuit analyser tool as well. In general, inductances in LTspice have some implemented serial resistance to avoid singularities. For the inductance, a default serial resistance of 1mΩ is pre-set. To deal with this parasitic behaviour, there are some alternatives: It is possible to set the parasitic value to zero and develop the model as in (7.5) or, as an example, take the parasitic behaviour into consideration.

In the second case, the voltages of the single stages are calculated as in (7.6) noting that, due to the parasitic resistance R_{par}, the gain of the output voltage has to be corrected. This can be done by dividing the final result by the overall gain of the circuit or by adjusting the gain-values of the single stages of the circuit respectively.

$$U_0 = I \cdot R_0$$

$$U_1 = U_0 \cdot \frac{R_1}{(R_1 + R_{par})} \cdot \frac{1}{1 + j\omega \dfrac{L}{(R_1 + R_{par})}}$$

$$U_2 = U_1 \cdot \frac{R_2}{(R_2 + R_{par})} \cdot \frac{1}{1 + j\omega \dfrac{L}{(R_2 + R_{par})}} \tag{7.6}$$

$$\vdots$$

$$U_n = U_{n-1} \cdot \frac{R_n}{(R_n + R_{par})} \cdot \frac{1}{1 + j\omega \dfrac{L}{(R_n + R_{par})}}$$

Another possibility is to choose a different inductance value to increase the resistance values and, as a consequence, reduce the relative influence of the error of the parasitic resistance R_{par}. Nevertheless, it is always important to fully understand the implemented simulation models and parameters.

To demonstrate that this circuit model is valid for arbitrary shield thicknesses and material properties, the simulated results are compared to the analytical results and this is depicted in Fig. 7.5 and Fig. 7.6.
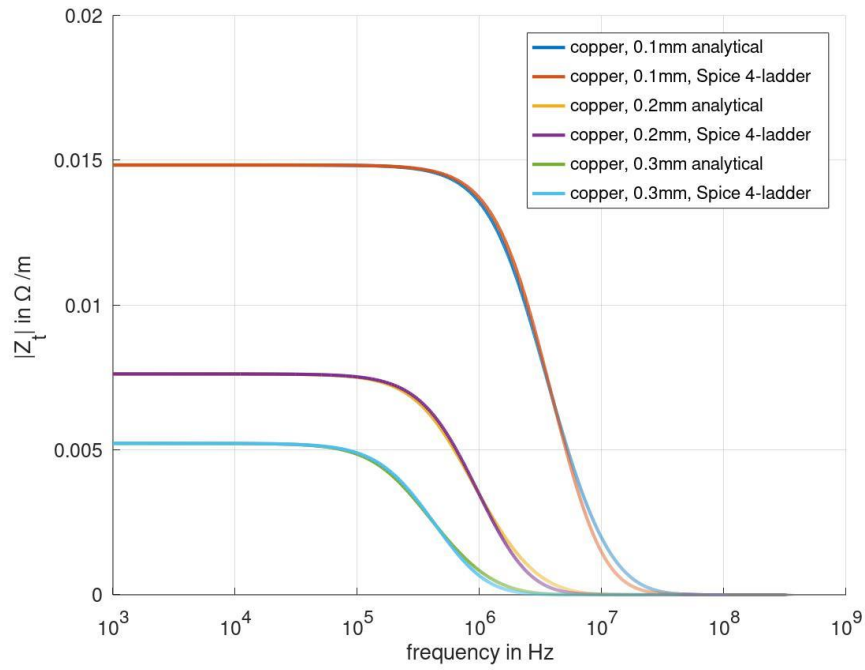
Fig. 7.5: four-ladder network vs analytical results for different shield thicknesses
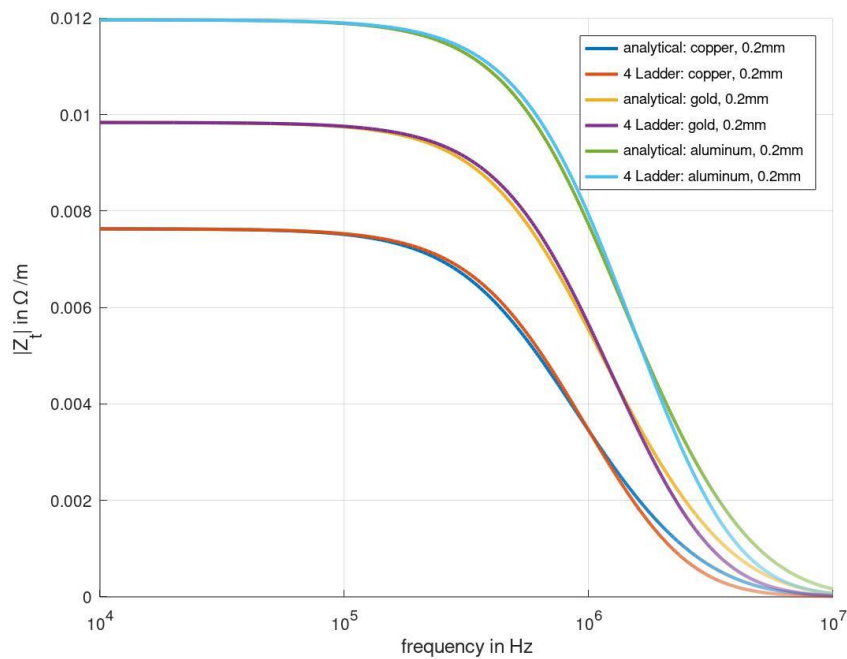
Fig. 7.6: four-ladder network vs analytical results for different material parameters

7.2 Transfer impedance of braided shield

As mentioned in the beginning of this chapter the overall transfer impedance can be simulated as a simple series connection of the DC-resistance and the skin-effect losses, which are both modelled via the circuit model in Fig. 7.1 and the inductance determined by aperture leakage of the shield as in (7.1). The inductance values can be derived analytically, as described in chapter 3 or with the aid of numerical simulation with the finite element model as in chapter 4.

Fig. 7.7 compares the results of the numerical model and the circuit model simulated in LTspice and everything stands in very good agreement.
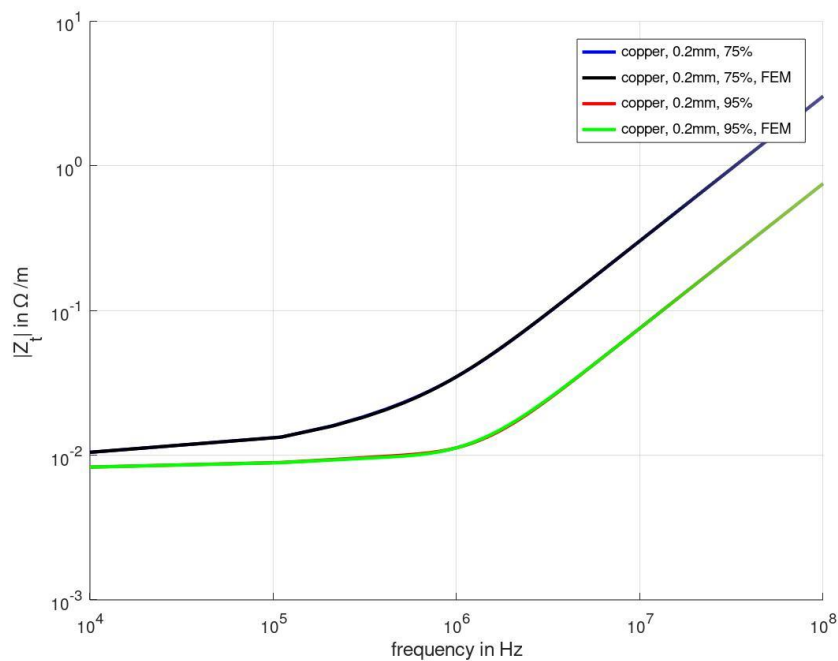
Fig. 7.7: results for numerical simulation and circuit model in LTspice

8 Investigation of spice models for transient voltage suppressor diodes

While the preceding chapters dealt with the broader theory behind the transfer impedance and FEM-based analytics, this chapter deals with the specific case of transient voltage suppressor diodes based on my publication [2].

Transient voltage suppressor (TVS)-diodes are commonly used devices for overvoltage protection against electrical fast transients (EFT/BURST) and electrostatic discharge (ESD) and act as a clamping device for overvoltage peaks. The investigation of these protective measures is an important topic in terms of signal integrity and immunity as well to ensure the correct functionality of subsequent devices.

This investigation is not dominantly focused on the response behaviour of the TVS-diode but on the transient disturbances that are generated by the device itself.

Since these diodes are very common, models are largely available in circuit simulation tools as for example LTspice used in this work.

Concerning the disturbances that are generated by these devices, certain implemented diode- model types can present inaccuracies for this kind of prediction, especially in the cut-off region, which is presumably due to the fact that the model of the implemented junction capacitance follows a linear extrapolation and this leads to differences between the simulated results and the real measured behaviour of the device under test.

For the simulation of this problem setting the measurement setup is considered as a transmission-line and can be simulated in LTspice via the lumped-circuit approach as described in Chapter 2.

8.1 Electrical Fast Transients

The investigated transient phenomena here are electrostatic discharge (ESD) and electrical fast transients (EFT/BURST) as they are described and standardized in [38] and [39].

These waveforms' characteristics are a relatively fast rise time which leads to disturbances at very high frequencies and both of these test cases constitute an important sub-

set of investigations in the field of electromagnetic compatibility in terms of conducted emission, especially immunity.

8.1.1 Electrostatic Discharge - ESD

This pulse is characterized by its very fast rise- and fall-time of its first peak ("initial peak"). Rise-time t_r and fall-time t_f are both within the range of 0.7ns to 1ns and are measured from 10% to 90% of the maximum peak value. The typical pulse shape is depicted in Fig. 8.1. This particular characteristic used here meets the requirements of the system level ESD as characterized in [38].
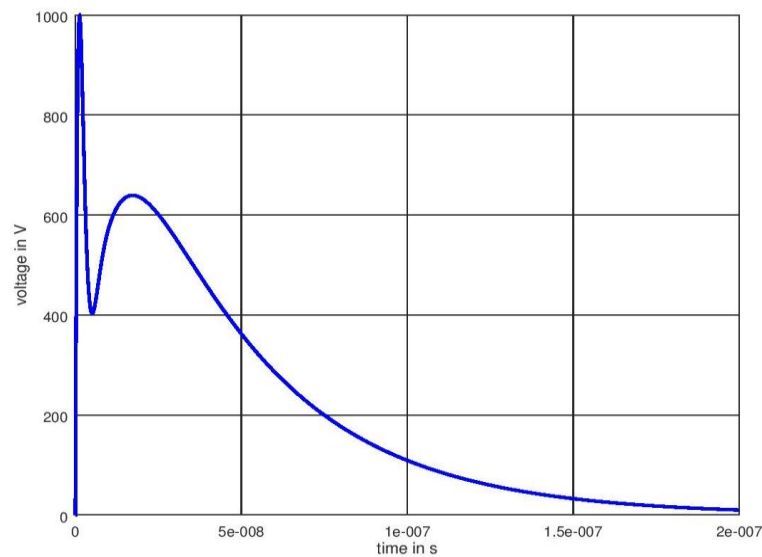
Fig. 8.1: Waveform: ESD-pulse [2], © 2019 IEEE

Nominal peak values of this pulse can range from 500V up to 4kV. Another characteristic for this pulse is its high current level but, due to the fact that this pulse is fairly short, the main disturbances are generated as a result of its fast timing characteristic generating disturbances at very high frequencies rather than in terms of high energy levels.

8.1.2 EFT/BURST

This pulse is characterized by its rise-time and its pulse width as standardized in [39]. The rise- time is nominally between 3.5ns and 6.5ns and the pulse- width should be in the range of 35ns to 65ns. The waveform can be analytically modelled via a double exponential pulse as

$$u(\text{t}) = U_s \cdot k \left(e^{-\alpha t} - e^{-\beta t} \right) \qquad (8.1)$$

as described in [40] where U_s is the maximum value, k is a correction factor and α, β are the parameters defining the characteristic shape as depicted in Fig. 8.2.
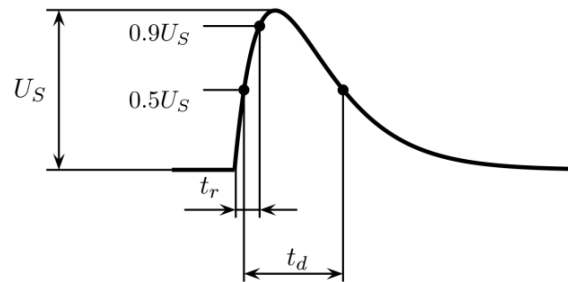
Set Voltage: U_S	Rise-time: t_r	Pulse Width: t_d
1000 V	(5 ± 1.5)ns	(50 ± 15)ns

Fig. 8.2: Waveform: EFT/BURST-pulse with nominal parameters [2], © 2019 IEEE

Again, this pulse generates disturbances at high frequency levels due to its fast rise time. Typical voltage peak levels are again in the range of kilovolts. In this case, the maximum level was set to 1kV to keep the number of destroyed diodes at a minimum.

8.2 Diode models

LTspice features two different diode models [41]. The first standard- or linear model emulates the three linear regions (forward bias region, reverse breakdown region and the breakdown voltage) and the second standard model or non-linear model (Berkely-model) simulates also the non-linear behaviour of this semiconductor device. For the non-linear model, the parameter C_{j0} defined below is very important. It describes the zero bias depletion capacitance and is used for linear extrapolation of the depletion capacitance in the LTspice model:

$$C_j(0) = A_j \sqrt{\frac{e\varepsilon}{2U_J} \frac{N_A N_D}{N_A + N_D}} \qquad (8.2)$$

A_j is the junction area, e is the elementary charge, ε is the material permittivity, N_A is the acceptor concentration, N_D is the donator concentration and U_J is the diffusion- or built-in voltage.

The depletion capacitance as described in [41] and [42] is derived as

$$C_j(U) = \frac{C_j(0)}{\left(1 - \dfrac{U}{U_J}\right)^m} \quad m = \frac{1}{2}\dots\frac{1}{3} \tag{8.3}$$

Fig. 8.3 shows the capacitance as a function of the forward voltage and compares the extrapolated value used in LTspice and the real curve characteristic.
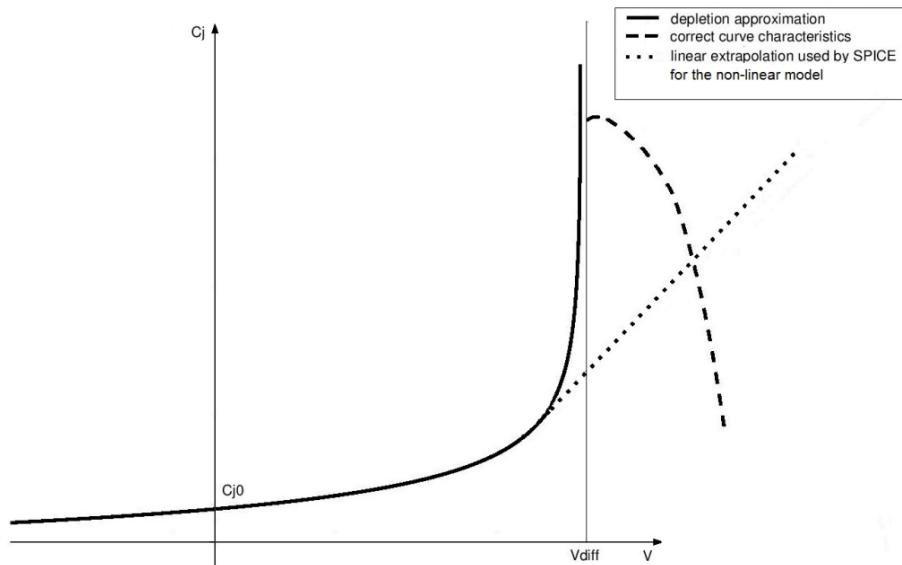
Fig. 8.3: Depletion capacitance in relation to the forward voltage (real behaviour vs non-linear model) [2], © 2019 IEEE

8.2.1 Comparison of the models

Before starting the comparison of the implemented models, it has to be mentioned that no model is either better or correct or wrong. In the course of this investigation, it will be shown that the linear model is the better option for this kind of transient investigation (reverse bias mode). Also, it will be shown later that the response time is more accurate when using the non-linear model since the junction capacitance has an influence on the timing behaviour as well. Anyhow, these are two different kinds of investigation and simulation and one should always understand which model suits the actual demands.

To demonstrate the behaviour of the two different diode- models, a simple simulation setup is used, as depicted in Fig 8.4. It consists of a voltage source applying a rectangular pulse with an edge steepness of 1ns, mimicking the broadband behaviour of electrical fast transient pulses. The wire is simply approximated as a line inductance.
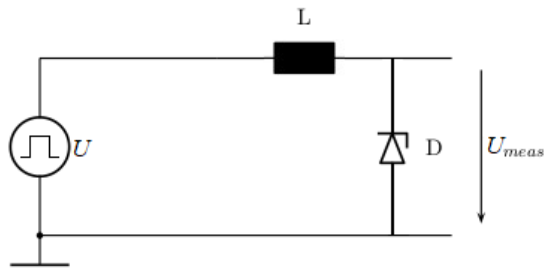
Fig. 8.4: Simple simulation setup [2], © 2019 IEEE

Fig. 8.5 shows the simulated voltage U_{meas} for the linear-model. In this case, no oscillation is present, as expected, since this model does not implement the junction capacitance.
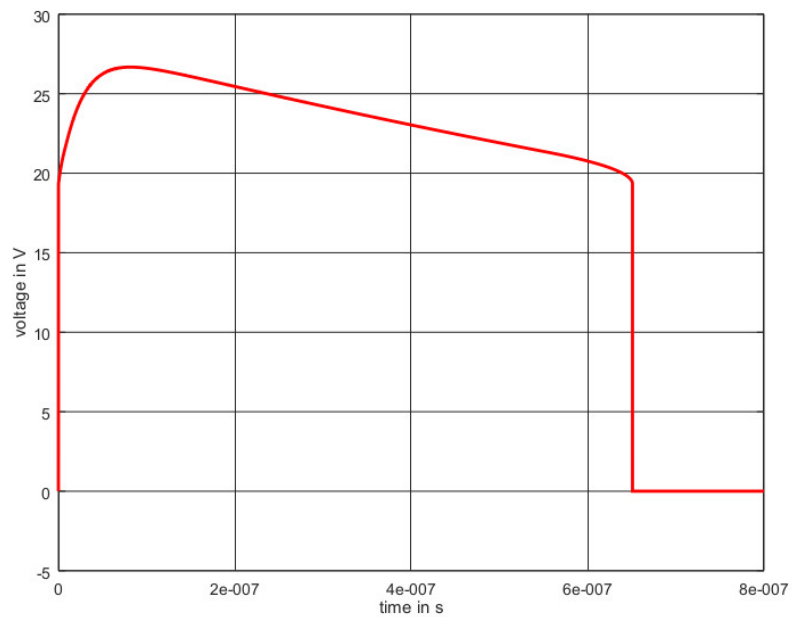
Fig. 8.5: Linear standard-model [2], © 2019 IEEE

In Fig. 8.6, the simulated voltage U_{meas} using the nonlinear model is depicted. In this case the simulated voltage is basically an undamped oscillation with its resonance frequency given as

$$f_0 = \frac{1}{2\pi\sqrt{LC_{diode}}} \tag{8.4}$$

where L is the aforementioned line inductance of the simulation setup and C_{diode} is the residual capacitance value of the TVS-diode model.

From (8.4), the remaining capacitance value can be derived quite easily. It is noteworthy that changing the rise time or amplitude of the voltage source does not impact the results and the derived capacitance value has remained constant.
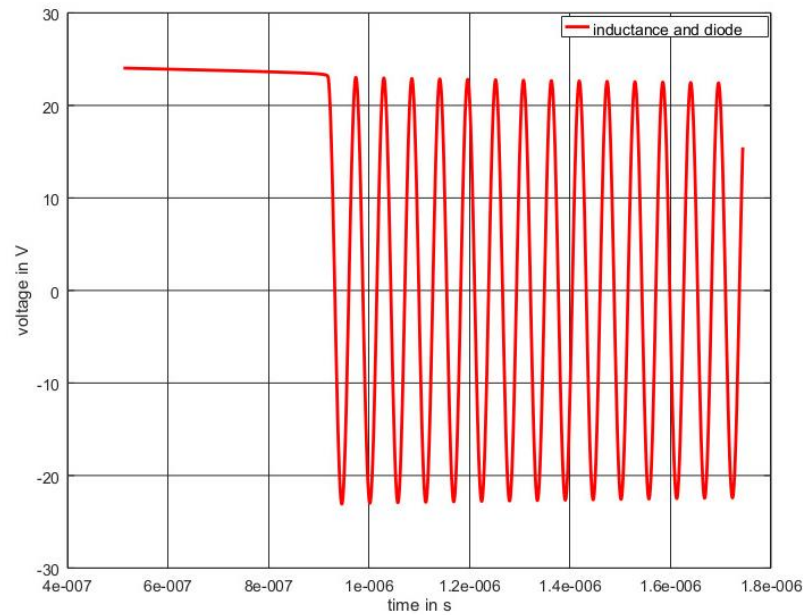
Fig. 8.6: Nonlinear standard-model [2], © 2019 IEEE

Additionally, a measurement setup was built to compare the simulated results to measured results and to check whether the oscillating behaviour is a model limitation or the behaviour is also apparent in the real diode device.

Measurements did not show dependencies of this kind and for further investigations, the simulation setup was improved to reproduce the measurement setup more accurately. The implemented test setup will be explained in section 8.3 and the simulation setup will be discussed in section 8.4.

8.3 Test setup

The used test set up for the measurement that has later been reproduced for simulation, is depicted in Fig 8.7.

It consists of a wire interconnecting the EFT source and the TVS-diode. This connecting transmission line propagates the fast transients induced by the EFT pulse.

The TVS- diode under test is the 5KP20CA from the 5KP Series from Littlefuse, Inc. These diodes are specifically designed for protection of electronic devices against these common voltage transients. The Spice models used for simulation have been taken from the manufacturer's homepage and are compliant to the device used in measurements.

The wire is placed in a controlled distance d above the grounded plane and the TVS-diode is connected to the left end of the wire. To measure the voltage-drop over the diode, an oscilloscope together with a high voltage probe is used. The factor of the voltage probe is 100:1, as depicted in Fig 8.7 as "100:1 PH".

The EFT pulse is applied on the right hand side directly into the line and its amplitude is set to the nominal value of 1000V. For the whole setup it is important that everything is grounded to the same reference plane in order not to distort the measured data.

Simulation and measurements have been carried out for both EFT\BURST and ESD.
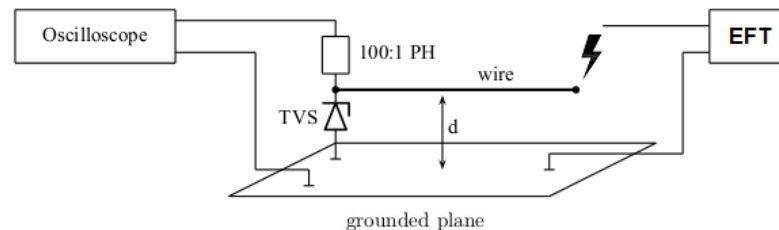
Fig. 8.7: General test setup to measure the voltage drop on the TVS-diode [2], © 2019 IEEE

8.3.1   Practical implementation of the measurement setup

For the measurements, the wire is placed on a 2cm thick layer of polystyrene, in order to keep the distance between the wire and the grounded plane constant.

This height is later needed to determine the parameters for the transmission-line model for simulation. The diameter of the wire is 1mm and the wire length varied between 80cm and 130cm. This is done to get more insight into the influence of the length-dependent line inductance together with the capacitive behaviour of the TVS-diode.

Fig. 8.8 shows the measurement setup and it can be seen that the oscilloscope and the diode are correctly connected to the common grounded plane as also depicted in Fig. 8.7.
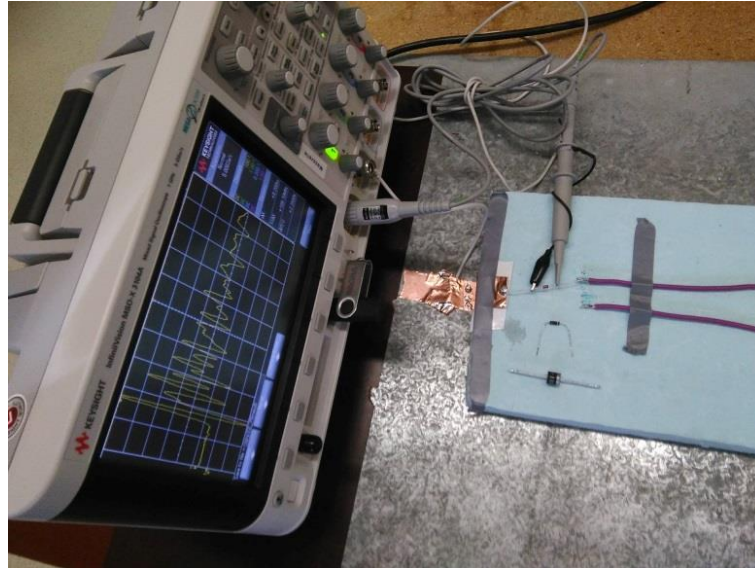
Fig. 8.8: Measurement setup [2], © 2019 IEEE

To keep unwanted interference at a minimum level and avoid coupling between the equipment under test (EUT) and the probe itself, the head of the high-voltage probe was shielded with copper foil, too, since EFT interferes at very high frequencies. The additionally shielded voltage probe can be seen in Fig. 8.9.

Fig. 8.9: Shielding of the probe head [2], © 2019 IEEE

8.4 Simulation setup

To achieve results comparable to measurements, the sources and the wire need to be modelled precisely to match the measurement setup.

8.4.1 EFT Sources

For the simulation setup, the ESD-generator is implemented as a circuit equivalent with the relevant approaches found in [43], [44] and [45]. The maximum amplitude in this case was set to 1000V for measurements and for simulation.

The EFT/BURST testing, the voltage source was modelled as a so called "arbitrary voltage source" in LTspice via the double exponential pulse given in (8.1). Its rise time was set to 5ns and its pulse width to 50ns, again with a maximum amplitude of 1000V to match the input signal used for measurements.

8.4.2 Wire modelling

The wire was modelled as a lossy transmission-line via the lumped element approach as shown in Fig. 8.9.

Since ESD and EFT/BURST generate disturbances in the higher frequency range for the per unit length parameters of the wire, the external inductance (8.5) and capacitance (8.6) suffice due to the dominant skin effect:

$$L = \frac{\mu_0}{2\pi} ln\left(\frac{2d}{r}\right) \quad \text{H/m} \tag{8.5}$$

$$C = \frac{2\pi\varepsilon}{ln\left(\frac{2d}{r}\right)} \quad \text{F/m} \tag{8.6}$$

The parameters are the distance d of the wire above the grounded plane, the radius r of the wire, the permeability of free space μ_0 and the permittivity of free space ε_0 and the relative permittivity ε_r of the polystyrene layer. The AC-resistance R for the maximum occurring frequency is calculated as:

$$R \approx \frac{length_{wire}}{\pi \cdot (2 \cdot r - \delta) \cdot \delta \cdot \sigma} \approx \frac{length_{wire}}{\pi \cdot 2 \cdot r \cdot \delta \cdot \sigma} \quad \Omega / \text{m}, \tag{8.7}$$

where δ denotes the skin depth

$$\delta = \sqrt{\frac{2}{\omega\mu\sigma}} \qquad (8.8)$$

σ is the specific conductivity of copper, r is again the radius of the wire and ω is the angular frequency.

The calculated values were extracted from a 2D-FEM simulation, too, and stand in a good agreement.
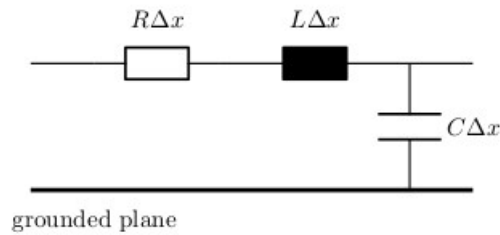
Fig. 8.10: Circuit model of the lossy transmission-line [2], © 2019 IEEE

The propagation delay in s/m of the used line can be derived by the line-parameters as:

$$t_d = \sqrt{L \cdot C} \qquad (8.9)$$

and for the lumped element approach, one segment, in this case called *max_length* , has to be smaller than one-tenth of the wavelength λ as mentioned in section 2.4

$$\mathcal{L} = max\_length \leq \frac{\lambda}{10} \quad . \qquad (8.10)$$

For ESD, the most pessimistic case is a maximum frequency of 1.45GHz and the maximum segment length value for *max_length* is about 2cm or less according to (8.10) and, in this case, the wire with the length of 80cm is divided into a minimum number of 40 lumped elements, called *num_elem* as depicted in Fig. 8.10.

In the case of EFT/BURST, the most pessimistic maximum frequency is 285MHz which leads to a maximum segment length of 10cm and, for the 80cm long cable, a minimum of 8 lumped elements (again *num_elem* as in Fig. 8.11) have to be used.
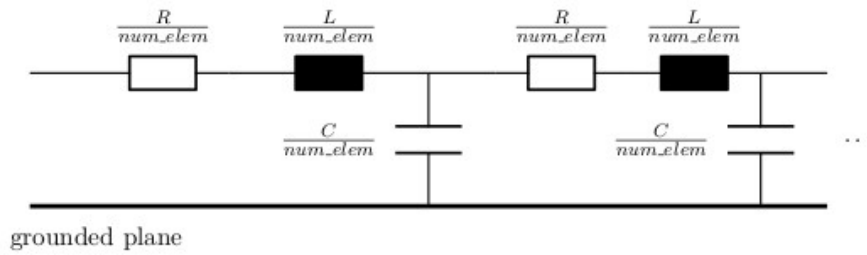
Fig. 8.11: Example of two lumped elements linked together [2], © 2019 IEEE

8.5 Comparison of simulation and measurements

8.5.1 Results for ESD

The LTspice simulation setup for the ESD test is shown in Fig. 8.12 and it consists of the voltage source, the lossy transmission line model implemented as lumped elements and the TVS-diode under test.
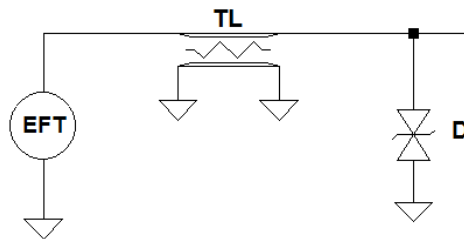
Fig. 8.12: Simulation setup for ESD [2], © 2019 IEEE

The result for the first standard model or the linear model is depicted in Fig. 8.13 where the red waveform shows the simulated voltage compared to the measured waveform in blue.

The linear-model without the implemented capacitance gives actually a quite good agreement compared to the measured data and the ringing of the wire can be simulated as well. This ringing-effect appears because of impedance mismatches of the transmission-line path and is visible as an oscillation of the signal, as depicted in Fig. 8.3.
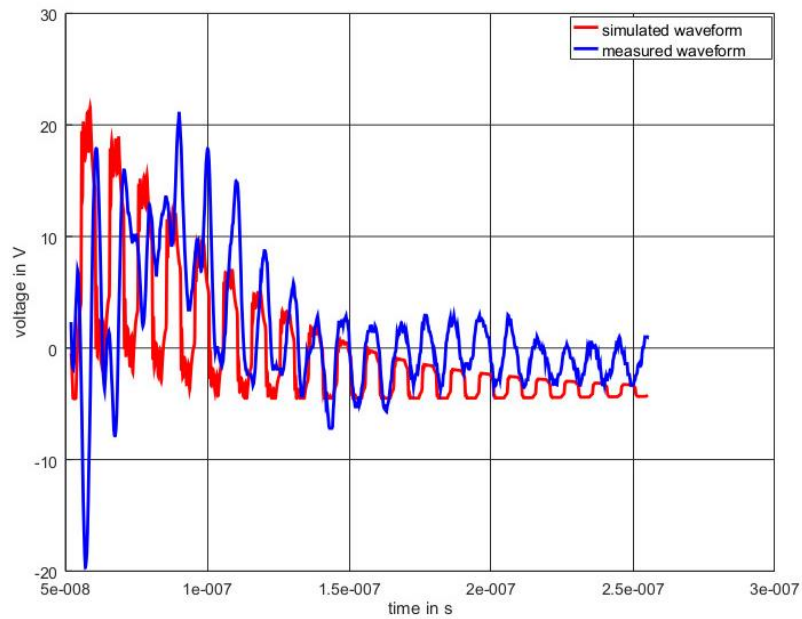
Fig. 8.13: Results: linear TVS-model compared to measurement [2], © 2019 IEEE

Fig. 8.14 shows the direct comparison of the two standard models for the same TVS-diode, where blue is the linear model, as before, and green shows the waveform of the non-linear model with the implemented capacitance C_{j0} .

The clamping response can be simulated with the nonlinear model but the ringing from the wire which is always present due to mismatched termination at either end of the transmission-line cannot be reproduced. It seems that the extrapolated capacitance value has a significant influence on the simulated result.
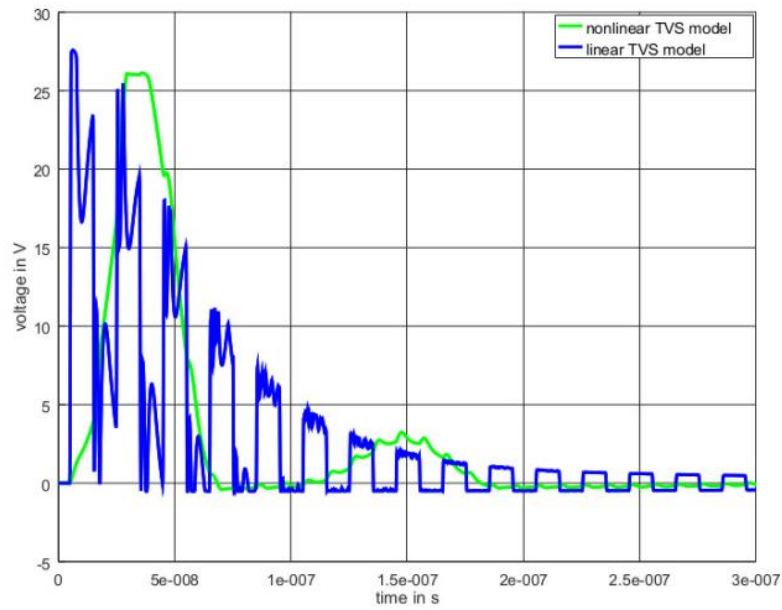
Fig. 8.14: Comparison: linear and non-linear diode model [2], © 2019 IEEE

8.5.2 Results for EFT/BURST

For EFT\BURST, the same setup was used for simulation and measurements as depicted in Fig. 8.15. The coupling of the EFT pulse is via 50Ω as recommended in [39].
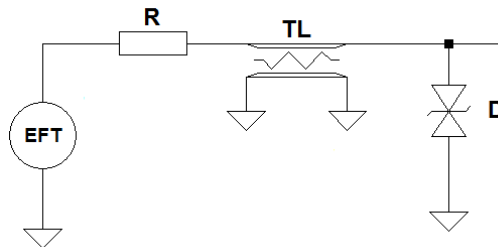
Fig. 8.15: Simulation setup for EFT/BURST [2], © 2019 IEEE

In Fig. 8.16, the measurement in red is compared to the simulated result in blue for the nonlinear-model.
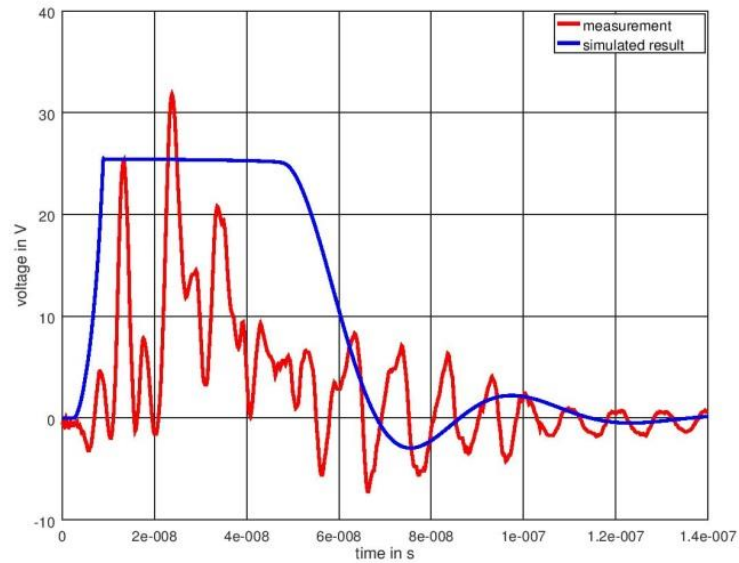
Fig. 8.16: Results: measurement vs nonlinear-model [2], © 2019 IEEE

Again with the nonlinear-model with the implemented capacitance C_{j0}, the simulated results do not match with measurements. The non-vanishing capacitance value, together with the inductance parameter of the transmission-line distort the simulated voltage.

Since, most of the time, non-linear diode-models are provided by the manufacturers, the influence of the extrapolated capacitance value can be easily eliminated by setting the parameter C_{j0} to zero. The result can be seen in Fig. 8.17.

With the modified model the expected waveform can be approximated and also the ringing of the transmission line is visible.
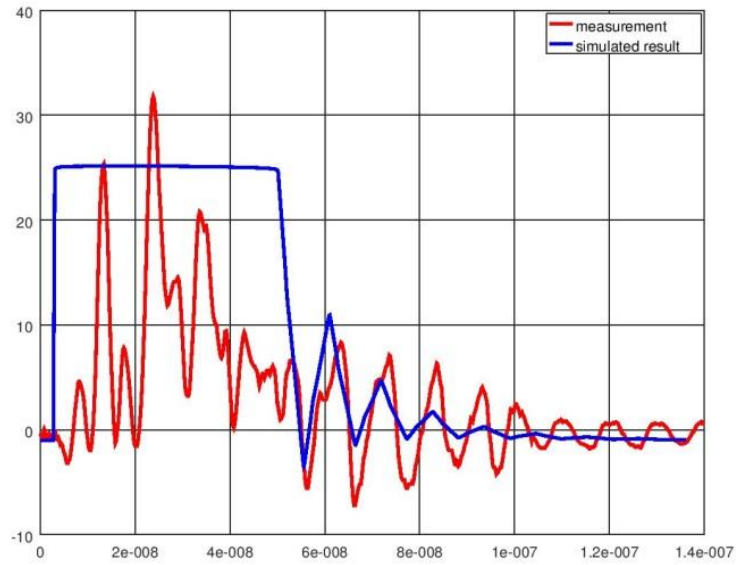
Fig. 8.17: Results: measurement vs modified nonlinear-model [2], © 2019 IEEE

In Fig. 8.18 the direct comparison between the modified model and the model provided by the manufacturer (non-linear model) is depicted.
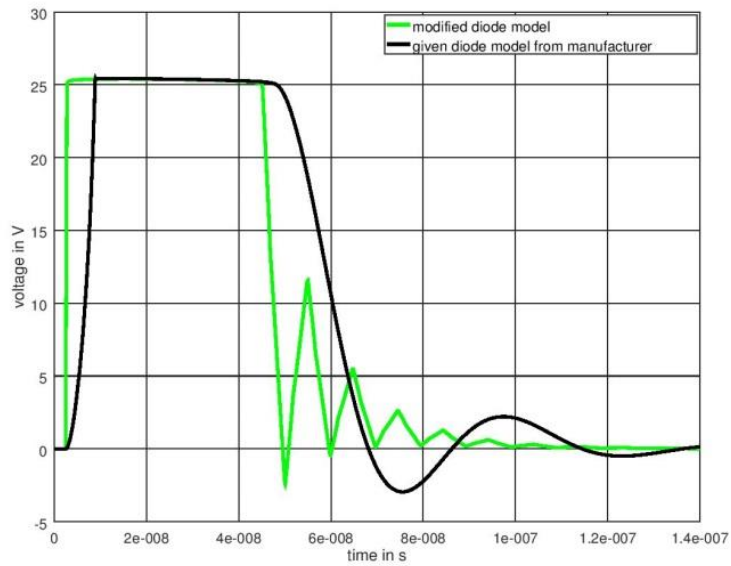
Fig. 8.18: Comparison: modified non-linear model vs nonlinear-model [2], © 2019 IEEE

In case of the non-linear model, the responsiveness of the time-depending clamping behaviour can be observed, but it is not possible to give any statement regarding the actual transient behaviour.

As for the case of the modified model, the transient behaviour can be observed but the correct time-depending clamping behaviour is not simulated correctly.

In Fig. 8.19 the difference between the modified non-linear model and the linear model is shown and their behaviour for transient analysis is quite similar.
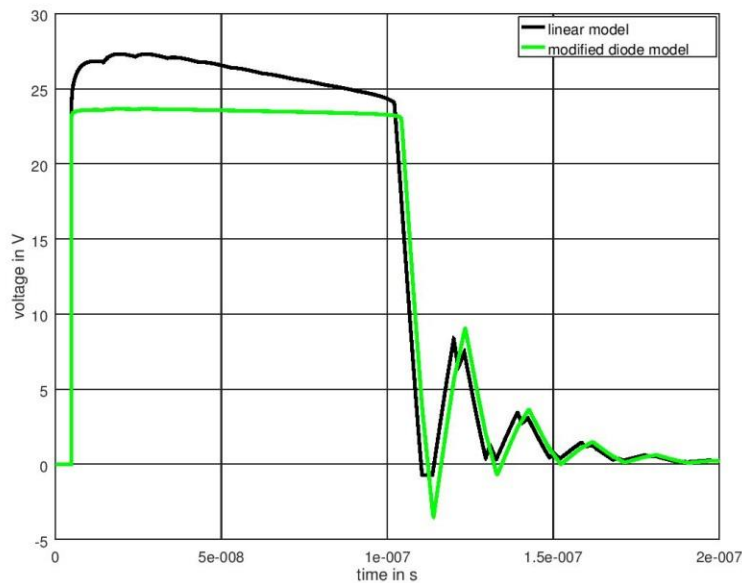
Fig. 8.19: Comparison: linear model vs modified non-linear model [2], © 2019 IEEE

So, even if no linear models are available for the simulation, setting C_{j0} to zero can give some improvement in simulating the transient response.

8.6 Conclusions

This study shows quite well that, in order to be able to simulate a realistic behaviour, it is not only important to understand the limitations of the models and their application areas but also to model sources and network elements with sufficient precision.

It has become clear that the simulation outcome of the transient behaviour of TVS-diodes as overvoltage protection devices is very much dependent on the implemented diode-model in the circuit simulator. The linear model of the diode might be more simplified but it represents a better option for this kind of transient investigation.

If no linear models are available, setting the capacitance C_{j0} to a minimum value of $0\,pF$ can provide more satisfactory results in this specific application operating in the reverse bias mode. Nevertheless, it is always recommended to compare simulated results with measured data.

As mentioned at the beginning of this chapter, every diode model has its advantages and disadvantages and its different areas of application and it is always important to understand given models to use them in a way to gather meaningful results.

9   Parameter extraction for Capacitive Coupling Clamp test setup

This chapter deals with the measurement method of the so called capacitive coupling clamp and the simulational approach thereof [6].

The capacitive coupling clamp test setup is a standardized immunity test method of electronic devices against electrical fast transients (EFT) that has been established by the International Electrotechnical Commission [39].

The capacitive coupling clamp is a measurement setup to investigate conducted electromagnetic interference without a direct galvanic connection between the cables under test and the clamp itself.

A fast EFT pulse with a rise-time in the range of nanoseconds is applied to the coupling clamp and the robustness of the inserted cable harness against EFT can hence be examined.

The goal of this chapter is to extract the network parameters of this test-procedure to gather equivalent circuit models to simulate in circuit analysers like LTspice. This is done with the use of the FEM-method described in Chapter 2.

Since the whole setup can be viewed as a multi-conductor-transmission line, the LTspice simulation can again be carried out with the aid of the lumped-circuit approach described in Chapter 2.

Using simulations during different design processes of electronic devices is an efficient way to estimate the robustness of the devices against EMC-requested standards and to prevent costly redesigns of the final product.

Analytical approaches to calculate the circuit elements can be found in [46] and [47] but the advantage of the Finite Element Method lies in a more precise modelling of the geometry and also in the fact that the influence of the insulation material can be taken into account without loss of accuracy.

The setup and the desired network-representation are explained in sections 9.1 and 9.2. The parameter extraction procedure for the circuit-model is described in section 9.3.

9.1 General setup

Fig. 9.1 depicts the general setup of this measurement method and it is based on IEC61000 − 4 − 4 [39]. For the development of the circuit-model, the setup is divided into three segments, as indicated in Fig. 9.1, depicting the overall setup.

The first segment on the left, denoted section A, consists of n PVC-insulated copper wires of length l_a, which is 10cm. The wires are arranged parallel at a required distance of 10cm above a ground reference plane. This "cable harness" enters the middle segment denoted section B. This section consists of the triangle-shaped aluminium housing, the capacitive coupling clamp, of a specified length l_b of 1m, again 10cm above the ground reference plane.

On the right side, the cable harness is guided along the distance l_a of 10cm in free air over the ground reference plane again. This segment is identical to section A.
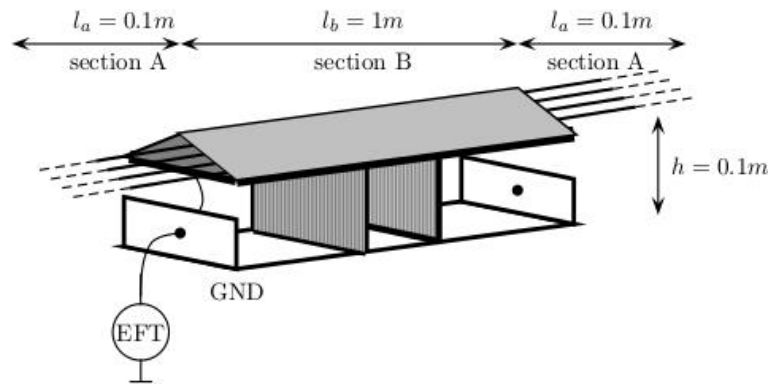
Fig. 9.1: General setup, based on IEC [6], © 2017 IEEE

The wires are terminated by 50Ω resistors and the EFT pulse is impinged by an impulse generator, also called BURST-generator, into the aluminium case against the ground reference plane. The waveform and characteristics of this pulse is the same pulse as mentioned in section 8.1.2 and the parameters of this double exponential pulse are derived as

$$u(t) = k \cdot U_S \left[e^{-\frac{t}{64.8ns}} - e^{-\frac{t}{4.02ns}} \right]$$

(9.1)

with k representing an amplification factor [40] to adjust the used test voltage-level to 200V.

The rise time of the applied test pulse nominally is 5ns but given tolerances range between 3.5ns and 6.5ns. Therefore the fastest possible rise-time that is still within the limit given in [39] is 3.5ns and therefore the chosen operating frequency for parameter-extraction in section 9.3 is set to 285MHz. This is applies for developing the circuit-model in section 9.4 as well.

9.2 Network representation of the setup

To obtain a network representation of this given setup, it is viewed as a multi-conductor transmission line problem. For this representation, essential knowledge regarding the mutual inductances and the coupling capacitances of the conductors and the capacitive coupling clamp has to be gathered. In the further course, special focus is put on obtaining valid and accurate circuit parameters by the use of appropriate finite element simulations.

For this investigation, four parallel PVC- insulated copper wires with a conductor diameter of $d = 1.1mm$ are used. The isolation thickness is $0.6mm$ and the relative dielectric constant $\varepsilon_r = 3$ for PVC is taken.

Due to the different arrangements of section A and section B of the general set-up, they are studied separately.

9.2.1 Section A – Parallel wires above a grounded plane

For this section, the wires are placed parallel with certain distances s between each other, 10cm above the ground reference plane as depicted in Fig. 9.2. As a consequence the isolation material ε_r of the wires has to be taken into consideration.
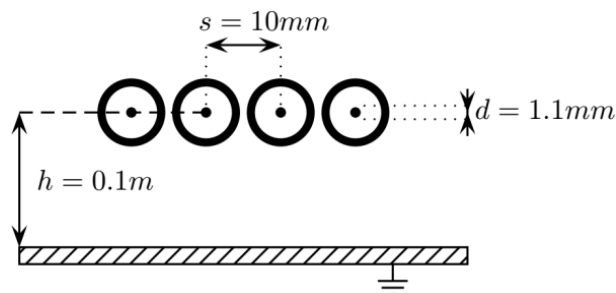
Fig. 9.2: Cross section and model dimensions of section A [6], © 2017 IEEE

The equivalent representation of this multi-transmission line model with the lumped element approach is depicted in Fig. 9.3 where $L_{n,n}$ denote the self-inductances of the

single wires and $L_{k,n}$ the mutual inductances between the wires just as C_n represents the capacitive coupling between a single wire and the ground reference plane and $C_{k,n}$ describes the capacitive coupling between the wires. R represents the AC-resistance of the copper wire for the selected frequency of 285MHz, modelling the impedance rise due to the skin-effect, as it is also described in section 8.4.2.
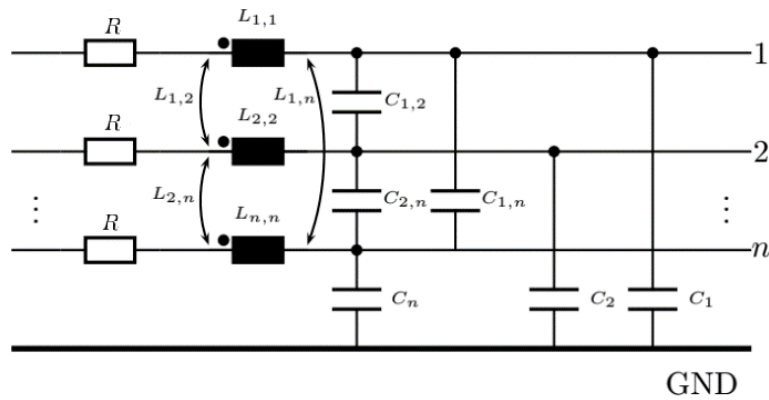
Fig. 9.3: Circuit model of the isolated wires above grounded plane, lumped elements [6], © 2017 IEEE

9.2.2 Section B – Clamp housing cables

Section B, consisting of the capacitive coupling clamp with the inserted wires, is depicted in Fig. 9.4.
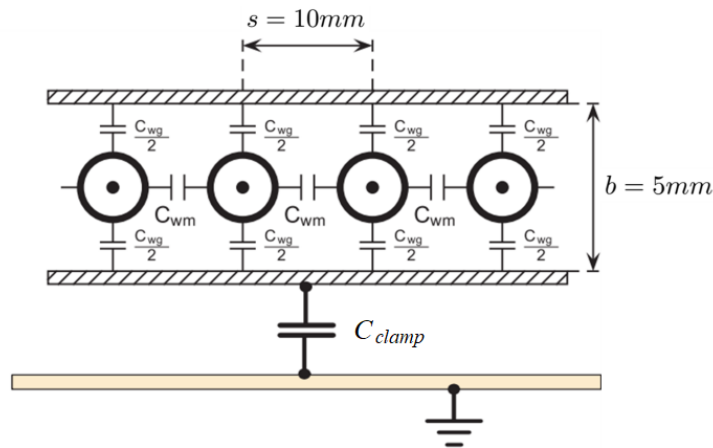
Fig. 9.4: Cross section of the model, capacitances indicated [6], © 2017 IEEE

The spacing between the wires and the spacing between the wires and the ground reference plane remain the same as in section A. The main difference here is that the coupling clamp adds an additional conductor to this setup.

The triangular shape of the real coupling clamp is simplified by the use of two parallel aluminium plates. In Fig. 9.4, the capacitive coupling between the coupling clamp and the inserted wires and the clamp to ground is depicted as well.

Fig. 9.5 shows the equivalent multi-transmission line model as it can be applied for any circuit simulator. R again stands for the AC-resistance as also mentioned in the previous section, $L_{b_{nn}}$ are the self-inductances of the wires, $L_{b_{n,clamp}}$ describe the mutual inductances between the n wires and the clamp plates, $L_{b_{k,n}}$ describe the mutual inductances between the wires and L_{clamp} represents the inductance of the clamp-plates with respect to the ground-reference plane.
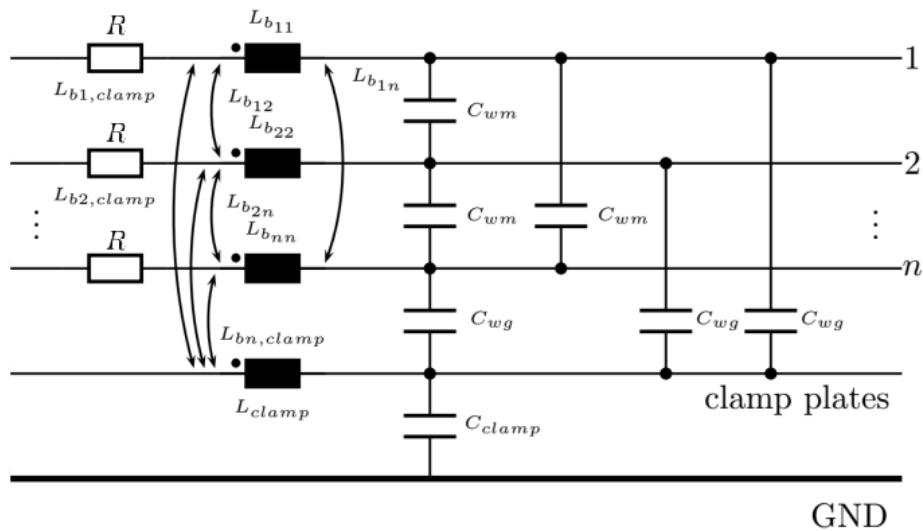
Fig. 9.5: Circuit model of the coupling clamp housing cables above a grounded plane [6], © 2017 IEEE

The capacitance values, also depicted in Fig. 9.5, C_{wm} describe the mutual capacitive coupling between the wires, C_{wg} give the capacitive coupling between the single wires and the clamp-plates and C_{clamp} stands for the capacitance value between the clamp-plates and the ground-reference plane.

9.3 FEM- based circuit parameter extraction

To obtain the parameters for the multi-transmission line models for circuit simulators, the electric and magnetic coupling have each to be treated with different kinds of numerical FEM-computations as mentioned in Chapter 2.

The used methodologies are explained in the following sections and as mentioned in section 9.1 the parameter extraction is done for a frequency of 285MHz.

9.3.1 The capacitive coupling: quasi-static electric computations

For the capacitive coupling, the capacitance matrices for both sections, section A $[C_A]$ and section B $[C_B]$ have to be determined.

For section A, all capacitive coefficients of the wires against ground and all mutual capacitive coefficients as well have to be computed as they are described in section 9.2.1.

For section B, as described in section 9.2.2, the capacitive coupling coefficients between the wires and the clamp plates and the mutual coefficients of the wires itself have to be derived. Additionally, the capacitance of the capacitive coupling in relation to the ground reference plane has to be found as well. This leads to an additional electrode for section B considering the clamp.

Quasi-static electric computations are carried out to derive the distributed capacitances of every section.

In general, the setup including ground consists of n electrodes and therefore $(n-1)$ FEM-computations are carried out consecutively by setting the potential of one electrode to 1V while all other electrodes are set to zero potential. After each FEM-computation, the influenced charge quantities Q_n on all n electrodes can be derived and the capacitance coefficients can be obtained as in (9.3).

The applied procedure can be summarized as:

$$\forall n = 1,\dots n \quad electrodes$$

$$U_{em1} = \begin{cases} U_{em1} = 1\,V & n = m \\ U_{em1} = 0\,V & n \neq m \end{cases} \tag{9.2}$$

$$C_{mn} = \frac{Q_n}{U_{em1}} \tag{9.3}$$

and the capacitance matrix $[C]_{NxN}$ is assembled elementwise.

The number of electrodes for section A is always one less than for section B, since section A does not include the coupling clamp.

9.3.2 The inductive coupling: quasi-static magnetic computations

For the inductive coupling, FEM-simulations using the **A**V,**A**-formulation are carried out, as described in Chapter 2.

To gather the inductance matrices, $[L_A]$ for section A and $[L_B]$ for section B, both the self-inductances and the mutual inductances of all conductors have to be derived, as they are described in section 9.2.1 and 9.2.2.

Analogously to the method for the capacitive coupling, the procedure is again carried out sequentially, but in this case a current of 1A is applied successively on each of the conductors, whereas the other conductors remain at 0A.

The induced voltages U_{e_n} due to the inductive coupling can be post-processed after each FEM-computation and this gives knowledge of the impedance matrix $[Z]_{NxN}$ for the multi-conductor systems. The procedure applied to both sections separately is summarized as:

$$\forall n = 1, \dots n \quad conductors$$

$$I_{nm} = \begin{cases} I_{nm} = 1 \ A & n = m \\ I_{nm} = 0 \ A & n \neq m \end{cases} \tag{9.4}$$

$$z_{mn} = \frac{U_{e_n}}{I_{nm}} \tag{9.5}$$

and the impedance matrix $[Z]_{NxN}$ is assembled elementwise as in (9.5) and the inductance matrix $[L]_{NxN}$ can be derived directly from these results.

Again, section B has one more conductor than section A because of the clamp.

9.4 Model for circuit simulator

After extracting the per-unit length parameters for both sections the whole setup can be assembled. Fig. 9.6 depicts the schematic diagram of the whole setup demonstrating the interconnection of section A and section B.

This lumped element model of the multi-transmission line equivalent circuit can be simulated via common circuit simulators. In this case the circuit simulator LTspice is used.
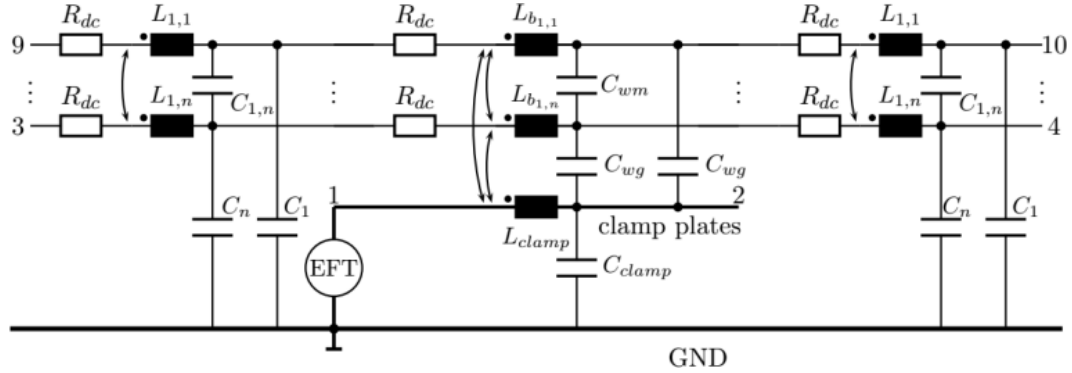
Fig. 9.6: Overall system, interconnecting the networks for section A, section B and section A [6], © 2017 IEEE

This lumped element approach is valid as long as the problem setup can be considered to be electrically short and again the following condition holds as mentioned in section 2.4:

$$\lambda = \frac{c}{f_{max}} \Rightarrow \mathcal{L} = len \leq \frac{\lambda}{10}. \qquad (9.6)$$

where *len* is the maximum length of one subsection of the lumped element model.

The maximum frequency f_{max} is 285MHz, as mentioned in section 9.1, and therefore the maximum segment length *len* has to be shorter than 10cm for every single segment. For the LTspice model, a maximum segment length of 5cm has been chosen to definitely meet the needed condition and, therefore, section A is modelled via two segments to arrive at the total length of 10cm and section B is modelled via twenty segments since this section has a length of 1m.

9.5 Results

For the measurements and the LTspice simulations as well, ports 4 to 10 on the right hand side of the setup are terminated with 50Ω each and the coupling clamp, denoted as Port 2 in Fig. 9.6 and the ports on the left side of the BURST generator are operated in open-circuit.

The applied maximum peak voltage for the test pulse has been set to 200 V for measurements and simulations and the results are compared in Fig. 9.7.
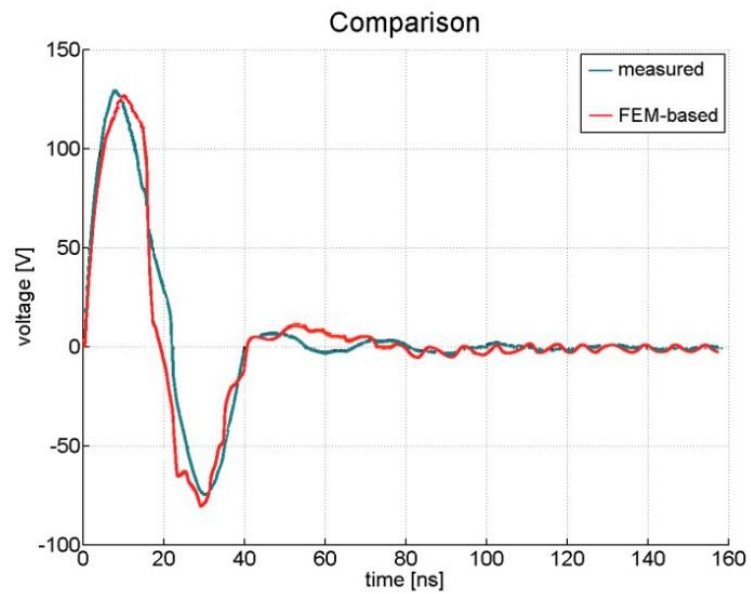
Fig. 9.7: Comparison between simulated and measured results [6], © 2017 IEEE

The simulated output voltage is 131V and the measured output voltage is 134V which leads to a deviation between the simulated and measured results of less than 5% indicating an acceptable agreement between these two methods.

10 Further Work

For the FEM model so far, the apertures of the shield are inserted in a solid conducting screen. Further investigation might contain a detailed model of the single carriers of the braided cable shield. This might be very interesting in investigating the influence of partially damaged cable shields of broken single strains and their influence on the transfer impedance and the shielding effectiveness.

In this work, the geometry can be altered to mimic stretched or compressed cable shields by analysing different geometries of the rhombic apertures varying the coverage factor. Another possible task would be to extend the cable model to investigate not only different shield geometries but also geometry deformations occurring with general cable alterations, such as twisted or heavily bent cables. Different cable layouts will also lead to different shield alterations and this influence might be worth investigating.

Different shielding geometries and cable types can be investigated as well and manageable simulation models could be developed.

For all the above mentioned cable alterations, not only the transfer impedance is a characteristic parameter of interest, also the electric field penetrating the apertures has to be investigated, especially in the case of cable harnesses and the resulting capacitive coupling between cables and the effect on signal transmission.

The next step could also be to analyse cable harnesses and reliable simulation approaches of them, especially focusing on capacitive- and inductive coupling with respect to electrical fast transients [48].

References

 [1] LTspice download link, https://www.analog.com/en/design-center/design-tools-and-calculators/ltspice-simulator.html

[2] S. Bauer et al., "Investigation of SPICE Models for Overvoltage Protection Devices With Respect to Fast Transients," in *IEEE Letters on Electromagnetic Compatibility Practice and Applications*, vol. 1, no. 1, pp. 20-25, March 2019

[3] S. Bauer et al., "Time domain FEM computational approach for calibration of surface scan method," in *IEEE International Symposium on Electromagnetic Compatibility and 2018 IEEE Asia-Pacific Symposium on Electromagnetic Compatibility (EMC/APEMC)*, Singapore, 2018, pp. 866-871

[4] S. Bauer, B. Deutschmann and G. Winkler, "Prediction of the robustness of integrated circuits against EFT/BURST," in *IEEE International Symposium on Electromagnetic Compatibility (EMC)*, Dresden, 2015, pp. 45-49

[5] A. Lavarda, D. Amschl, S. Bauer and B. Deutschmann, "Characterization of the immunity of integrated circuits (ICs) at wafer level," in *10th International Workshop on the Electromagnetic Compatibility of Integrated Circuits (EMC Compo)*, Edinburgh, 2015, pp. 196-201

[6] S. Bauer, W. Renhart and O. Bíró, "FEM-Based Computation of Circuit Parameters for Testing Fast Transients for EMC Problems," in *IEEE Transactions on Magnetics*, vol. 53, no. 6, pp. 1-4, June 2017

[7] S. Bauer, C. Türk, W. Renhart and O. Bíró, "Finite element analysis of cable shields to investigate the behavior of the transfer impedance with respect to fast transients," in *IEEE 23rd Workshop on Signal and Power Integrity (SPI)*, Chambéry, France, 2019, pp. 1-4

[8] C. Tuerk, D. J. Pommerenke and S. Bauer, "Improved Alternative Method For Fast And Simple Transfer Impedance Measurements," in *IEEE Letters on Electromagnetic Compatibility Practice and Applications*, (early access)

[9] C. Tuerk, S. Bauer and D.J. Pommerenke, "Alternative Method for Transfer Impedance Measurements," (accepted) in *International Symposium on Electromagnetic Compatibility,* 2020

[10] S. Bauer et al., "Sensitivity Analysis of the Transfer Impedance of Shielded Cables with Braided Shields Using a Parametrized FEM Model," Abstract in *19th Biennial IEEE Conference on Electromagnetic Field Computation*, 2020

[11] O.Bíró, "Edge element formulations of eddy current problems," in *Computer Methods in applied Mechanics and Engineering*, Vol. 169, Issues 3-4, pp391-405, 1999

[12] O.Bíró, K. Preis, "On the use of the magnetic vector potential in the finite-element analysis of three-dimensional eddy currents," in *IEEE Transactions on Magnetics*, Vol. 25, No. 4, July 1989

[13] K. Preis, "Anwendung der Methode der finiten elemente zur numerischen Berechnung elektromagnetischer Felder," Habilitationsschrift, TU-Graz, 1983

[14] K. Preis, O. Bíró, K. R. Richter, H. Resinger, K. Papp, "Nonlinear periodic eddy currents in single and multiconductor systems," in *IEEE Transactions on Magnetics,* Vol. 32, No 3, part 1, pp. 780-783, 1996.

[15] K. Hollaus, B. Wagner, O.Bíró, "Simulation of the quasi-static electric field by an electric current vector potential approximated by edge elements," in *COMPEL - The international journal for computation and mathematics in electrical and electronic engineering*, Vol 24, No. 2, pp 581-590, 2005

[16] C.R. Paul, "Analysis of Multiconductor Transmission Lines," in *IEEE Press*, John Wiley & Sons, INC., 2008, Second Edition.

[17] C. R. Paul, "Introduction to Electromagnetic Compatibility," John Wiley & Sons, INC., 2006, Second Edition

[18] S. A. Schelkunoff, "The electromagnetic theory of coaxial transmission lines and cylindrical shields," in *The Bell System Technical Journal*, Vol. 13, Issue 4, Oct. 1934

[19] A. Tsaliovich, "Cable shielding for electromagnetic compatibility," Chapman&Hall, 1995

[20] R. Otin, J. Verpoorte, H. Schippers, "Finite Element Model for the Computation of the Transfer Impedance of Cable Shields," in *IEEE Transactions on Electromagnetic Compatibility*, Vol. 53, Issue 4, Nov. 2011

[21] S. Celozzi, R. Araneo, G. Lovat, "Electromagnetic Shielding," in *IEEE Press*, Wiley- Interscience, John Wiley & Sons, INC., 2008

[22] H. A. Bethe. "Theory of diffraction by small holes," in *Phys. Rev.*, vol. 66, no. 7–8, pp. 163–182, Oct. 1944

[23] R. E. Collin, ''Field Theory of Guided Waves,'' in *IEEE Antennas and Propagation Society*, IEEE Press, 2nd Edition, 1990

[24] J. A. Stratton, ''Electromagnetic Theory,'' in *IEEE Antennas and Propagation Society*, IEEE Press Series on Electromagnetic Wave Theory, 2007

[25] F. M. Tesche, M. V. Ianoz, T. Karlsson,'' EMC, Analysis Methods and Computational Models,'' John Wiley & Sons, INC., 1997

[26] E. F. Vance, "Shielding Effectiveness of Braided-Wire Shields," in *IEEE Transactions on Electromagnetic Compatibility*, vol. EMC-17, no. 2, pp. 71-77, May 1975

[27] M. Tyni, "The transfer impedance of Coaxial Cables with Braided Outer Conductor," Digest of the 10th International Wroclaw Symposium on EMC, 1976, pp. 410-419

[28] B. Demoulin, P. Degauque, "Shielding Effectiveness of braids with High Optical Coverage," in *Proceedings of the International Symposium on EMC*, Zuerich, 1982: 491-495

[29] S. Sali, "An improved model for the transfer impedance calculations of braided coaxial cables," in *IEEE Transactions on Electromagnetic Compatibility*, vol. 33, no. 2, pp. 139-143, May 1991

[30] T. Kley, "Optimized single-braided cable shields," in *IEEE Transactions on Electromagnetic Compatibility*, vol. 35, no. 1, pp. 1-9, Feb. 1993

[31] V. I. *FABRIKANT* (1987), "Electrical polarizability of small apertures: analytical approach," in *International Journal of Electronics Theoretical and Experimental*, 62:4, 533-545

[32] F. De Meulenaere and J. Van Bladel, "Polarizability of some small apertures," in *IEEE Transactions on Antennas and Propagation*, vol. 25, no. 2, pp. 198-205, March 1977

[33] R. De Smedt and J. Van Bladel, "Magnetic polarizability of some small apertures," in *IEEE Transactions on Antennas and Propagation*, vol. 28, no. 5, pp. 703-707, September 1980

[34] H. Schippers and J. Verpoorte, "Hole inductance in braided cable shields," in *IEEE International Symposium on Electromagnetic Compatibility (EMC)*, Dresden, 2015, pp. 56-61

[35] A. Kameari, "Calculation of transient 3D eddy current using edge-elements," in *IEEE Transactions on Magnetics*, vol. 26, no. 2, pp. 466-469, March 1990

[36] IEC 62153-4 series: "Metallic communication cable test methods, Electromagnetic compatibility (EMC)"

[37] I. M. Sobol', "On sensitivity estimation for nonlinear mathematical models," in *Matem. Mod.*, 1990, Volume 2, Number 1, 112–118

[38] Electromagnetic compatibility (EMC) Part 4-2: Testing and measurement techniques – Section 2: Electrostatic Discharge (ESD) immunity test, IEC-EN 61000-4-2, 2008

[39] Electromagnetic compatibility (EMC) Part 4-4: Testing and measurement techniques – Electrical fast transient/burst immunity Test, IEC-EN 61000-4-4, 2012

[40] M. Magdowski, R. Vick "Estimation of the Mathematical Parameters of Double-Exponential Pulses Using the Nelder-Mead Algorithm," in *IEEE Transactions on electromagnetic compatibility*, Vol.52, No.4, November 2010

[41] G. Brocrad, "Simulation in LTSpice IV: Handbuch, Methoden, und Anwendungen," Swiridoff, 2013, pp. 455-459

[42] M. Reisch, "Elektronische Bauelemente, Funktion, Grundschaltungen, Modellierung mit SPICE," Springer- Verlag Berlin Heidelberg 1998, pp. 370-377

[43] J. Cao, Y. Wang, Y. Wang, G. Lu, X. Zhang, "A novel SPICE circuit model of electrostatic discharge (ESD) generator," in *IEICE Electronics Express* vol. 13 no.9, pp. 1-8, May 2016

[44] Y. Zhou, J. Hajjar, "A circuit model of electrostatic discharge generators for ESD and EMC SPICE simulation," in *IEEE International Conference on EDSSC*, Chengdu, China, June 2014

[45] L. Buccolini, "Simple SPICE ESD Generator Circuit based on IEC61000-4-2 Standard," Available: http://www.youspice.com/simple-spice-esd-generator-circuit-based-on-iec61000-4-2-standard/

[46] F. Musolino, F. Fiori, "Modeling the IEC 61000-4-4 EFT Injection Clamp," in *IEEE Transactions on electromagnetic compatibility*, Vol. 50, No. 4.

[47] S. Caniggia, L. Vitucci, M. Acquaroli, A. Giordano, "Measurement and SPICE Models for Data Signal Lines Under Electrical Fast-Transient Test," in *4th European Symposium on Electromagnetic Compatibility - EMC EUROPE*, 11-15 Sep. 2000, Brugge (Belgium).

[48] S. Bauer, K. Hollaus, M. Leumueller, C. Tuerk, "Measurement and Modeling of Effective Cable Parameters of Unshielded Conductors," presented *at the 19th international IGTE Symposium, 2020,* Graz (Austria)